

AN IMPROVED DATA ACQUISITION SYSTEM FOR
CONTACTLESS CONDUCTIVITY IMAGING

A THESIS SUBMITTED TO
THE GRADUATE SCHOOL OF NATURAL AND APPLIED SCIENCES
OF
MIDDLE EAST TECHNICAL UNIVERSITY

BY

İLYAS EVRİM ÇOLAK

IN PARTIAL FULFILLMENT OF THE REQUIREMENTS
FOR
THE DEGREE OF MASTER OF SCIENCE
IN
ELECTRICAL AND ELECTRONICS ENGINEERING

APRIL 2005

Approval of the Graduate School of Natural and Applied Sciences

Prof. Dr. Canan ÖZGEN
Director

I certify that this thesis satisfies all the requirements as a thesis for the degree of
Master of Science

Prof. Dr. İsmet ERKMEN
Head of

Department

This is to certify that we have read this thesis and that in our opinion it is fully
adequate, in scope and quality, as a thesis for the degree of Master of Science

Prof. Dr. Nevzat G. GENÇER
Supervisor

Examining Committee Members

Prof. Dr. Cengiz Beşikçi (METU,EE) _____

Prof. Dr. Nevzat Güneri GENÇER (METU,EE) _____

Prof. Dr. Murat B. EYÜBOĞLU (METU,EE) _____

Assoc. Prof. Dr. Tolga ÇİLOĞLU (METU,EE) _____

Asst. Prof. Dr. Atila YILMAZ (HACETTEPE UNV.,EE) _____

I hereby declare that all information in this document has been obtained and presented in accordance with academic rules and ethical conduct. I also declare that, as required by these rules and conduct, I have fully cited and referenced all material and results that are not original to this work.

İlyas Evrim ÇOLAK

ABSTRACT

AN IMPROVED DATA ACQUISITION SYSTEM FOR CONTACTLESS CONDUCTIVITY IMAGING

Çolak, İlyas Evrim

M.S., Department of Electrical and Electronics Engineering

Supervisor: Prof. Dr. Nevzat G. Gençer

April 2005, 96 pages

The previous data acquisition system developed for the electrical impedance imaging via contactless measurements is improved to obtain measurements with a faster scanning speed of 0.15 sec/mm². This system uses magnetic excitation to induce currents inside the body and measures the magnetic fields of the induced currents with an axial gradiometer. Gradiometer consists of two differentially connected 10000-turn coils with diameter of 30 mm and a transmitter coil of 100-turn coil of diameter 30 mm placed and magnetically coupled between them. Transmitter coil is driven by a sinusoidal current of 200 mA (peak) whose frequency is 14.1 kHz. A Data Acquisition Card (DAcC) is designed and constructed on PCB, thus eliminates the use of the Lock-In Amplifier Instrument (LIAI) in the phase sensitive measurements. User interface programs to control the scanning experiments via PC (MATLAB Scanner 1.0, HP VEE Scanner 1.0) and to analyze the acquired data (Data Observer 1.0) are prepared. System performance tests for the DAcC are made. Error in the phase sensitive measurements is measured to be 0.6% of the test signals.

Minimum magnetic field density that can be detected is found to be $7 \mu\text{T}$. Output stage performance of the DAcC is improved by using an integrator instead of an amplifier in the output stage. In this manner, maximum linearity error is measured as $6.60 \times 10^{-4} \%$ of the full scale for the integrator circuit. Thermally generated voltage drift at the sensor output is measured to be 0.5 mV/minute in the ambient temperature. Overall normalized standard deviation at the output of the data acquisition system is observed as to be in the order of 10^{-4} . Mathematical relation between the resistive rings and conductive phantoms is studied. It is derived that maximum resistor value that can be distinguished in the resistive ring experiment which is 461Ω , corresponds to the phantom conductivity of 2.7 S/m . Field profiles (i.e., the voltage measurements) for the human left hand is obtained for the first time in literature, employing the LIAI. Agar objects with conductivity value of 1 S/m in a saline solution of 0.2 S/m are scanned and the field profiles are obtained using the DAcC. Image profiles of the scan fit well with the actual locations, geometries, and relative dimensions of the agar objects. A coil winding machine is prepared which enables the operator to design and wind up coils under self-controlled environment and conditions.

Keywords: Medical Imaging, Magnetic Induction, Magnetic Measurement, Electrical Impedance Imaging, Contactless Conductivity Imaging.

ÖZ

DOKUNMASIZ ELEKTRİKSEL İLETKENLİK GÖRÜNTÜLEME İÇİN İYİLEŞTİRİLMİŞ VERİ TOPLAMA SİSTEMİ

Çolak, İlyas Evrim

Yüksek Lisans, Elektrik ve Elektronik Mühendisliği Bölümü

Tez Yöneticisi: Prof. Dr. Nevzat G. Gençer

Nisan 2005, 96 sayfa

Biyolojik dokuların elektriksel iletkenliklerinin görüntülenmesi amacıyla hazırlanmış veri toplama sistemi 0.15 saniye/ mm^2 hızında tarama deneyleri gerçekleştirmek amacıyla geliştirilmiştir. Ölçüm sistemi, iletken cisim içerisinde manyetik indükleme yoluyla oluşturulan akımlardan kaynaklanan manyetik alanları eksensel bir farkölçer ile algılamaktadır. Farkölçer, 10000 sarımlı 30 mm çapında iki alıcı sargı ile yine 30 mm çapında ve alıcı sargıların arasına yerleştirilerek alıcı sargılara eşleştirilmiş 200 sarımlı bir verici sargıdan oluşmaktadır. Verici sargıda 200 mA tepe değerine sahip 14.1 kHz'lik bir akım akıtılmaktadır. Faza Duyarlı Yükseltici Cihazı'na (FDYC) olan ihtiyacı ortadan kaldırmak için Veri Toplama Kartı (VTK) tasarlanmış ve baskı devre şeklinde gerçekleştirilmiştir. Tarama deneylerini bilgisayar aracılığı ile düzenlemek amacıyla MATLAB Tarayıcı 1.0 ile HP VEE Tarayıcı 1.0 kullanıcı arayüz programları hazırlanmıştır. Toplanan verilerin incelenmesi için Veri Gözlemleyici 1.0 programı geliştirilmiştir. VTK kullanılan sistem için performans testleri gerçekleştirilmiştir. Faza duyarlı ölçümlerde hatanın test sinyalinin % 0.6'sını

aşmadığı görülmüştür. Ölçülebilir en düşük manyetik alan $7\mu\text{T}$ olarak bulunmuştur. VTK'nın çıkış devresinin performansı, bu kısımda yükseltici yerine integral alıcı devre kullanılarak iyileştirilmiştir. Bu şekilde, VTK'nın çıkış kısmında integral alıcı devre kullanıldığında doğrusallıktan sapmanın en büyük miktarı tüm ölçeğin % $6.60 \cdot 10^{-4}$ 'sı kadar olmaktadır. Durağanlığa ulaşmış sistemde, oda sıcaklığında, algılayıcı çıkışında sargıdaki sıcaklık değişiminden kaynaklanan voltaj oynaması 0.5 mV/dakika olarak bulunmuştur. Sistemin standart sapmasının 10^{-4} mertebesinde olduğu görülmüştür. Dirençli iletken halkalar ile iletken cisimler arasındaki ilişki matematiksel olarak incelenmiştir. Dirençli iletken halka deneylerinde ölçülebilen en büyük direnç değeri olan 461Ω 'un, 2.7 S/m 'lik bir iletken cisime denk olduğu türetilmiştir. FDYC ve sıfırlayıcı devre kullanılarak insan elinin alan görüntüsünün elde edilmesi, tarama sisteminin hızı iyileştirildikten sonra mümkün olmuştur. VTK kullanılarak, 1 S/m 'lik agar nesnelere agar cisimler, 0.2 S/m 'lik tuzlu su çözeltisinin içine yerleştirilerek taranmıştır ve alan görüntüleri (voltaj ölçümleri) elde edilmiştir. Tarama sonucunda elde edilen alan görüntüleri ile kullanılan agar cisimlerinin gerçek konumlarının, biçimlerinin ve birbirleriyle oransal büyüklüklerinin uyduğu görülmüştür. Kullanan kişinin sarım koşullarını ayarlayabileceği bir sarım makinası hazırlanmıştır.

Anahtar Kelimeler: Tıbbi Görüntüleme, Manyetik İndükleme, Manyetik Ölçüm, Elektriksel Empedans Görüntüleme, Dokunmasız İletkenlik Görüntüleme

**.Sevmek güzel, sevilmek herşey
.To love is fine, to be loved everything**

**.Annemle Babam
Siz olmasaydınız ben bu dünyada yoktum
If it were not for you, I wouldn't make my appearance**

ACKNOWLEDGEMENTS

First of all, I would like to express my deepest gratitude to my supervisor Prof. Dr. Nevzat G. GENÇER for his patience, guidance, advice, criticism, and insight throughout the research. As for the contributors section, surely including Mr. and Mrs. GENÇER, it had me think about where we had been before that peculiar point banded out to be everything, considering we appear sort of distant at the moment. Truth is, we were not distant in the past, not going to be in the future. The evidence is the meaning in the today of ourselves. Because the time is equal to the human. Since the start of my thesis, the Earth has made three and half rotations on the ellipsoidal orbit around the two foci which are the physical sun, (the source of life for our system-the power) and the transcendental sun which gives the meaning to the power which carries the power in the nature. During this study, the night folded over the day 1260 times, like the pages of my book being turned and turned one on other. The book in everything. I was to reserve different paragraphs for those who contributed to the formation of the thesis. The truth is, being far beyond a paragraph, they all contributed as being one in the book of the every thing. Everyone of us is included in the all, like the stars spread over the galaxy, rotating around the center with a balanced attraction. Due to the limited space, I will just mention the names whose contributions have been like the power which carry the power to me and praised as the birth from the darkness to the daylight: I would like to thank Zeynep (AKALIN) ACAR and Can ACAR, Yoldaş ATASEVEN, Emre ARPINAR28, Evren DEĞİRMENCİ, Koray Özdal ÖZKAN44. Comments of Hüseyin YİĞİTLER, Ayhan YILMAZ, Murat ÖZSÜT, Dario MARTIN LORCA are appreciated. I would also like to thank Feza CARLAK, Reyhan TUTUK, Serap AYDIN, A. Bülent UŞAKLI, Serkan ŞIK, my lab fellows and Zekeriya ÖZGÜN, Veysel EREN for the technical supports. I would like to welcome Deniz İLDENİZ, Mert and M. Yağız BAYRAK, who gathered us in the same family. Truth of everything can just be learned from the every thing by being with everything, recognizing yourself in the every thing.

TABLE OF CONTENTS

PLAGIARISM	iii
ABSTRACT	iv
ÖZ	vi
ACKNOWLEDGMENTS	ix
TABLE OF CONTENTS	x
LIST OF TABLES	xiii
LIST OF FIGURES	xiv
CHAPTER	
1. INTRODUCTION	1
1.1 Electrical Impedance Tomography	1
1.2 Conductivity Imaging via Contactless Measurements	5
1.3 Objectives of the Study	13
1.4 Outline of the Thesis	14
2. THEORY	15
2.1 Introduction	15
2.2 Formulation for the Induced Voltages in the Receiver Coils for an Arbitrary Shaped Object	15
2.3 Resistance of a Conductive Ring	18
3. EXPERIMENTAL SETUP	22
3.1 Introduction	22

3.2	The previous data collection system that uses a Lock-in Amplifier Instrument	22
3.2.1	Lock-in Amplifier Instrument	23
3.2.2	Nulling Circuit	25
3.3	Phase Sensitive Detection System using Data Acquisition Card.....	27
3.4	Coils	40
3.5	Power Amplifier.....	42
3.6	XY Scanner System	42
3.7	RS-232 Port Programming.....	46
3.8	Choice of the Excitation Frequency.....	49
4.	DATA ACQUISITION AND ANALYSIS SOFTWARE.....	51
4.1	MATLAB Scanner 1.0	51
4.2	HP VEE Scanner 1.0	52
4.3	Data Observer 1.0.....	54
5.	RESULTS	57
5.1	Introduction	57
5.2	The Lock In Amplifier Instrument and the Nulling Circuit.....	57
5.2.1	Phase and amplitude measurement test.....	58
5.3	The Data Acquisition Card (DAcC) Performance Tests.....	60
5.3.1	Scaling.....	60
5.3.2	Noise Levels of the DAcC Blocks	60
5.3.3	Phase and Amplitude Tests for the DAcC	62
5.3.4	Magnetic Field Measurement Tests Using Conductive Ring and Resistors	67

5.3.4.1	Conductive Ring and Resistor Experiment using the DC Amplifier.....	70
5.3.4.2	Conductive Ring and Resistor Experiment using Integrator	76
5.4	Scanning Experiments.....	78
5.4.1	Experiment using the LIAI.....	82
5.4.2	Experiment using the DAaC	83
6.	CONCLUSION AND DISCUSSION.....	86
	REFERENCES.....	89

LIST OF TABLES

TABLES

Table 1.1	The resistivity of body tissues at low frequencies (20-100Khz)[1]	2
Table 3.1	The LIAI settings	25

LIST OF FIGURES

FIGURES

Figure 1.1	ACEIT configuration	3
Figure 1.2	ICEIT configuration.....	3
Figure 1.3	A differential coil sensor to measure body conductivity by sensing magnetic fields of induced eddy currents	7
Figure 1.4	The measurement approaches applied by Ahmad and Gençer	9
Figure 2.1	Magnetic vector potential at point P created by current carrying loop...	17
Figure 2.2	The conductive ring	19
Figure 3.1	The structure of the data collection system using the LIAI.....	23
Figure 3.2	The nulling circuit diagram.....	26
Figure 3.3	The Data Acquisition Card (DAcC)	28
Figure 3.4	Locations of pin connectors in the DAcC.....	29
Figure 3.5	Transmitter Coil Current Buffer	31
Figure 3.6	Amplifier, A1 circuit connections	31
Figure 3.7	Phase shifter Q1 circuit connections.....	32
Figure 3.8	Phase shifter Q2 circuit connections.....	32
Figure 3.9	Phase shifter Q3 circuit connections.....	33
Figure 3.10	QA_SELECT Connector circuit connections.....	33
Figure 3.11	Receiver coil signal buffer circuit connections.....	34
Figure 3.12	Divider circuit for the receiver coil buffer output.....	34
Figure 3.13	Divider circuit for the transmitter buffer output	35
Figure 3.14	Rms to DC Converter circuit connections	35
Figure 3.15	Signal selection pin connector blocks.....	36
Figure 3.16	Multiplier circuit connections.....	36
Figure 3.17	Low Pass Filter circuit connections	37
Figure 3.18	Low Pass Filter circuit connections	37
Figure 3.19	Low Pass Filter circuit connections	38
Figure 3.20	Low Pass Filter circuit connections	38
Figure 3.21	Input selection pin connector, A2_IN_S2	39
Figure 3.22	Amplifier circuit connections	40
Figure 3.23	Integrator circuit connections	41
Figure 3.24	PIC16F877 Microcontroller circuit	41
Figure 3.25	The power amplifier circuit diagram	43
Figure 3.26	Step motors driving circuitry	45
Figure 3.27	The switching sequence of the step motor terminals.....	46
Figure 3.28	(a): Appearance of the XY Scanner, (b): The data acquisition system...	47
Figure 3.29	RS-232 DB09S Connector.....	48
Figure 3.30	RS-232 Connection Scheme used in this study	48
Figure 3.31	Standard 9-Pin RS-232 sockets [75].....	49

Figure 3.32	The response of the differentially connected receiver coils	50
Figure 4.1	MATLAB based user interface program Scanner 1.0	52
Figure 4.2	HP VEE 4.0 based user interface program HP VEE Scanner 1.0	53
Figure 4.3	MATLAB based user interface program DataObserver 1.0	55
Figure 4.4	MATLAB based user interface program DataObserver 1.0	56
Figure 5.1	Test setup for phase sensitive measurement system using the LIAI and the nulling circuit.....	58
Figure 5.2	Output voltage of the LIAI (A') as a function of the input phase angle (ϕ) for different values of input amplitude A	59
Figure 5.3	Peak value of the output amplitude (A'_{PEAK}) as a function of input amplitude (A_{PEAK}).....	59
Figure 5.4	Divider circuit (D1) output voltage as a function of transmitter coil current	61
Figure 5.5	Standard deviation at the output of amplifier block, (indicated as DC Figure 3.3) as a function of the test signal amplitude	63
Figure 5.6	Mean value of the amplitude of the output of the amplifier as a function of the test signal amplitude	63
Figure 5.7	The DAcC Test Setup	64
Figure 5.8	Output voltage for DAcC as a function of phase difference.....	65
Figure 5.9	Test setup which is used to investigate the response of the measurement system to external magnetic field	65
Figure 5.10	Digitally controlled variable gain circuit.....	66
Figure 5.11	Digitally controlled variable gain circuit.....	66
Figure 5.12	Measured in-phase component voltage for different values of L	68
Figure 5.13	Measured signal due to I_{EXT} as a function of decimal value of the Port D.....	68
Figure 5.14	Magnetic field generation by the conductive ring with variable resistance R	69
Figure 5.15	The output voltage of the amplifier as a function of the samples taken during whole experiment.....	72
Figure 5.16	Output of the amplifier as a function of the Difference Data for all measurements	72
Figure 5.17	Output voltage of the DAcC employing the amplifier as the last stage .	73
Figure 5.18	Zoomed version of the output voltage in figure 5.17	73
Figure 5.19	Difference Data obtained from the output voltage of the DAcC with amplifier.....	74
Figure 5.20	Output voltage of the Amplifier as a function of (Zoomed) $1/\text{Resistor Values}$	75
Figure 5.21	Output of the integrator in the DAcC as a function of sample number..	77
Figure 5.22	Output of DACC using the integrator at the output stage as a function of the difference data sample number.....	77
Figure 5.23	Slope of the lines fitting to the difference data for resistor values	79
Figure 5.24	Zoomed version of the slope of the lines fitting to the difference data in Figure 5.23 as a function of resistor values.....	79
Figure 5.25	Slope of the difference data lines as a function of inversed resistor values	80
Figure 5.26	Slopes of the difference data lines as a function of $1/\text{Resistor values}$	81

Figure 5.27 The field profile of the palm of the human left hand.....	83
Figure 5.28 (a): Image profile of the agar objects placed in saline solution of 0.2 S/m , (b): Agar objects of 1 S/m.....	85

CHAPTER 1

INTRODUCTION

1.1 Electrical Impedance Tomography

Imaging modalities are based on distinguishing a specific physical property of the tissue, such as X-Ray attenuation coefficient for the Computed Tomography (CT), or proton density in the Magnetic Resonance Imaging (MR). Electrical Impedance Tomography (EIT) is based on the measurement of resistance and reactance patterns [1], [2]. EIT is used to measure tissue conductivities that cover a wide range of values as shown in Table 1.1, by introducing low frequency alternating currents to the body and measuring the resulting electrical potential fields via surface electrodes [1].

Depending on the way of introducing currents in the body, there are two main EIT approaches: 1) Applied Current Electrical Impedance Tomography (ACEIT) and, 2) Induced Current Electrical Impedance Tomography (ICEIT). In ACEIT (Figure 1.1), both current injection and voltage measurements are performed via surface electrodes [1], [3]-[5]. In ICEIT (Figure 1.2) currents are induced by magnetic induction and voltage measurements are performed by the attached electrodes [6]-[11].

EIT can be used in monitoring brain during the cardiac cycle ([12], [13]), to detect cardiac volume changes, diagnosis of emphysema [14], heart imaging [15]-[17], respiratory volumetric measurements ([18], [19]), chest impedance imaging [20], monitoring gastric emptying ([21], [22]), breast cancer detection

Table 1.1: The resistivity of body tissues at low frequencies (20 to 100 kHz) [1].

Tissue	Resistivity (Ωcm)
Cerebrospinal Fluid	65
Plasma	66
Blood	150
Liver	350~550
Human Arm	240 (longitudinal) 675 (transverse)
Skeletal Muscle	125 (longitudinal) 1800 (transverse) 150 (longitudinal) 2300 (transverse) 530 (average of above)
Cardiac Muscle	160 (longitudinal) 424 (transverse) 575 (longitudinal) 5181 (transverse) 410~750 (average of above)
Neural Tissue	580 284 (gray matter) 682 (white matter)
Lung	727~2363
Fat	2060~2720
Bone	16600

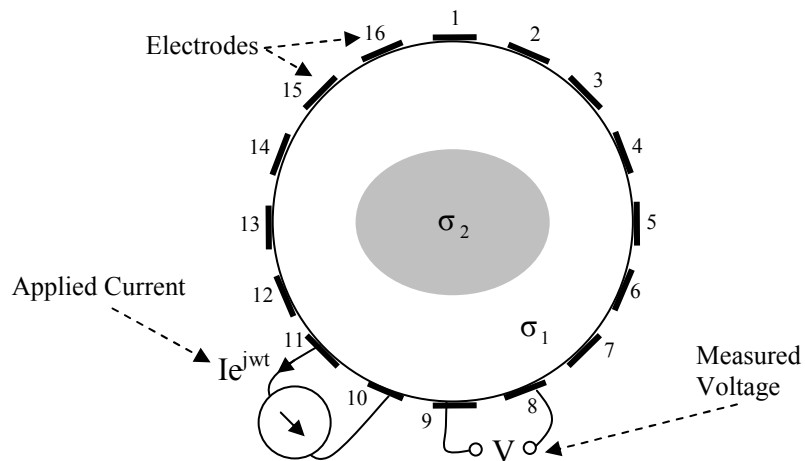


Figure 1.1: ACEIT configuration. For this specific case in the figure, 16 electrodes are attached on the body surface. σ_1 and σ_2 represent conductivities of different regions. Current is applied between the two surface electrodes and voltages between the remaining 13 pairs are measured in a cyclic manner.

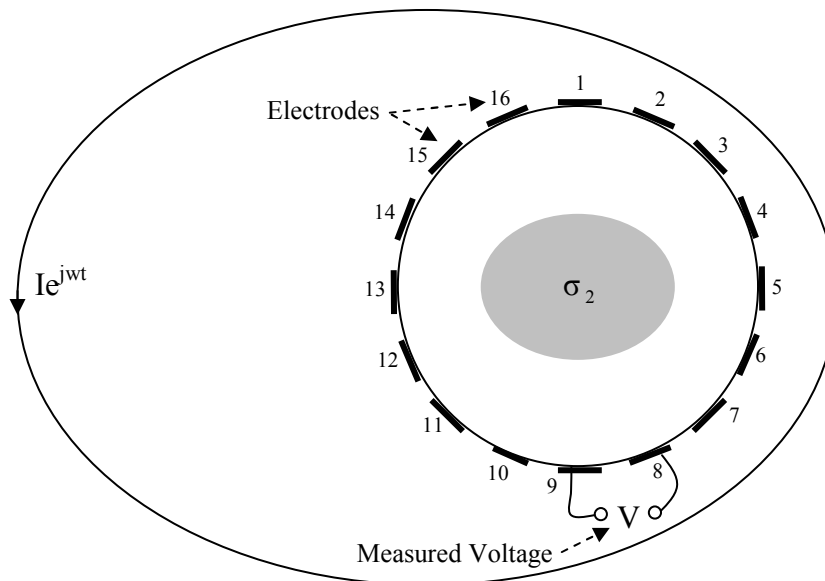


Figure 1.2: ICEIT configuration. For this specific case in the figure, 16 electrodes are attached on the body surface. σ_1 and σ_2 represent conductivities of different regions. Current flowing through the outer ring induces currents in the conductive object. Voltage measurements are done via the surface electrodes.

([23]-[26]), conductivity changes due to ventilation and perfusion [27], brain edema detection [28], brain function monitoring ([29], [30]), human lung and thorax function monitoring [31], lung cancer and tumour localization [32]. Further applications and aspects of EIT can be found in [32]-[35].

Although currently not being capable of very high resolution, EIT has some advantages compared with CT or MR:

- The time required to collect and process a data set is small compared to that required by CT or MRI systems. This makes EIT systems particularly useful for examining dynamic events in both clinical and other applications,
- EIT systems use low power, low frequency sources and consequently can be used for long term clinical monitoring without risk of damage to the subject,
- The sensitivity of EIT systems to small changes in conductivity is sufficient to discriminate between blood and various soft tissues,
- The cost of a complete EIT system is between one and two orders of magnitude less than that of either CT or NMR systems.

Trade-off between ACEIT and ICEIT are discussed in [6] and [8]. In ACEIT, an electrode is used for both current injection and voltage measurement, which imposes circuit design constraints. Moreover, bones act as barriers for the injected current, thus reducing the injected current density in deep lying tissues [36]. However, injected current must be limited for safety considerations of the skin where the electrodes are connected, which causes the measured voltages to be diminished. As a result, the Signal-to-Noise Ratio (SNR) decreases. Alternative solutions to these problems involve complication of the circuitry and the cabling.

To overcome the problems related to ACEIT to some degree, ICEIT is proposed in 1990 as a new method for imaging the human conductivities [37], [38]. Although images of two and three dimensional objects were also given in the same studies, detailed mathematical analysis of the problem is given in [7] and [9]. ICEIT

has some advantages on ACEIT: Since the electrodes are used only for voltage measurements, coil configuration and related circuitry can be optimized. A major advantage revealed by studies of Purvis et al. ([6]) and Gençer et al. ([7], [9]) was that the independent measurements could be increased by spatially independent magnetic field patterns. This can be achieved by only employing additional electrodes in ACEIT. Another point which needs to be emphasized is that the need for minimizing the contact resistances of electrodes (which is important in ACEIT) was eliminated in ICEIT by magnetic induction. Thus, current injection limit at the surface electrodes due to safety considerations in ACEIT was overcome in ICEIT.

As a summary, major disadvantages of the techniques that employ electrodes are the low spatial resolution and the limitations related to electrodes [6]-[9]. The resolution of the EIT system falls significantly with increasing distance from measuring electrodes and traditional EIT measurement schemes are unsuitable for example, for mammography because of this reason [24]. A large number of electrodes, which are required to provide acceptable resolution of the system, causes an increase in the computation time for image reconstruction ([24], [39]). Besides, low spatial resolution does not permit the use of EIT, for example for exact tumor localization inside a lung [32]. Moreover electrode placement and recording their precise location are important problems in practice [40], [41]. Due to these limitations, there has been an increasing interest in developing possible methods of contactless imaging of the internal electrical conductivity of the human body.

1.2 Conductivity Imaging via Contactless Measurements

In this method, magnetic excitation is used to induce eddy currents inside the body and the resulting magnetic fields are measured with pick up (receiver) coils. Primary flux generated by the transmitter coil induces eddy currents in the conductive object. Primary flux linked through the identical receiver coils is equal since both coils are at same distance from the transmitter coil which is the source of the primary field. However, secondary flux generated by the eddy currents flowing in the conductive object is linked through the differentially connected receiver coils

unequally or in an unbalanced fashion due to the fact that flux strength is diminished with distance. This causes a gradient voltage in the receiver coils due to conductive object (Figure 1.3).

Compared to the described EIT techniques this method has following advantages:

- In injected current systems the largest current densities occur at the electrodes. Since the induced current system is not limited by high surface injection current densities, the internal induced currents could be increased if necessary with a corresponding increase in signal to noise ratio. The currents are introduced via magnetic excitation thus it is possible to eliminate the screening effect of the bones [10],
- There is no physical contact between the body and the measurement system,
- The performance of the imaging system and scanning movements are not limited by the need for good surface electrode contacts [36].

Therefore conductivity measurement by magnetic induction and magnetic measurement is a valuable alternative for impedance measurements of biological tissues. This method has been known for decades. Common applications include industrial imaging for the visualization and control of processes in vessels and pipelines [42], nondestructive testing, environmental monitoring for tracking the migration of pollutants underground [43], salt content measurements in sea water, impurity measurements in semiconductors, imaging submerged remains in archaeology [44].

Tarjan and McFee were first to propose this method for medical purposes in 1968 to determine the effective electrical resistivity (100 kHz) of the human torso and head [45]. The same group also proposed this method to follow conductivity fluctuations as a result of cardiac activity and ventilation [45]. Almost 25 years later, Al-Zeibak and Saunders proposed a contactless measurement system which operates at 2 MHz. A sensor probe was used to scan the saline solutions and by employing the

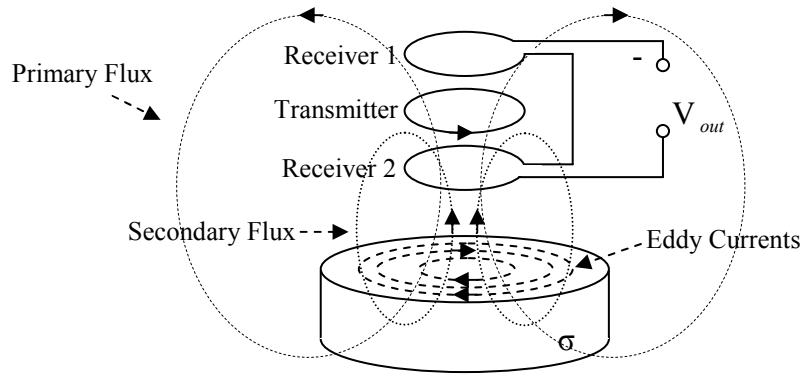


Figure 1.3: A differential coil sensor to measure body conductivity by sensing magnetic fields of induced eddy currents.

computational algorithms developed for X-ray computed tomography conductivity images were reconstructed. It was shown that fat and fat-free tissues could be distinguished and the internal and external geometry of simple objects can be determined. The system was named as *Mutual Inductance Tomography* [46]. Around the same times, Netz et al. employed 25-mm diameter coils and showed a linear dependence between the subsurface measurements and the electrolytic content of saline solutions at an operating frequency of 100 kHz [36]. The ability to detect simulated cytotoxic edema conditions in a skull model was also shown.

Gençer and Tek explored the feasibility of this method for safety conditions at 50 kHz [47]. The pick-up voltages for a miniaturized coil configuration (10-mm radius) over a uniformly conductive semi-infinite region were calculated around 10 μV while the induced currents were well below the safety limit (1.6 mA/cm^2 at 50 kHz) [47]. Thereafter, they proposed the use of this method for subsurface imaging and showed its potential numerically by three-dimensional simulations [47]-[50].

The experimental study utilizing the previous theoretical and numerical work was presented by Ülker and Gençer [51]. The system operates at such a low frequency like 11.6 kHz for the first time in the literature. Ülker and Gençer employed receiver coils which have 10000 turns both and are differentially connected to cancel out the primary voltage created by the 100 turn transmitter coil located between the receiver coils. Thus these three coils are magnetically coupled to form a three-layer-sensor. Sensor layers are 15 mm in diameter. The data were

acquired using a PC-controlled lock-in amplifier instrument. A scanner hardware to which the sensor was attached was constructed mostly with nonconductive material (delrin) to scan the probe over two dimensional surfaces. The linearity of the system is 7.2% at full scale and the sensitivity from 0.3 cm is 21.47 mV/(S/m). The system has a signal-to-noise ratio of 34 dB and a thermal stability of 33.4 mV/C°. It was observed that it is possible to detect a conducting tube of average conductivity (0.2 S/m) when the body is 6 cm from the sensor. Conductivity images were reconstructed using the steepest-descent algorithm. Images obtained from isolated conducting tubes show that it is possible to distinguish two tubes separated 17 mm from each other. The images of different phantoms were found to be a good representation of the actual conductivity distribution. Even the field profiles obtained by the scanning system were observed to be the good representatives of the conductive object under investigation, which showed the potential of this methodology for clinical applications ([51]-[53]).

Another study using magnetic induction-magnetic measurements for contactless conductivity measurement was pursued by Ahmad and Gençer [54]. In that study, two approaches were proposed. The first one employs a single coil through which the exciting current flows to generate the primary field. Eddy currents induced by the primary field flows in the conductive object and oppose the primary field which causes a change in the inductance of the coil. This, in turn, affects the resonance frequency of the coil. An impedance-to-frequency converter was used to measure the change in the inductance of the coil (Figure 1.4 (a)). A 100 Hz change per 0.19 S/m was generated with this method. The system was tested at a high frequency of 1.4 MHz. In the other approach, two transmitter coil- receiver coil pairs were employed, one of which was the sensor and other one was the auxiliary coil (Figure 1.4 (b)). Transmitter 1 in the first pair (sensor) was used to induce eddy currents in the conductive object. Receiver 1 was used to pick up the flux generated by the eddy currents, while other pair (the auxiliary coil) was kept distant from the first sensor (and not effected from the conductive object). The auxiliary coil was used to generate an auxiliary signal to cancel out the primary voltage induced in the Receiver 1. Primary signal which was induced by direct coupling of the Transmitter 1 to Receiver 1, was very large (about 150 V) compared to the voltage induced by

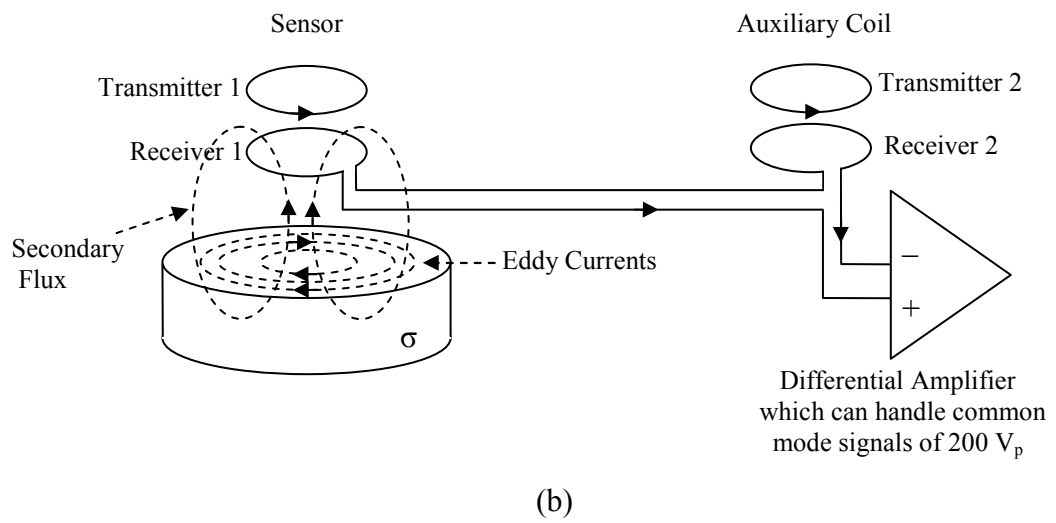
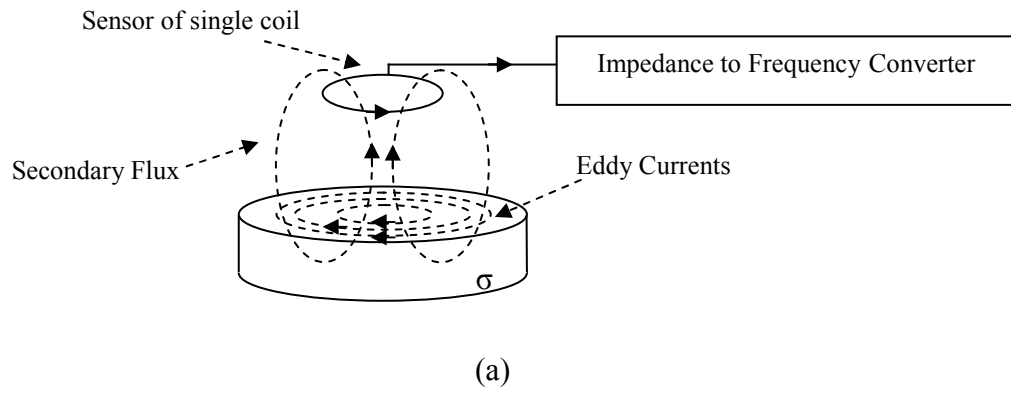


Figure 1.4: The measurement approaches applied by Ahmad and Gençer [54], [55]
 a) Single coil system, b) Two-coil system.

the eddy currents flowing in the conductive object, and needed to be cancelled out by the use of the auxiliary coil. The induced voltage due to conductive object was 18 μV per 0.19 S/m at 15 kHz. The SNR of the system was measured as 39 dB while Full Width at Half Maximum (FWHM) was measured as 9 mm with a 1 mm object of 2 S/m conductivity. In that study, field profiles of 1 mm to 30 mm diameter objects whose conductivities varied from 0.2 S/m to 2 S/m were obtained. In another experimental study even a broken bone hidden in mutton chop could be observed clearly in [55]. Further information can be found in [54] and [55].

Recently new studies on contactless conductivity measurement and MIT are being pursued. The approach of Ülker and Gençer was employed by Riedel et al. with an 2*2 array of axial gradiometers in which each sensor consists of five Printed Circuit Board (PCB) elements [56]. The excitation and measurement coils have spiral coils of 2.5 cm diameter and all have 13 turns. The measurement coils have a distance of 5 mm to the excitation coil. The shielding has a distance of 1 mm to the measurement coil. All PCBs were fixed with plastic screws to adjust the sensor output. The distance of the PCB boards can be changed by turning the screws and checking the output voltage at the oscilloscope. To avoid capacitive coupling, shielding which consists of radial and star shaped PCB lines were used. Sensor output voltage varies linearly with the coefficient 0.033 mV S⁻¹ m using an excitation current of 316 mA at 600 kHz in the range of 0-5 Sm⁻¹. No apparent correlation with conductivity for the real component was reported. The noise and drift of the imaginary component of the sensor output were given as 0.001 mV and 0.006 mV, respectively.

Korzhenevskii and Cherepenin presented a theoretical study of the two-coil arrangement and proposed the direct measurement of phase angle for detecting the conduction eddy currents [57]. Korjenevsky et al. reported the implementation of this method [58]. The system employed 16 electronically switched excitation and detection coil units arranged in a circle. The carrier frequency of the system was 20 MHz and this was down-converted to 20 kHz for processing. Demonstration of the imaging of cylindrical objects, with positive and negative conductivity contrast, in a saline bath is given in the same study. The objects, each with diameter 29% of the array diameter, were clearly resolved using a filtered-back projection algorithm.

Korjenevsky and Sapetsky showed that reduced spatial distortion could be achieved when images were reconstructed by a neural network for some simple distributions of conductivity [59].

A review of Magnetic Impedance Tomography (MIT) studies can be found in [60]. Recent publications on this topic will be summarized below:

Watson et al. preferred to realize a down-conversion-type phase detector circuit for direct phase measurement between the excitation signal and the received signal instead of amplitude detection [61]. The idea originates from the observation that a change in the induced conduction current of 1%, for instance, would result in a received signal amplitude variation of just 0.005%. A 100-sample average taken with this circuit provides a precision of less than or equal to 22 millidegree for input amplitudes down to 2.8 mV_{pp}. The measured drift for this configuration, however, was found to be 0.03°. Sources of phase noise were investigated. It was concluded that phase measurement of the required precision for high-frequency biomedical MIT was possible with a down-converting direct phase MIT system, if the systems coils and preamplifiers could provide receiver signals on the order of a few mV without adding a significant phase noise.

Gough reported a circuit for measurement of small phase delays in MIT, employing phase sensitive detection and avoiding the complication of using frequency down-conversion [62]. The ‘raw’ noise in the measurement of phase was 1.5 millidegree which seems to compare favorably with [57] which gives 22 millidegree of phase resolution.

Watson et al. describes the results of measurements carried out with a 16-channel, downconverting, 10 MHz, MIT system utilizing two types of data extraction techniques: direct-phase measurement and measurement of the in-phase and in-quadrature components of the signal with a vector voltmeter [63]. The basic precision provided by each technique was 50 millidegree, and the thermal drift was shown to be the major limiting factor. Performances of both techniques were compared considering phase noise, phase skew and phase drift and data acquisition time. It was concluded that both techniques exhibit certain advantages and disadvantages resulting from the nature of the techniques themselves.

Watson et al. also suggested a sensor alignment for the primary field cancellation in MIT which is called B_x -sensor method [64]. They employed ferrite chip inductors of inductance $10 \mu\text{H}$ as the receiver coil. With a compensated ferrite-cored sensor, the noise and drift in the signal were reduced by factors of 43 and 51, respectively, relative to the uncompensated orientation. Compensation was achieved by aligning the receiver perpendicular to the transmitter coil. Thus receiver sensitivity to primary field was minimized.

The same principle was employed by Igney et al. to construct a planar array MIT system [65]. The system comprises 4 printed excitation coils of 4 turns which are shielded and 8 surface-mount inductors of inductance $10 \mu\text{H}$ as sensor. The excitation current was multiplexed via relays to drive the excitation and reference coils. The system was found to provide a SNR of 30–50 dB over the frequency range 1–8 MHz, based on the peak value for all channels, using a 0.3 S/m phantom of dimensions $20 \text{ cm} \times 20 \text{ cm} \times 10 \text{ cm}$. The results of the linearity measurements for selected channel combinations imply approximately $50 \mu\text{V}/\text{Sm}^{-1}$ sensitivity in the range from 0 to 2 Sm^{-1} .

Watson et al. examined the relative performance of the axial and B_x gradiometers through computer simulations of the sensitivity profiles produced by a single sensor and comparison of the reconstructed images produced by sensor arrays. [66]. A finite-difference model was used to determine the sensitivity profiles obtained with each type of sensor arrangement. B_x sensors were found to provide higher sensitivity at depth than axial gradiometers.

Scharfetter et al. used planar gradiometers to calculate and measure the sensitivity maps for a single channel MIT system [67]. For that purpose, a cylindrical tank (diameter 200 mm) with a spherical perturbation (diameter 50 mm) of conductivities in the physiological range was used. The excitation coil was a solenoid (diameter 100 mm) with its axis perpendicular to the cylinder axis. Calculations were carried out with a finite element model comparing the planar gradiometer and a solenoid receiver coil with its axis perpendicular to the excitation coil axis. The planar gradiometer was much less sensitive to far sources of electromagnetic interference. Preliminary measurements showed that the SNR of the measured signal

was more than 20 dB better for the planar gradiometer than for the solenoid receiver when the coils were not shielded magnetically.

Scharfetter et al. developed a new type of gradiometer (zero flow gradiometer) which combines the advantages of planar coil system and B_x or zero flow coil system [68]. The perturbation to signal ratio of the combined system was more than 12 times lower than that of the zero flow coil system. Eight planar gradiometers were oriented to receive zero flux from the excitation coil. Thus perturbations from far sources were cancelled as effectively as with the planar gradiometers. The induced spurious signals due to thermal mismatch between both halves of the gradiometer were minimized.

As a last point to finalize this section, the crucial difference between Gençer, Ülker and Ahmad's systems and Magnetic Impedance Tomography (MIT) systems must be emphasized: Although all employ magnetic induction-magnetic measurement method to measure conductivities, the systems of Gençer, Ülker, and Ahmad operate at low frequencies (11.6 kHz and 15. kHz) whereas MIT employs high operating frequencies (1MHz to 10 MHz). Low operating frequency have some certain advantages on high frequency: At high frequencies 1) the displacement currents in the conducting body are not negligible; 2) the propagation effects should be taken into account; and 3) the stray capacitances are effective in the measurements [51]. Thus, in MIT, both the theory and the experimental work are more complicated than the low frequency studies.

1.3 Objectives of the Study

Objectives of this study are listed as follows:

- To develop a data acquisition system without using a lock-in amplifier instrument. In order to do this necessary hardware will be designed and will be implemented.

- To improve the speed of the scanning system,

- To prepare a data analysis software to test the quality of the acquired data.

1.4 Outline of the Thesis

In this thesis after an introduction on existing conductivity measurement techniques (Chapter 1), the theory behind magnetic induction and magnetic measurement method is explained (Chapter 2). The details of the new data acquisition system are presented in Chapter 3. In Chapter 4, the data acquisition and analysis software are explained. The results are presented in Chapter 5. The performance of the system and possible future work are discussed in Chapter 6.

CHAPTER 2

THEORY

2.1 Introduction

Conventional eddy current inspection is carried out as follows: A coil built into the sensor is fed with a high-frequency alternating current and the sensor is positioned close to a conductive object. The electromagnetic field of the coil creates eddy currents in the target. A magnetic flux is created in reaction to the flow of eddy currents which results in the change of the impedance of the coil. With a proper circuitry, either Hall Effect Sensors or receiver coils are used to measure the magnetic fields created by the eddy currents or the change in the coil impedance to reveal information about the conductivity of the target [69].

The instrument used in this study is a three coil differential transformer. In the following sections, first, formulations related to induced voltages in a differential coil system due to an arbitrary shaped conductive object will be presented. After that, resistance calculation for a ring shaped conductive object is given. Overall resistance of the ring is directly related to the eddy current density flowing in the ring. Calculation of this value is useful in preparing sample conductive objects with known resistances to test the system performance.

2.2 Formulation for the Induced Voltages in the Receiver Coils for an Arbitrary Shaped Object

Theoretical formulation relating conductivity to magnetic measurements is given in [49]. A summary of this theoretical background will be presented here. In

a linear, isotropic, non-magnetic medium, the electric field \vec{E} has two sources namely, the time varying magnetic field and the surface and volume charges. For the sinusoidal excitation, \vec{E} can be expressed as the combination of these two sources :

$$\vec{E} = -j\omega\vec{A} - \nabla\phi \quad (2.1)$$

where \vec{A} , ϕ , and ω represent the magnetic vector potential, scalar potential and radial frequency respectively.

For a circular loop of radius a , centered at origin in the x-y plane, carrying a current I as shown in Figure 2.1, magnetic vector potential, \vec{A}_p , at point P is calculated from [70] (page 182):

$$A_\phi(r, \theta) = \frac{\mu_0}{4\pi} \frac{4I_a}{\sqrt{a^2 + r^2 + 2ar \sin \theta}} \frac{(2 - k^2)K(k) - 2E(k)}{k^2} \quad (2.2)$$

where K and E are the elliptic integrals of first and second kinds, respectively. Argument k of the elliptic integral can be calculated using:

$$k^2 = \frac{4ar \sin \theta}{a^2 + r^2 + 2ar \sin \theta} \quad (2.3)$$

The scalar potential ϕ , for the same coil is calculated by solving the following differential equations [9],[11]:

$$\nabla \cdot (\sigma \nabla \phi) = -\omega \vec{A}_p \cdot \nabla \sigma \quad (2.4)$$

$$\frac{\partial \phi}{\partial n} = \omega A_{pn} \quad (2.5)$$

where \vec{A}_{pn} is the normal component of the magnetic vector potential on the surface of the conductive object whose conductivity is represented as σ .

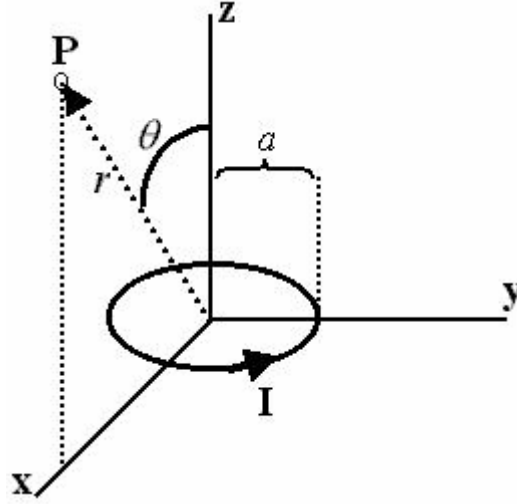


Figure 2.1: Magnetic vector potential at point P created by current carrying loop.

In the above equation, the scalar potential has only imaginary component. Consequently \vec{E} can be expressed as:

$$\vec{E} = -j(\omega \vec{A} - \nabla \phi) \quad (2.6)$$

The induced current density \vec{J}_i in the conductive object is $\vec{J}_i = \sigma \vec{E}$. This current in the conductive object create a magnetic flux Φ which is picked up by the receiver coil. Using the reciprocity theorem [71], Φ can be calculated using the following integrals in the corresponding volumes [49]:

$$\Phi = \frac{1}{I_R} \oint \vec{A}_R \cdot \vec{J}_T dV_{COIL} + \frac{1}{I_R} \int \vec{A}_R \cdot \vec{J}_I dV_{BODY} \quad (2.7)$$

where \vec{A}_R is the magnetic vector potential created by the reciprocal current I_R in the receiver coil. \vec{J}_T and \vec{J}_I represent the current density in the transmitter coil and the induced current density in the conductive object, respectively. The first term on the right is the primary flux, directly coupled from the transmitter coil. The second term

represents the flux caused by the induced currents. The electromotive force in the receiver coil can then be expressed as:

$$v = -j\omega\phi$$

$$v = -j(I_T \oint (\frac{w\vec{A}_R}{I_R}) \cdot d\vec{l}) - \int (\frac{w\vec{A}_R}{I_R}) \cdot \sigma(w\vec{A}_T + \nabla\phi)dV' \quad (2.8)$$

As seen in the above equations, the induced voltage in the receiver coil has two components. The quadrature component (with j coefficient) arises from the transmitter coil current while the in-phase component includes the conductivity information. Quadrature component is very large compared with the in-phase component and is cancelled out by use of differentially connected receiver coils. For perfectly matched receiver coils which have the same electrical characteristics, placed at the same distance from the transmitter coil, the differential connection produces the output voltage of:

$$v = \int w \left(\frac{w\vec{A}_{R_1}}{I_{R_1}} - \frac{w\vec{A}_{R_2}}{I_{R_2}} \right) \cdot \sigma(w\vec{A}_T + \nabla\phi)dV' \quad (2.9)$$

Here \vec{A}_{R_1} and \vec{A}_{R_2} are the magnetic vector potentials created by the reciprocal currents I_{R_1} and I_{R_2} , respectively. \vec{A}_{R_1} and \vec{A}_{R_2} can be calculated using the same formula given in equation (2.2) and (2.3).

2.3 Resistance of a Conductive Ring

Let us assume that a magnetic flux density $B(t) = B_o \cos(\omega t)\vec{a}_z$ is applied to a conductive ring of conductivity σ , with inner radius of b and outer radius of a , placed on the x - y plane as shown in Figure 2.2.

Voltage induced around contour C can be found starting from Maxwell Equations [72]:

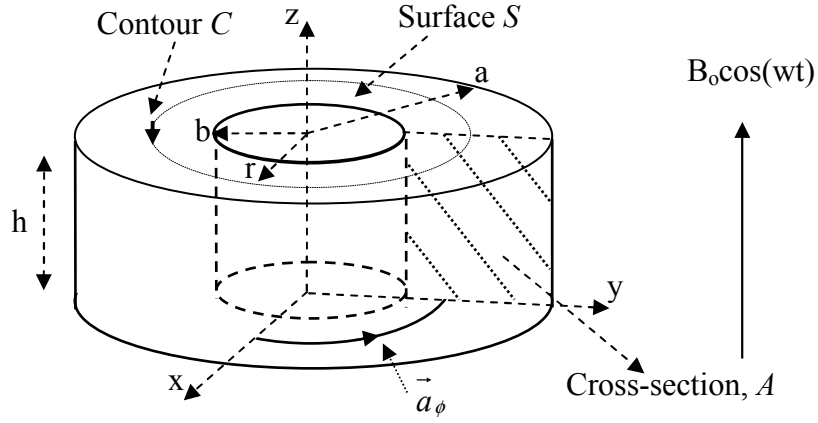


Figure 2.2: The conductive ring. A z-directed magnetic field applied to a conductive ring of inner radius b and outer radius a . Height of the ring is indicated as h .

$$\nabla \times E = -\frac{dB}{dt} \quad (2.10)$$

Applying Stokes's theorem to (2.10) and using (2.12) we can write:

$$\begin{aligned} \oint_C \vec{E} \cdot d\vec{l} &= \int_S -\frac{dB}{dt} = V_{induced} \\ &= -\frac{d\Phi}{dt} = V_{induced} \end{aligned} \quad (2.11)$$

Taking the surface integral of B over surface S which is encircled by contour C (Figure 2.2),

$$\begin{aligned} \Phi &= B \cdot S \\ &= B_0 \cos(wt) \pi(r^2 - b^2) \end{aligned} \quad (2.12)$$

The time derivative of Φ is obtained as follows,

$$\begin{aligned}
-\frac{d\Phi}{dt} &= -\frac{d(B_0 \cos(\omega t) \pi (r^2 - b^2))}{dt} \\
&= -\frac{d(B_0 \cos(\omega t) \pi r^2)}{dt}
\end{aligned} \tag{2.13}$$

Since the magnitude of the electric field is constant on a specific contour C , using cylindrical coordinates, combining Eq. 2.11 and Eq.2.13 we obtain:

$$E_\phi \cdot 2\pi r = \pi r^2 \omega B_0 \sin(\omega t) \tag{2.14}$$

$$E_\phi = \frac{1}{2} B_0 r \omega \sin(\omega t) \tag{2.15}$$

Since \vec{E} has only the \vec{a}_ϕ component,

$$\vec{E} = \frac{1}{2} B_0 r \omega \sin(\omega t) \vec{a}_\phi \tag{2.16}$$

Thus, the current density \vec{J} can be found by multiplying electric field with conductivity σ :

$$\vec{J} = \sigma \vec{E} = \sigma \frac{1}{2} B_0 r \omega \sin(\omega t) \vec{a}_\phi \tag{2.17}$$

Current flowing in the conductive ring is then found by integrating the current density:

$$\begin{aligned}
I &= \int_A \vec{J} \cdot \vec{dS} = \int_0^h \int_b^a \frac{\sigma B_0 \omega r}{2} \sin(\omega t) dr dz \\
&= \frac{\sigma B_0 h \omega (a^2 - b^2)}{4} \sin(\omega t) \text{ (Amps)}
\end{aligned} \tag{2.18}$$

The dissipated power (Eddy current loss) can be obtained as follows:

$$\begin{aligned}
 P &= \int_V \vec{J} \cdot \vec{E} \, dV = \int_V \sigma |E|^2 \, dV \\
 &= \int_0^h \int_0^{2\pi} \int_b^a \frac{\sigma B_0^2 \omega^2 r^2}{4} \sin^2(\omega t) r \, dr \, d\phi \, dz \\
 &= \frac{\sigma B_0^2 \pi h (a^4 - b^4)}{8} \omega^2 \sin^2(\omega t) \quad (\text{Watts})
 \end{aligned} \tag{2.19}$$

Since $P = \frac{1}{2} I^2 R$, using (2.16) and (2.17), the effective resistance R of the conductive ring can be obtained as:

$$R = \frac{P}{I^2} = \frac{4\pi}{\sigma h} \frac{a^2 + b^2}{a^2 - b^2} \quad (\Omega) \tag{2.20}$$

CHAPTER 3

EXPERIMENTAL SETUP

3.1 Introduction

In this chapter, first the hardware modifications made on the existing data collection system (that employs a Lock-in Amplifier Instrument (LIAI)) are presented ([51]-[53]). To eliminate the use of the LIAI, a data acquisition card (DAcC) is designed and printed on PCB. Details of these studies are explained in the next subsections.

3.2 The previous data collection system that uses a Lock-in Amplifier Instrument

The block diagram of the data collection system is shown in Figure 3.1. The coils are coaxial and 15 mm in radius. Oscillator output of the LIAI feeds the power amplifier which excites the transmitter coil. The induced primary voltage in the differentially connected receiver coils is cancelled out by the nulling circuit. Thus, the residual signal becomes nearly 0 V when there is no conducting object. The output of the nulling circuitry is connected to the input of the LIAI for phase sensitive detection. The LIAI's reference signal channel is fed with the voltage on the monitor resistor R_M whose phase is the same as that of the transmitter coil current. The instrument is controlled by a PC. Although D/A outputs of the LIAI can be used to control the XY scanner, scanning speed is limited with the data conversion time of the D/A converters of the LIAI. As an alternative, a PIC16F877

times. The properties of the EG&G Model 5209 Lock-in Amplifier Instrument can be summarized as follows:

- It has an oscillator output of 0.5 Hz to 120 KHz with 0.5 % total harmonic distortion with a maximum output of $2 V_{RMS}$ and 600Ω impedance, which is used to feed the power amplifier.
- The reference channel which is supplied by the transmitter coil current, allows inputs of $100 mV_{RMS}$ to $5 V_{RMS}$ with $1 M\Omega$ ac input impedance parallel with 30pF. The maximum allowed input is $30 V_{PP}$ without causing any damage.
- Input impedance is $100M\Omega$ parallel with 25pF.
- Two 16-bit D/A Converter outputs are provided which may be used to drive step motors of the XY scanning system. Maximum load is 5 mA up to $\pm 15V$.
- It is equipped with three different tracking filters: Notch, Bandpass, Lowpass. The filtering frequency is either selected automatically with the reference signal frequency or can be adjusted manually. In addition to these, there are also two power line notch filters with frequencies 50 Hz and 100 Hz.
- CMRR of the amplifier is typically 120dB at 1 KHz.
- An RS-232 DB25S DTE connector is present at the rear panel which allows the LIAI to be controlled via computer.
- In this study, the GPIB port which is present at the rear panel is used to control the LIAI via computer.

The LIAI settings used in this study are listed in Table 3.1.

Table 3.1: The LIAI settings.

Properties	Values
Filters	Bandpass, Track
Line Reject	F, 2F
Oscillator Frequency	14.1 kHz
Reference Phase	0°
Reference	External (Int extinguished)
Time Constant	30 or 100 ms
Slope	12 dB
Dyn. Res.	Norm

3.2.2 Nulling Circuit

The signal due to the conducting body is usually too small compared to the residual voltage caused by the primary coupling. There should be a nulling circuit to cancel the effects of the residual voltage (Figure 3.2) so that the signal due to conductive body can be amplified with a high amplification factor. For this purpose, a manually adjusted nulling circuit is designed and implemented. A signal in equal amplitude and phase of the residual signal is generated and subtracted from the residual signal to provide zero residual voltage. The signal on the monitor resistor is used for this purpose since amplitude and phase of this signal is steady and is taken as a reference during data acquisition. The signal is first amplified by manually adjusted amplifier P1, then is fed into cascaded, adjustable phase lag circuits with unity gain indicated as P2, which is capable of producing approximately 350° phase shift in total.

Although it is not applied in the nulling circuit, a suggestion is to put the phase shifter block before the amplifier block since the phase shifter circuit can not

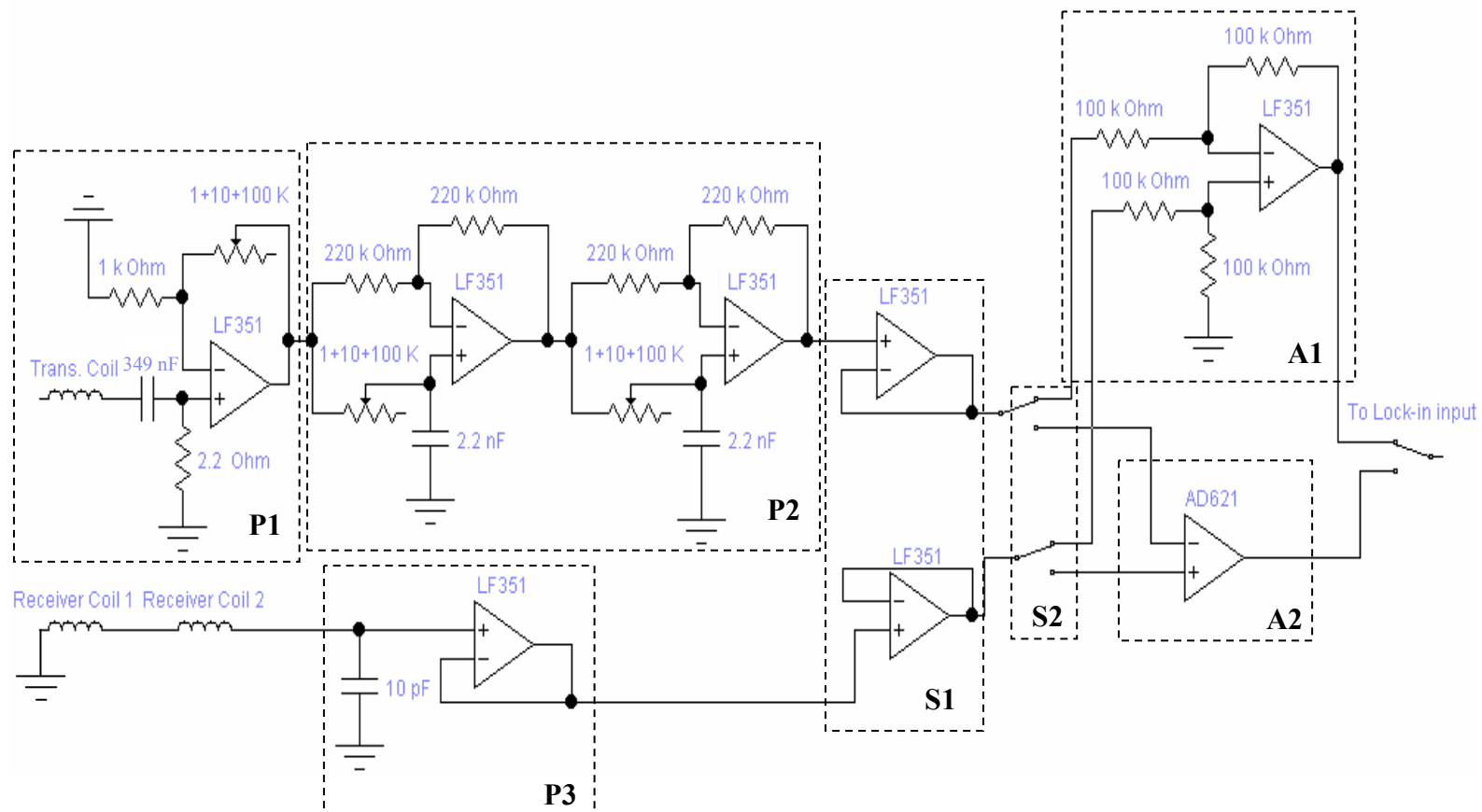


Figure 3.2: The nulling circuit diagram. Trans. Coil: Transmitter coil output, Lock-in input: LIAI input channel.

handle signals higher than $15 V_{PEAK}$ at 14.1 kHz. If the phase shifting operation is done before the amplification, the distortion problems arising in the phase shifter block can be eliminated

The cascaded amplifier and phase shifter blocks produce a signal whose magnitude and phase are the same with that of the residual signal. This signal is buffered in S1 to achieve equal and high input resistances for differential stages A1 or A2 as seen from the outputs of stages P2 and P3. The switches in S2 allow the selection of one of the two different differential amplifiers, A1 and A2, respectively. A1 is made of four 100 k Ω resistors and an op-amp (LF351) with unity gain, while A2 consists of AD621 which is a differential amplifier package with laser-trimmed resistors included, eliminating the usage of extra circuit elements. Differential gain can be either 10 or 100. AD621 is chosen for its application simplicity and for high common mode rejection ratio (93 dB at 1 kHz).

The amplification and shifting operations are performed with manually controlled potentiometers. The resulting signal is subtracted from the residual signal and passed through a buffer S1, connected to the input of a unity gain differential amplifier A1. In some experiments, the output of S1 is switched to A2 when higher gain is needed. The residual signal becomes 30 mV_{PEAK} when the nulling circuit is employed. Consequently, 99.57% cancellation is possible with this circuit.

3.3 Phase Sensitive Detection System using Data Acquisition Card

As an alternative to phase sensitive measurement system constructed with the LIAI and the nulling circuit, a phase sensitive detection circuit is designed and is constructed on PCB which is called as the data acquisition card (DAcC). PCB is copper-poured and is put in a metal box to minimize interaction and noise. All ICs' power supply pins are protected against supply voltage noise using 10 nF capacitors soldered right between the supply pin of the IC and the ground. Block diagram of DAcC is drawn in Figure 3.3. Pin locations diagram of DAcC is given in Figure 3.4. Detailed circuit connections are shown in the figures Figure 3.5 to Figure 3.24.

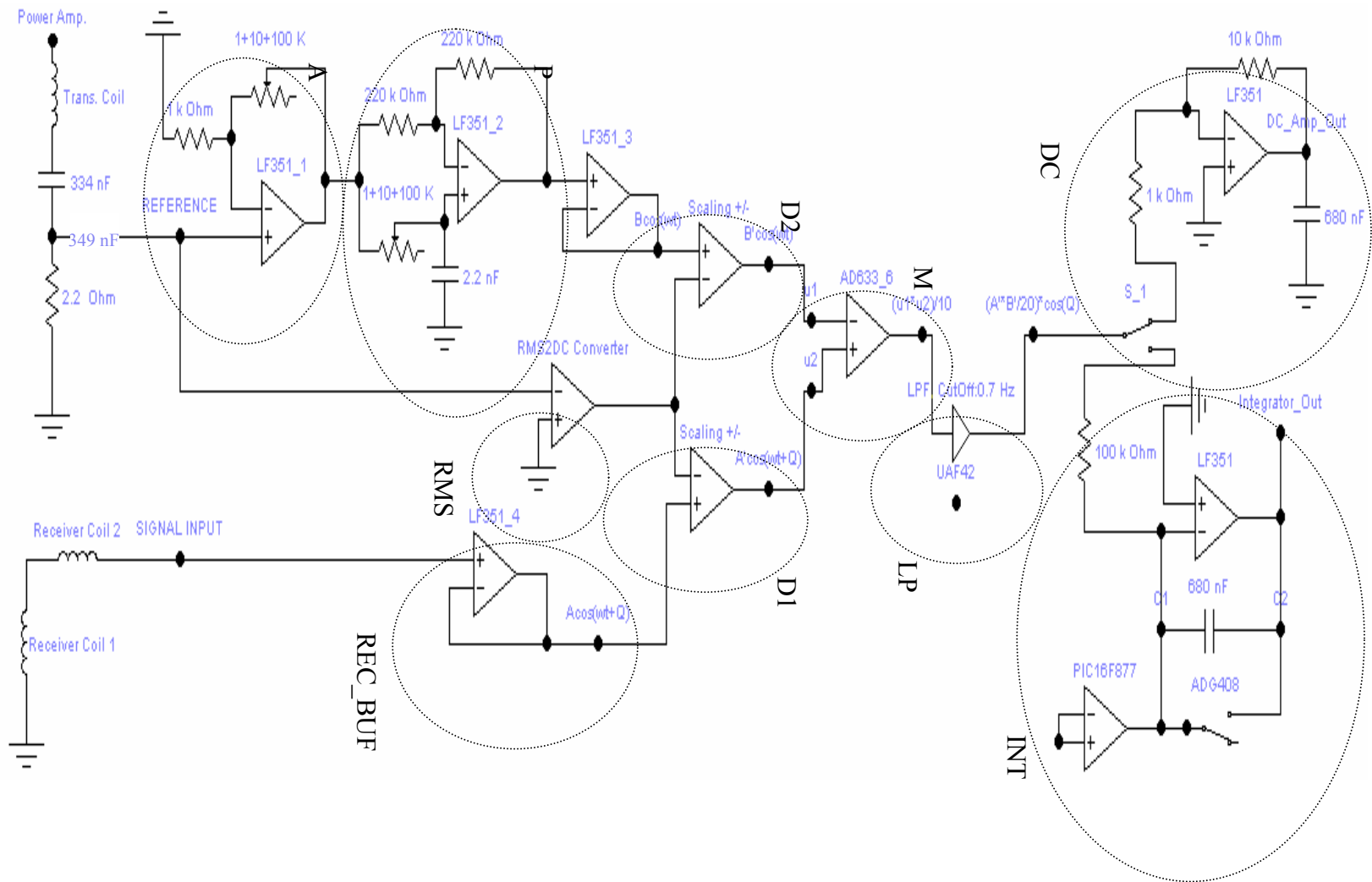


Figure 3.3: The Data Acquisition Card (DAC). A: Amplifier, P: Phase Shifter, D1& D2: Divider, RMS: RMS to DC Converter, REC_BUF: Receiver coil signal buffer, M: Multiplier, LP: Low Pass Filter, DC: Amplifier, INT: Integrator.

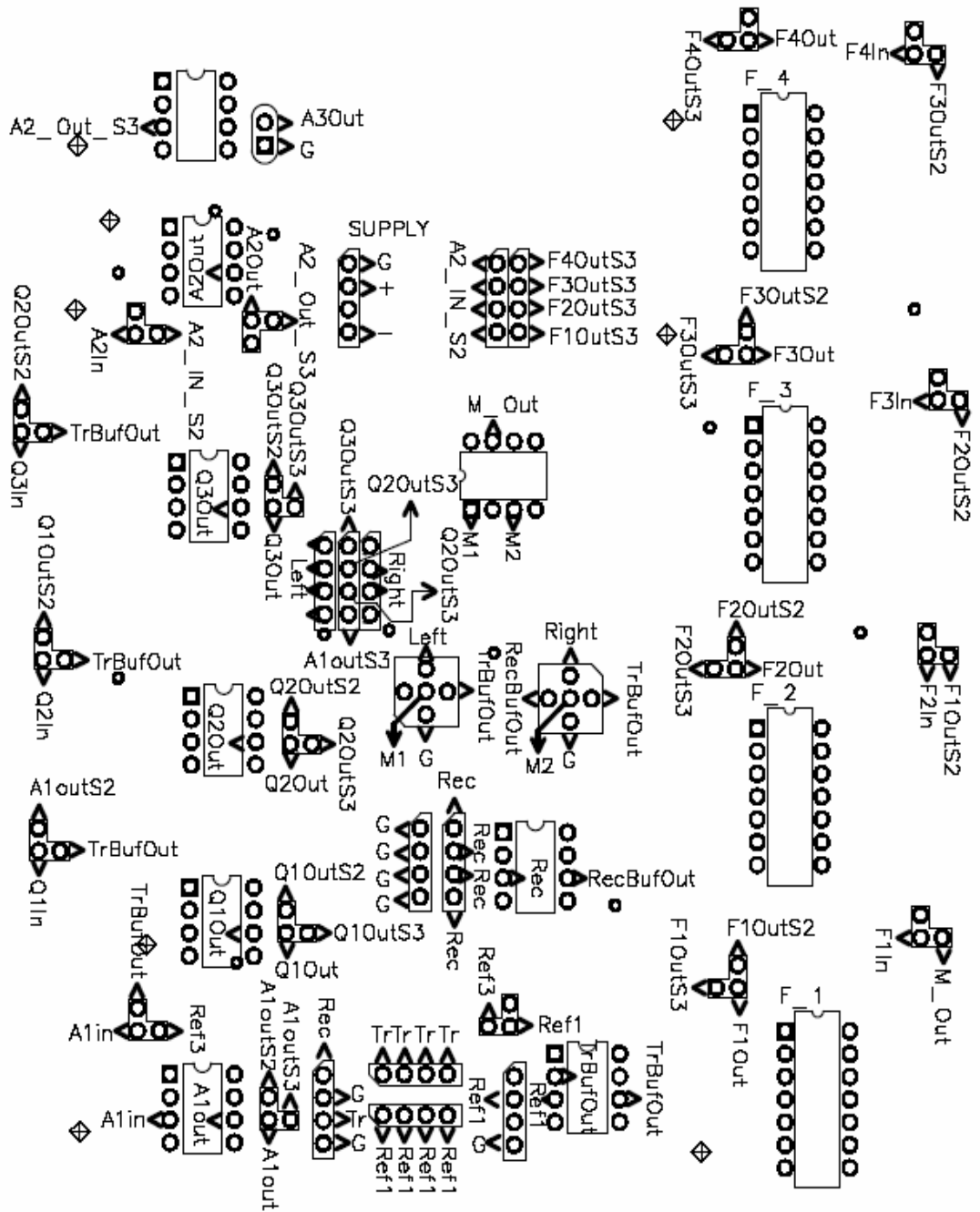


Figure 3.4 : Locations of pin connectors in the DACC.

The DA_C has two input channels: the reference and the signal input. Signal at the reference channel is the monitor resistor (R_M) voltage created by transmitter coil current. This signal is buffered by the Transmitter Coil Input Buffer (Figure 3.5).

Reference signal's amplitude and phase can be manually adjusted using the amplifier and phase shifter blocks in the DA_C, indicated as A and P respectively in Figure 3.3. The amplifier and three available phase shifter blocks (Figure 3.6 to Figure 3.9) can be cascaded using the connectors placed on the PCB in case alternative connection schemes are needed. Input and output of each block is available at a pin socket making the blocks selectable for different ways of cascading. Outputs of the amplifier and phase shifter blocks are available at output selection block given in Figure 3.10. Selected output is transmitted to the scaling circuitry, namely D2 (Figure 3.3). As shown in Figure 3.3, output of the phase shifter block, P is scaled with the rms of the reference voltage in D2, in case amplitude of the reference voltage varies due to fluctuations in the output of the power amplifier.

The signal coming from the differentially connected receiver coils are given to the 'Signal Input' buffer of the DA_C (Figure 3.11). Buffered receiver coil signal is scaled by the rms value of the receiver coil signal in D1 because of the same consideration about the reference voltage mentioned above. Circuit for the divider part is given in Figure 3.12. Divider circuit for the transmitter buffer output is given in Figure 3.13. Rms of the reference voltage is obtained by the RMS to DC converter block indicated as RMS in Figure 3.3. For this purpose AD536 produced by Analog Devices is employed as shown in Figure 3.14.

Rms to DC converter and divider circuits are constructed on a different card and signal transmission between two cards are achieved by cables which carry the incoming and outgoing signals between the MULT_IN_1, MULT_IN_3 sockets (Figure 3.15) and the second card. Scaled signals at the output of D1 and D2 are multiplied in the multiplier constructed with AD633 (Figure 3.16). Multiplier is named as M in Figure 3.3.

Output of the multiplier is given to the low pass filter block LPF (Figure 3.3), constructed with a UAF42 whose cutoff frequency is adjusted to be 0.7 Hz. Up to four low pass filters can be used in cascaded form by connecting the output of one to the input of the other by use of the sockets available on PCB (Figures 3.17 to 3.20).

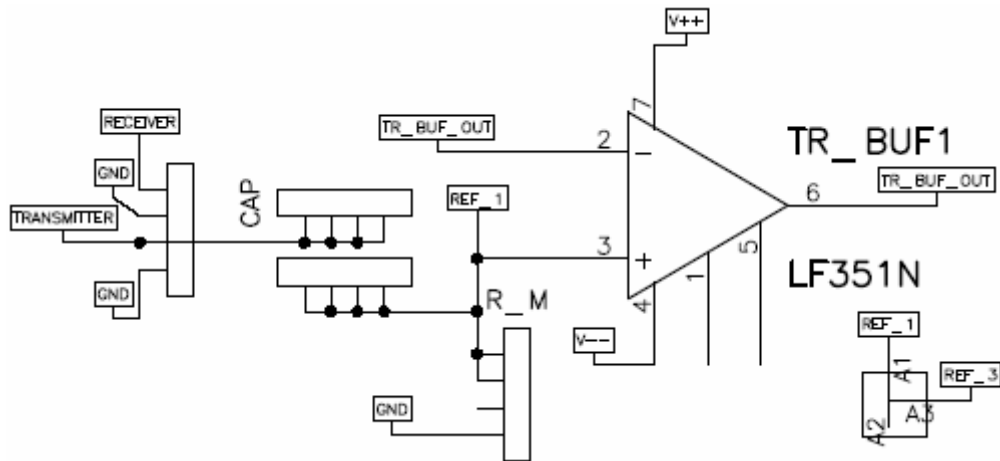


Figure 3.5: Transmitter Coil Current Buffer. Transmitter coil current entering the DAC at ‘TRANSMITTER’ flows through the 349 nF capacitor connected between the sockets indicated as CAP and then passes from the monitor resistor (R_M) in R_M socket and flows to the ground. Voltage on the monitor resistor (REF_1) is in phase with the transmitter current and is taken as the reference voltage. When REF_1 is connected to REF_3, unbuffered reference voltage is available at the REF_3 input of the amplifier A1.

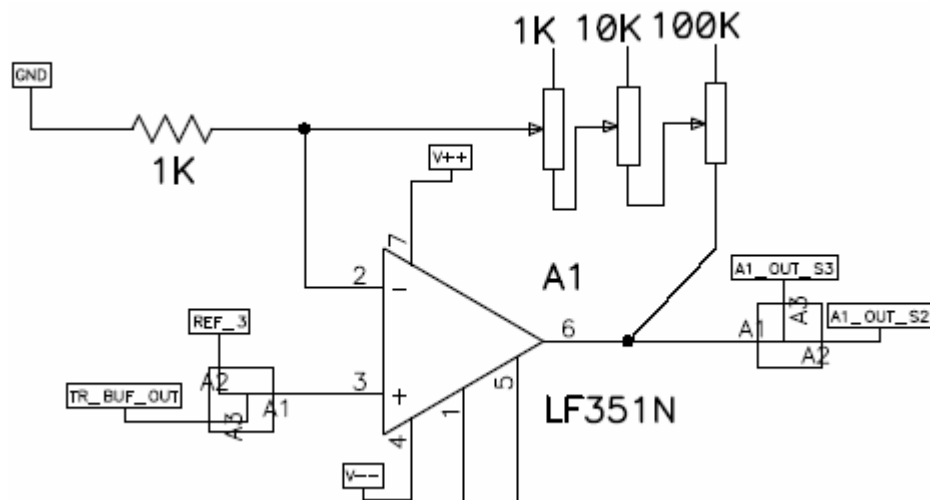


Figure 3.6: Amplifier, A1 circuit connections. This circuit is indicated as A in Figure 3.3. Buffered, namely TR_BUF_OUT or unbuffered monitor resistor R_M voltage, namely REF_3 can be selected as input of the amplifier block A1. Output of A1 can be led to A1_OUT_S3 which is one of the four selectable outputs (outputs of A1 and phase shifter blocks Q1, Q2, Q3) at QA4_SELECT socket (Figure 3.10); or to A1_OUT_S2 which goes to input socket of phase shifter block Q1.

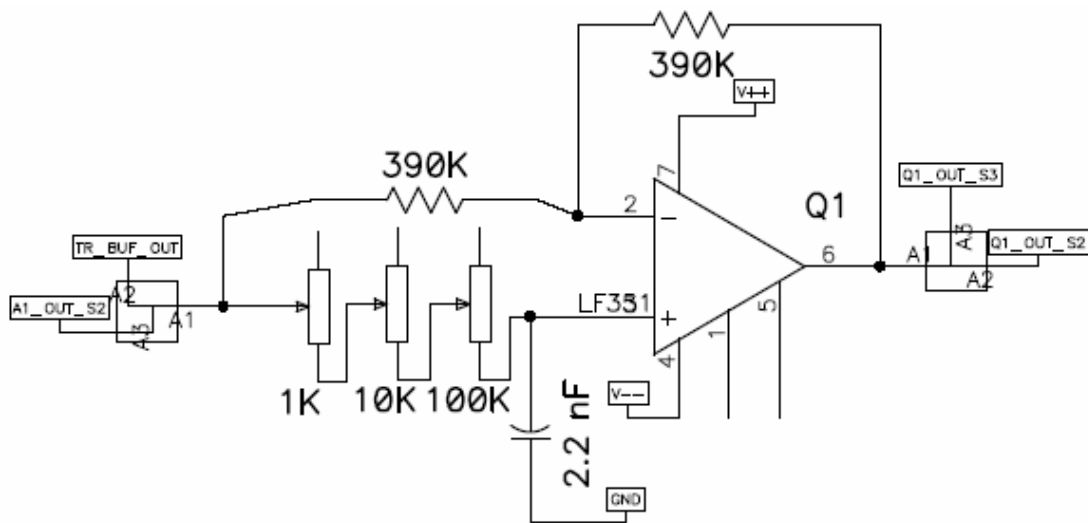


Figure 3.7: Phase shifter Q1 circuit connections. Its input can be selected to be the buffered monitor resistor (R_M) voltage TR_BUF_OUT or the output of the amplifier A1 which is A1_OUT_S2. Output of Q1 can be led to QA4_SELECT connector (Figure 3.10) via Q1_OUT_S3 or to input of phase shifter Q2 via Q1_OUT_S2. In the phase shifter blocks switching the positions of the 2.2 nF capacitor and the 1+10+100 k Ω potentiometers results in the phase shifter to be a phase lag or phase lead circuit.

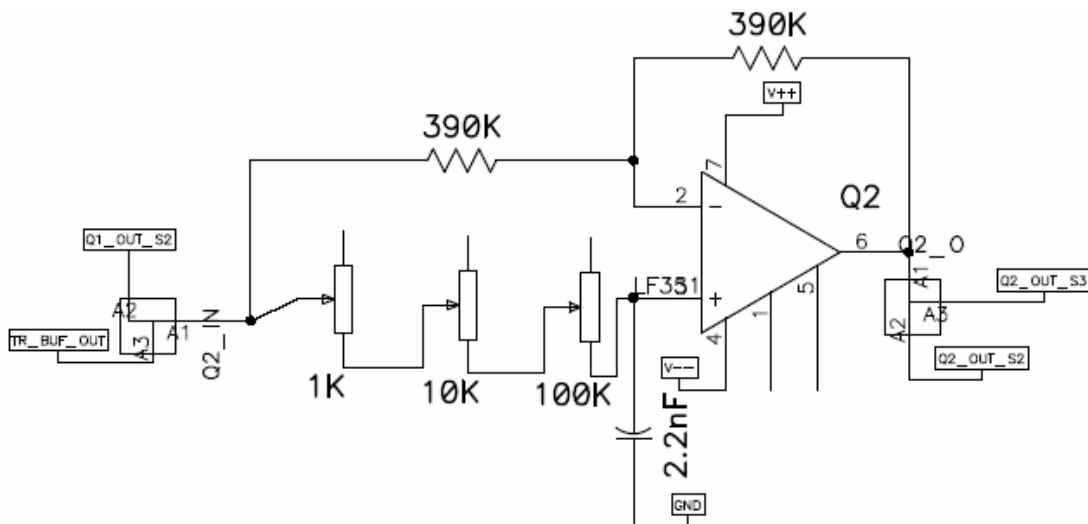


Figure 3.8: Phase shifter Q2 circuit connections. Its input can be selected to be the buffered monitor resistor (R_M) voltage TR_BUF_OUT or the output of the phase shifter block, Q1 which is Q1_OUT_S2. Output of Q2 can be led to QA4_SELECT connector (Figure 3.10) via Q2_OUT_S3 or to input of phase shifter Q3 via Q2_OUT_S2.

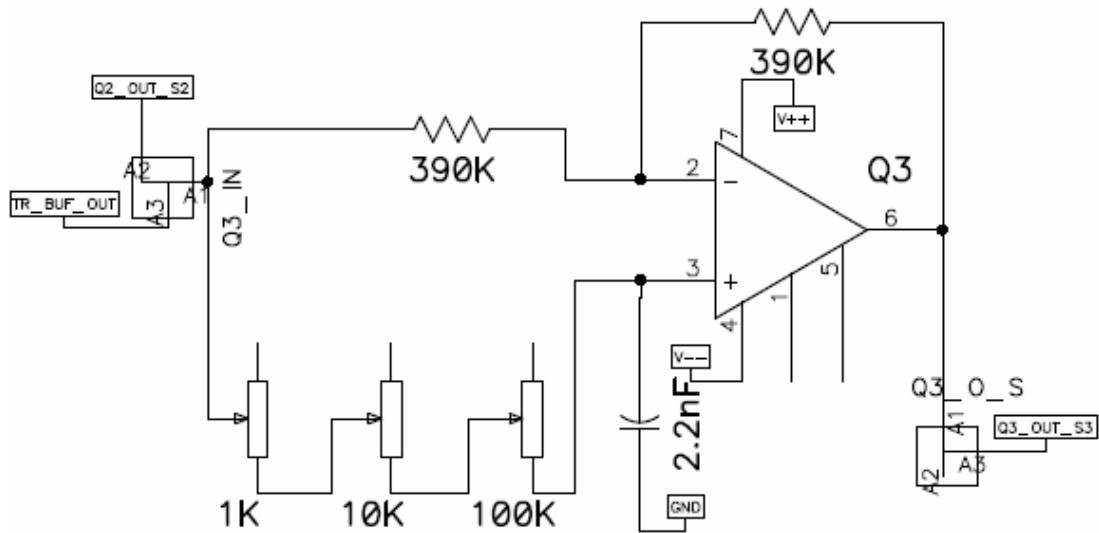


Figure 3.9: Phase shifter Q3 circuit connections. Its input can be selected to be the buffered monitor resistor (R_M) voltage TR_BUF_OUT or the output of the phase shifter block, Q2 which is Q2_OUT_S2. Output of Q3 can be led to QA4_SELECT connector (Figure 3.10) via Q3_OUT_S3. Cascaded Q1, Q2 and Q3 blocks are named as P in Figure 3.3. Cascaded three phase shifter blocks can produce approximately $3 \times 175 = 525^\circ$ phase shift, in total.

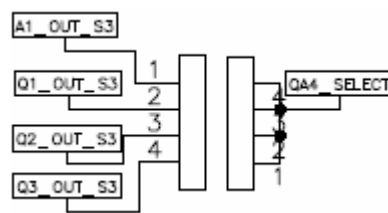


Figure 3.10: QA_SELECT Connector circuit connections. One of the four outputs at the left hand side can be selected by shorting related output signal pin with the QA_SELECT pin which is close to it.

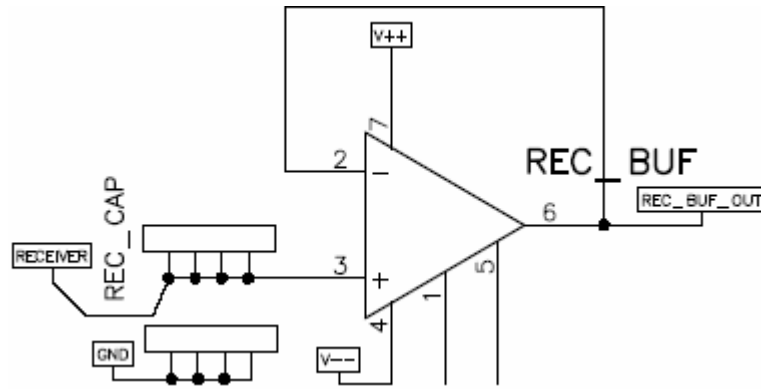


Figure 3.11: Receiver coil signal buffer circuit connections. This part is indicated as REC_BUF in Figure 3.3. Output of the differentially connected coils is given to the DAC via RECEIVER channel. Socket block named as REC_CAP is available in case capacitors between V₊ input of the buffer and ground are needed to load the receiver coils.

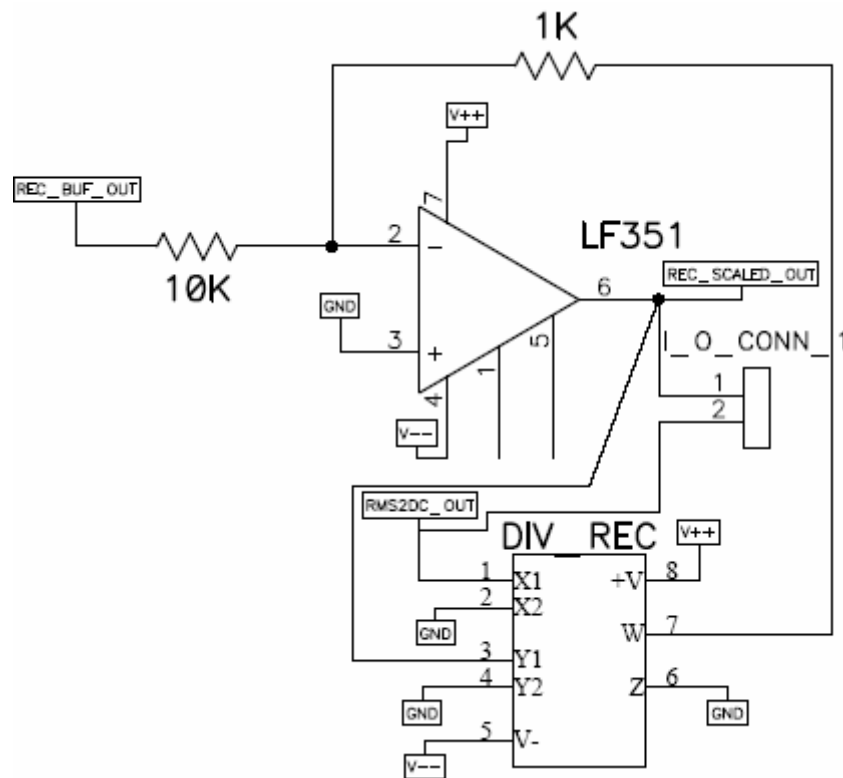


Figure 3.12: Divider circuit for the receiver coil buffer output. This is called as D1 in as shown in Figure 3.3. Receiver coil buffer signal is scaled with the rms of the reference signal. AD633 is employed as the divider IC. Feedback resistor is taken as 1 k Ω instead of 10 k Ω to decrease the output gain from 10 to 1. Scaled receiver coil signal is given to the multiplier IC input MULT_IN_3 as shown in Figure 3.16.

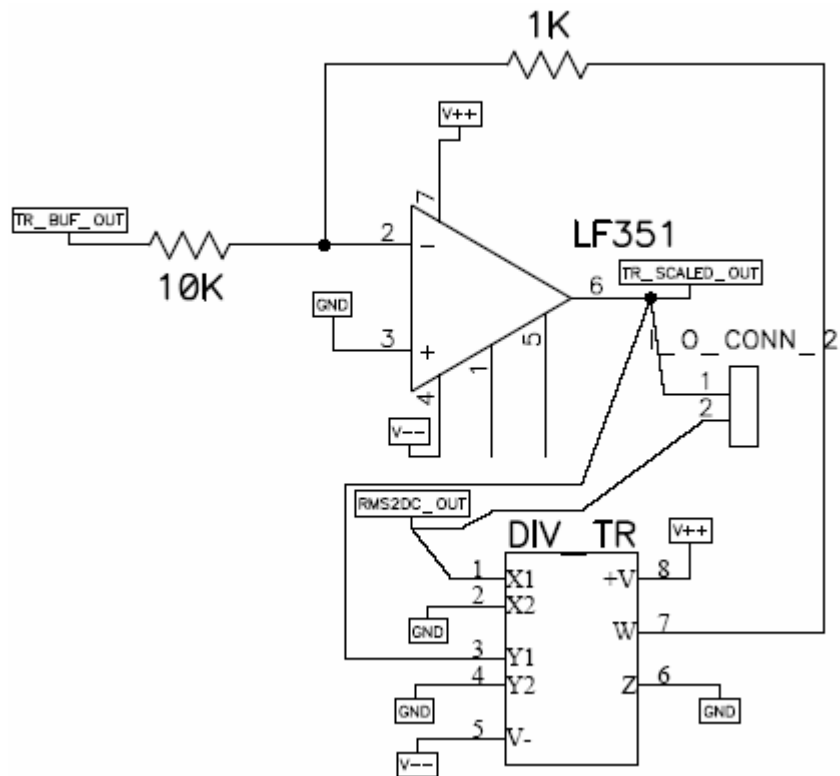


Figure 3.13: Divider circuit for the transmitter buffer output. This circuit is represented as D2 in Figure 3.3. Transmitter coil buffer signal is scaled with the Rms of the reference signal. AD633 is employed as the divider IC. Feedback resistor is taken as 1 kΩ instead of 10 kΩ to decrease the output gain from 10 to 1. Scaled reference signal is given to multiplier IC input MULT_IN_1 as shown in Figure 3.16.

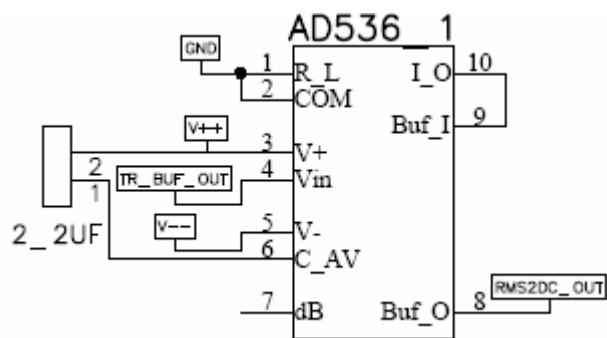


Figure 3.14: Rms to DC Converter circuit connections. At the output rms value of the reference voltage is obtained. 2.2 μF is used between V+ and C_AV. This circuit is named as RMS in Figure 3.3.



Figure 3.15: Signal selection pin connector blocks. MULT_IN_1 multiplexes one of the three available signals to the X1 input of the AD633 multiplier. MULT_IN_3 multiplexes one of the three available signals to the X2 input of the AD633 multiplier. X1 and X2 are 1st and the 3rd pins of AD633, respectively.

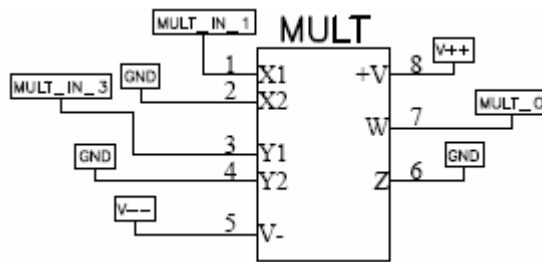


Figure 3.16: Multiplier circuit connections. AD633 is employed to multiply the scaled reference voltage and scaled receiver coil signal which are available at MULT_IN_1 and MULT_IN_3 pins, respectively.

In the application, only the first filter stage named as F_1 is used. To decrease the cutoff frequency of F_1, external 220 nF capacitors are connected in parallel to the internal 1000 pF capacitors buried in the filter IC [73] (Pages 1 and 6).

To make multiplication and low pass filtering process clearer, assume two signals at the same frequency with different amplitudes and whose phase differs by ϕ . That is, let the input signal be $A'\cos(\omega t + \phi)$ and reference signal be $B'\cos(\omega t)$. Using the trigonometric identity, multiplication of these two terms is obtained as $\frac{1}{2}A'B'[\cos(2\omega t + \phi) + \cos(\phi)]$. After low pass filtering, the high frequency term drops and one gets $\frac{1}{2}A'B'\cos(\phi)$. Keeping B' as unity, $1/2A'\cos(\phi)$ yields the component of the input signal in phase with the reference signal. Thus in the DAC, at the output of the low pass filter, the amplitude of the in phase component of the receiver coil is extracted. To amplify this dc signal, an amplifier circuit constructed

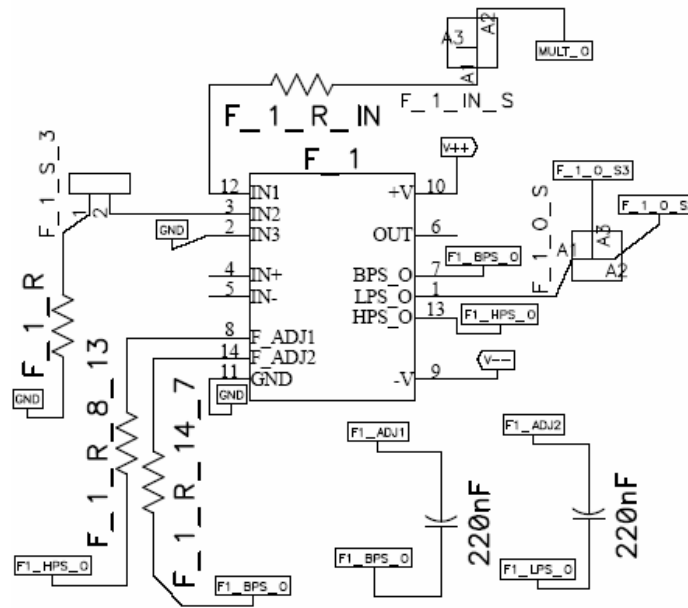


Figure 3.17: Low Pass Filter circuit connections. Input to this circuit, comes from the output of the multiplier shown as MULT_O. At the output F_1_O_S3 carries the output of F_1 to input of the next filter stage F_2 or F_1_O_S2 carries the output of F_1 to input selection pin connector block, A2_IN_S2 which is given in Figure 3.21.

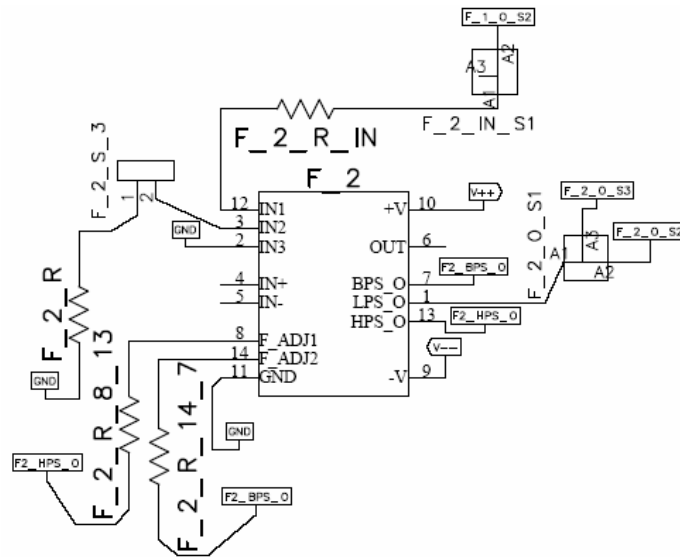


Figure 3.18: Low Pass Filter circuit connections. Input to this circuit comes from the output of the filter F_1 as shown as F_1_O_S2. At the output F_2_O_S3 carries the output of F_2 to input of next filter stage F_3 or F_2_O_S2 carries the output of F_2 to input selection pin connector block A2_IN_S2 (Figure 3.21).

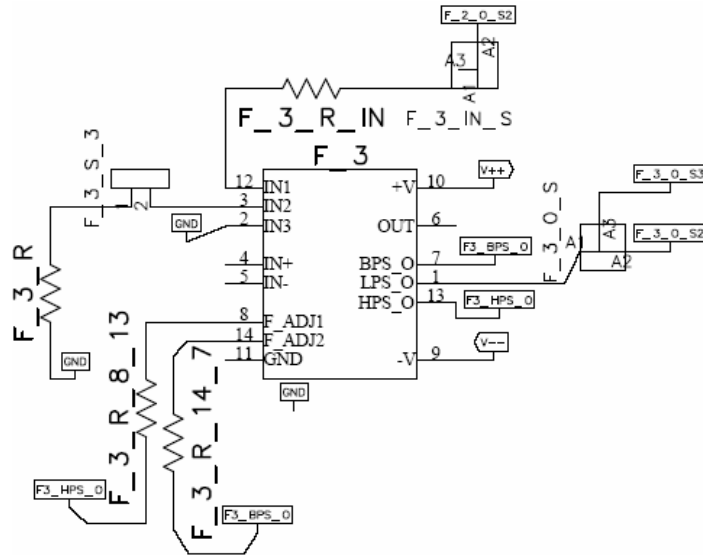


Figure 3.19: Low Pass Filter circuit connections. Input to this circuit, comes from the output of the filter F₂ as shown as F₂_O_S2. At the output F₃_O_S3 carries the output of F₃ to input of next filter stage F₄ or F₃_O_S2 carries the output of F₃ to input selection pin connector block A2_IN_S2 (Figure 3.21).

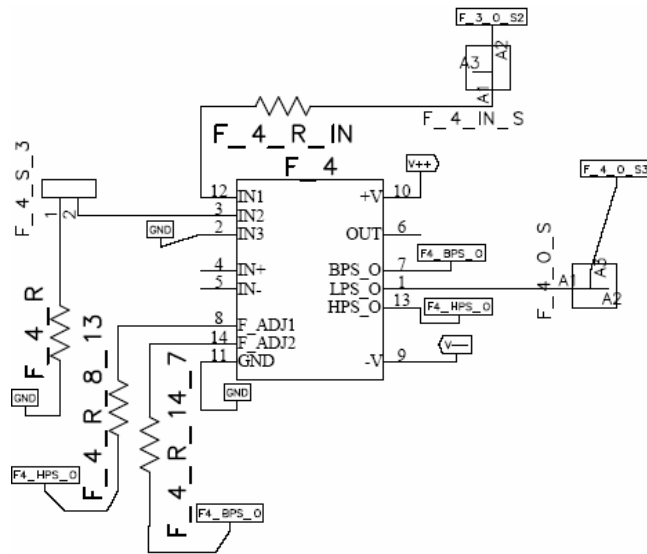


Figure 3.20: Low Pass Filter circuit connections. Input to this circuit, comes from the output of the filter F₃ as shown as F₃_O_S2. At the output F₄_O_S2 carries the output of F₄ to input selection pin connector block A2_IN_S2 (Figure 3.21). Cascaded filter blocks are represented as LPF in Figure 3.3.

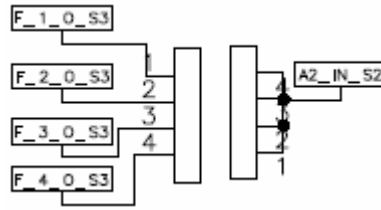


Figure 3.21: Input selection pin connector, A2_IN_S2. One of the filter outputs is given to the input of cascaded amplifier stages, A2 and A3 in the next stage.

with LF351 can be used (Figure 3.22). This amplifier stage is named as DC in Figure 3.3. A 680 nF capacitor is connected to the output of the amplifier to reduce the bandwidth eliminating high frequency terms since the aim is just to measure the dc signal obtained at the low pass filter output.

An integrator circuit can also be used to measure the dc signal indicated as INT in Figure 3.3. An ADG408 analog multiplexer IC is used as analog switch across the feedback capacitor of the integrator. Switching is controlled with PIC16F877 which communicates with the computer via RS232 port. E, enable pin of the multiplexer is connected to the D0 pin of the microcontroller. Multiplexer control bits are grounded, thus S1 pin of the multiplexer is internally connected to D pin when multiplexer is enabled. At times when integrator is not measuring, multiplexer is enabled by the microcontroller by default, closing the switch and shorting the feedback capacitor. This yields 0 mV at the output of the integrator. A data acquisition program written using HP VEE triggers PIC16F877 which disables the multiplexer to make the switch open; thus feedback capacitor is not shorted anymore and starts to get charged resulting in the gradual increase in the output voltage according to the dc level at the input of the integrator. Input dc level changes the slope during the rise of the output of the integrator. This way of measurement is considered to be more noise-immuned compared with the method of using a dc amplifier to measure the dc output of the low pass filter. Rising signal generated by the integrator as the output of the DAC is measured using an Agilent digital multimeter HP34401A which can communicate with the PC via GPIB port. Rising speed of the output voltage of the integrator is adjusted by the resistor and capacitor

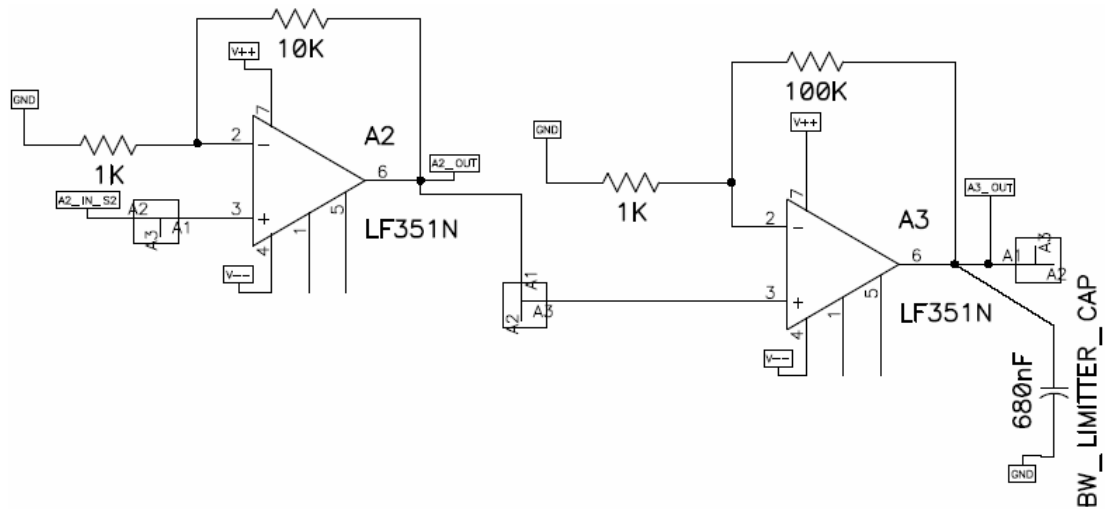


Figure 3.22: Amplifier circuit connections. Total amplification factor of *1000 is available with this configuration. Two amplifiers with gain values of *10 and *100 are used in cascaded form to avoid the instability that might occur due to usage of a single amplifier stage with gain of *1000.

used around the opamp of the integrator, whose values are 100k Ω and 680 nF respectively. For these values, the time constant (τ) is calculated as 100 k Ω * 680 nF which is 68 msec.

Circuit diagrams of the integrator and the μ controller is given in Figure 3.23 and Figure 3.24, respectively.

3.4 Coils

Receiver coil 2 has the following electrical properties: 1219 mH, 3.509 k Ω whereas Receiver coil 1 is 1228 mH and 3.512 k Ω . Series differential connection of the receiver coils gives 2219 mH and 7.008 k Ω . Both receiver coils are 10000 turns wound on a delrin rod whose outer diameter is 30 mm. The 200-turn-transmitter coil has such properties: 365.1 μ H, 3.97 Ω . Wire diameter of the receiver coils is 0.06 mm while the wire used in the transmitter coil is 0.5 mm in diameter. Transmitter's outer diameter is 30 mm. Inner diameters of the three coils are the same and are equal to 7 mm. There is a hole of 5 mm in diameter passing through the center of each coil

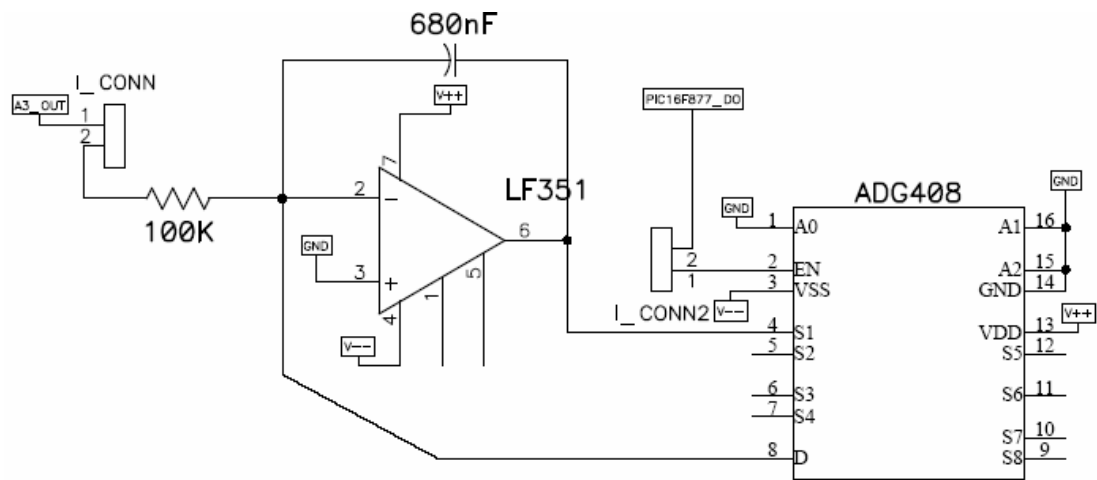


Figure 3.23: Integrator circuit connections.

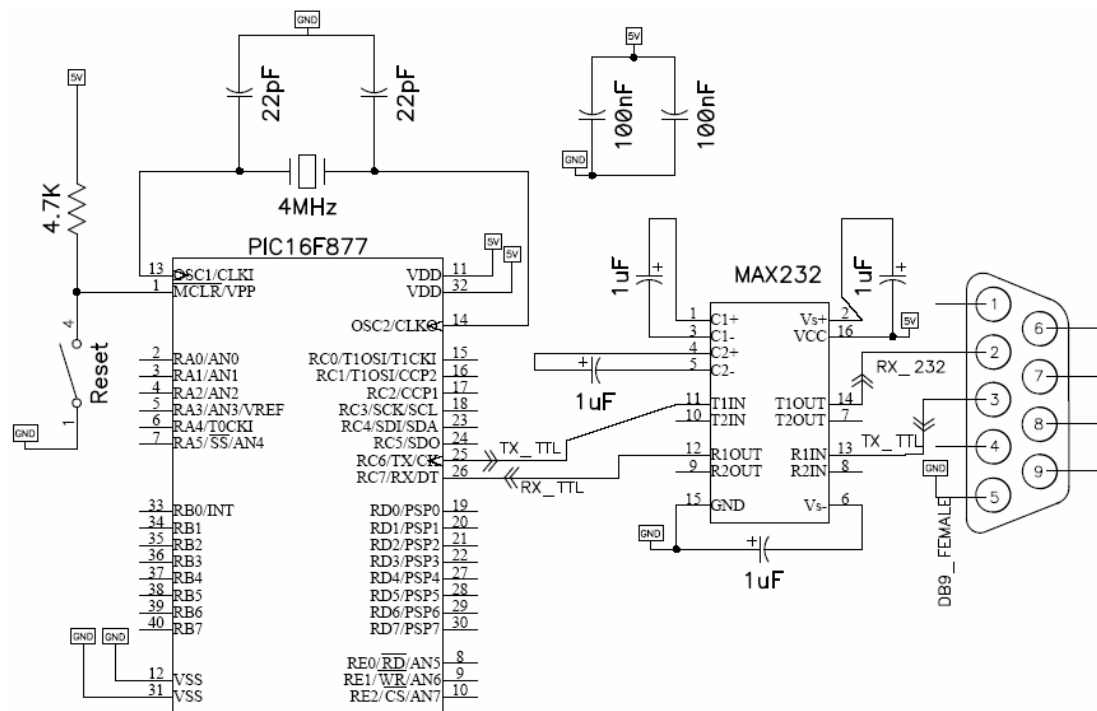


Figure 3.24: PIC16F877 Microcontroller circuit. The same circuit is employed where ever μ controller is needed.

3.5 Power Amplifier

To excite the transmitter coil a power amplifier is employed. The power amplifier (Figure 3.25) is capable of driving $\pm 25\text{V}$ at $\pm 10\text{A}$ while operating from $\pm 30\text{V}$ supplies. The monolithic IC used is LM12 operational amplifier which can deliver 80 W of sine wave power into a $4\ \Omega$ load with 0.01% distortion. Power bandwidth is 60 kHz. Further properties of the IC can be explored from its datasheet. The power amplifier is fed with $\pm 17.5\text{V}$ from a DC power supply (Farnell PDD3010A). The transmitter coil has a DC resistance of $3.97\ \Omega$ therefore, a power resistor of $2.2\ \Omega$ (5W) is connected in series with the coil since the power amplifier is capable of driving a minimum $4\ \Omega$ load. In addition to the resistance, a capacitance of 349 nF is connected for tuning purposes. Power amplifier input is fed with the oscillator output of the Agilent function generator HP33120A with 0.723 V at 14.1 kHz.

Since the output resistance of the oscillator output of the LIAI is $600\ \Omega$ and the power amplifier has $1\ \text{K}\ \Omega$ resistance at the input stage, a buffer is needed to make the connection between these two. A buffer is constructed using LF351. The current supplied by the power amplifier to the transmitter coil is $200\ \text{mA}_{\text{PEAK}}$.

3.6 XY Scanner System

To scan the probe over the phantom a computer controlled XY scanning system designed and implemented in [53] is used. The system is made up of all delrin (except step motors) to avoid artifacts. The probe motion is controlled by two step motors, which are controlled by a step motor driving circuit that is fed by a PIC microcontroller. The working principle of a step motor can be summarized as follows:

A step motor is an electromechanical device which converts electrical pulses into discrete mechanical movements. The shaft of a step motor rotates in discrete

steps increments when electrical pulses are applied in the proper sequence. Applied sequence controls the direction of the motor, the frequency and length of the rotation.

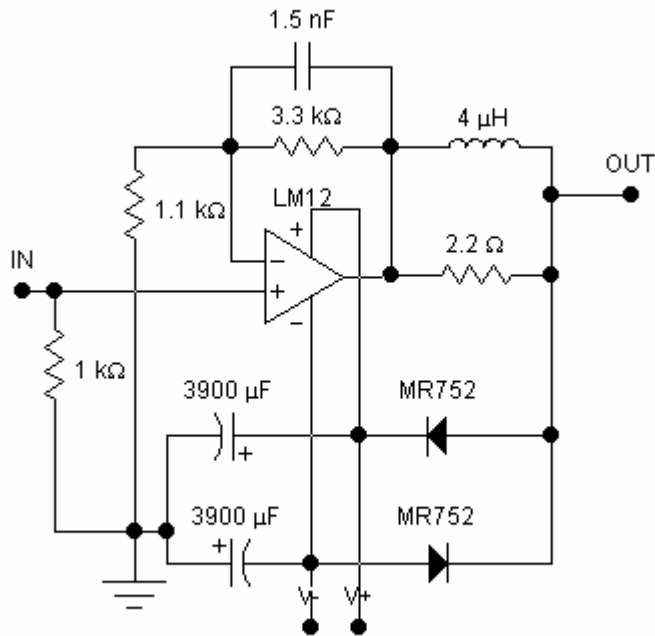


Figure 3.25: The power amplifier circuit diagram.

As a result we need a circuit (driver circuit) that can give the necessary pulses to the windings of the step motor (Figure 3.26). A step motor is a good choice when controlled movement is desired. It finds applications where control of the rotation angle, speed, position and synchronism is needed.

Experimentally it is observed that step motors used in this study can move a step at rate of 400 Hz at maximum without missing the sequence. The step angle of the motors is 1.8° which means that when the motor shaft moves a single step, shaft rotates 1.8° for each step. Thus a complete rotation requires $360^\circ / 1.8^\circ = 200$ steps. 400 Hz of stepping frequency means 2 complete rotations per second which is the mechanical limit for our motors.

The circuitry is composed of two parts: First part consists of PIC16F877 microcontroller which produces the necessary digital voltage levels for the driver circuit and the second part is the main driver circuit.

The switching sequence of the terminals of the step motor to rotate in clockwise (CW) or counterclockwise (CCW) is shown in Figure 3.27, where "-" means ground, " " means open connection and "+" means positive power supply (Since the motors used here are 3V step motors "+" means 3V in this circuit). Examining Fig. 3.26 shows that the voltage levels in nodes D7_1, D6_1, D5_1 and D4_1 (D3_2, D2_2, D1_2, D0_2 for the other motor driver) controls the voltage levels in the terminals 1, 3, 2 and 4 respectively. i ($i=1$ or $i=2$) in Dk_i represents the motor number while $k=\{0_{\text{LSB}}, 1, 2, 3, 4, 5, 6, 7_{\text{MSB}}\}$ represents the Port D bit number of the microcontroller from the least significant (LSB) to the most significant bit (MSB). Analyzing the circuit shows that to set a terminal to ground "+5V" should be applied to its control input, and to set it to no connection "0V" should be applied. In accordance with this idea the voltage sequence that should be applied to the control inputs D7_1, D6_1, D5_1 and D4_1 is shown in Figure 3.27. The microcontroller will generate these necessary voltage sequences at its Port D pins. For this purpose D7_1, D6_1, D5_1 and D4_1 terminals are connected to the data outputs of RD7_{MSB}, RD6, RD5 and RD4 of the microcontroller, respectively (For the second motor D3_2, D2_2, D1_2 and D0_2 terminals are connected to the data outputs of RD3, RD2, RD1 and RD0_{LSB} of the microcontroller respectively). Microcontroller circuit schematic is the same as given in Figure 3.24. Microcontroller can communicate with PC via RS232 port. As a result it is possible to control XY scanning system with the help of PC and HP VEE program. Since there are two step motors (one for X movement and one for Y movement) these two circuits should work in synchronization. The synchronization is achieved with the software. The scanning system has a minimum step size of 0.3 mm. It requires totally 2.5 seconds for the probe to move from a measurement point to another which is 1 cm away and record the output. Thus it takes $2.5 \times 17 \times 17 = 722.5$ seconds to scan over a 17cm * 17cm square shaped area and to record measurements at 17*17 points over the same area. This period is shorter compared with the previous state of the scanner. Shortening the data acquisition time might be critical in the scanning experiments of biological tissues or living animals. Appearance of the system can be viewed in Figure 3.28.

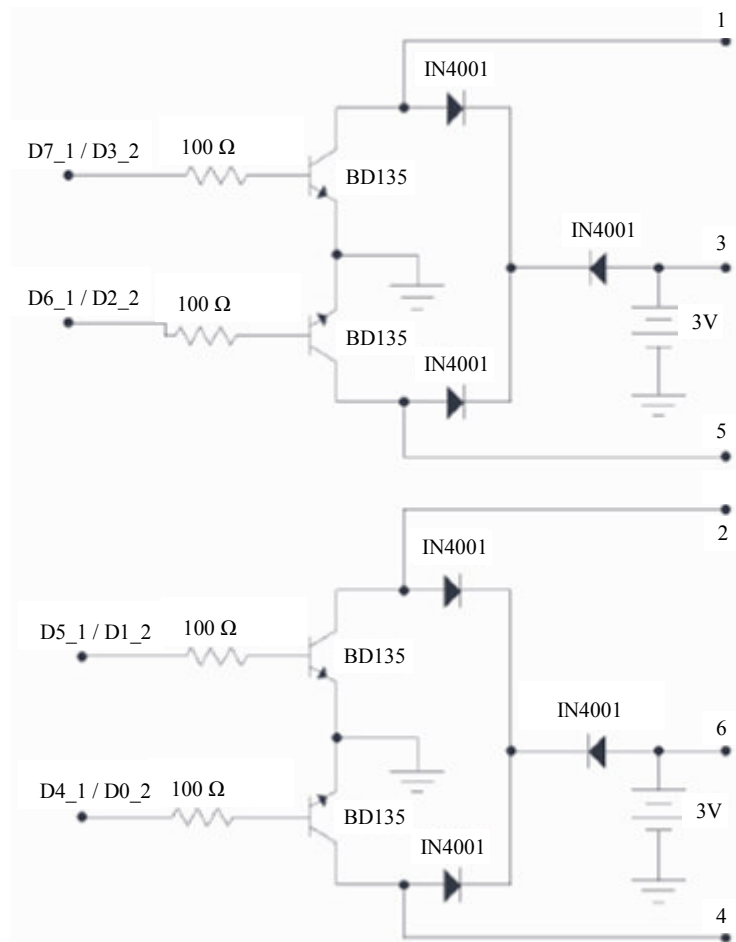


Figure 3.26: Step motors driving circuitry.

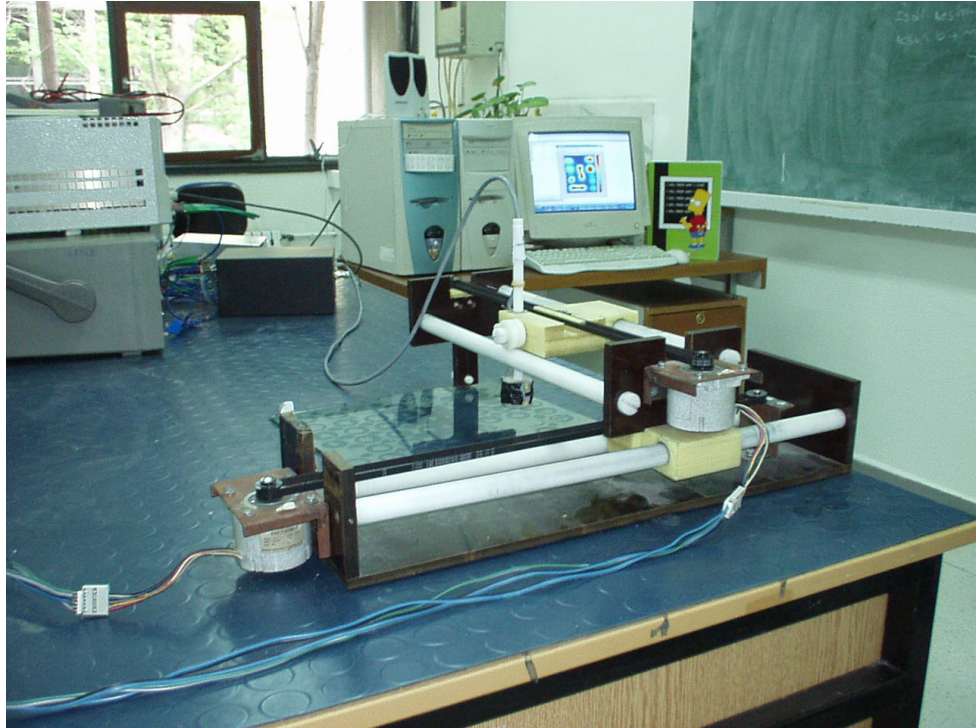
	1	3	2	4	5/6
1	-		-		+
2	-			-	+
3		-		-	+
4		-	-		+

Figure 3.27: The switching sequence of the step motor terminals.

3.7 RS-232 Port Programming

In this study when communicating with the LIAI via RS-232 handshaking is used with 9600 baud rate, even parity, 7 data bits per byte, 1 stop bit. LIAI is associated with several commands to be used in the transmission [74].

Preparing microcontroller for the serial communication requires the registers of the microcontroller related to serial communication to be initialized. For asynchronous mode of the USART module (Universal Synchronous Asynchronous Receiver Transmitter) related registers are SPBRG, TXSTA, RCSTA, TXREG, RCREG, PIR, PIE. Loading SPBRG register with '19h' (hexadecimal) or equivalently '25' in decimal, UART (Universal Asynchronous Receiver Transmitter) baud rate is set to 9600 with a 4 MHz crystal. Loading TXSTA with b'00100100' (binary) settings of TXSTA becomes 'asynchronous mode (don't care), 8-bit data transmission, transmit enabled, asynchronous mode, unimplemented, high speed for asynchronous mode, TSR full, don't care'. Loading the receiver status register RCSTA with b'10010000' settings of RCSTA becomes 'Serial port enabled, 8-bit Reception, don't care (asynchronous mode), continuous receive enabled, address detection disabled, no framing error, no overrun error, don't care'. Thus initialization of UART module is complete. Microcontroller starts sending data as soon as TXREG (transmit register) is loaded. Data reception is recognized when receive register is full which yields the PIR1,5 namely RCIF flag bit to be set. Received data is stored in RCREG and is ready to be used in the program. To receive another data PIR1,5 must be cleared in the program. More information is available in [75] and [76]. Pin descriptions and connection scheme is given in Figures 3.29-3.31.



(a)



(b)

Figure 3.28: (a): Appearance of the XY Scanner, (b): The data acquisition system

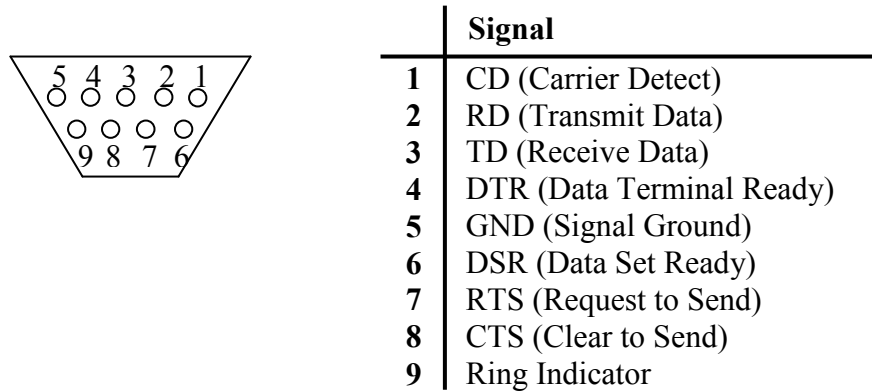


Figure 3.29: RS-232 DB09S Connector.

	Computer Side (Male)	Connection	MAX232 (µcontroller Side) (Female)
PIN1	CD	↔	Unused
PIN2	RD	↔	RD(↔ T1_Out of ax232)
PIN3	TD	↔	TD (↔ R1_In of max232)
PIN4	DTR		Unused
PIN5	GND		GND
PIN6	DSR		Unused
PIN7	RTS		Unused
PIN8	CTS		Unused
PIN9	Ring Indicator		Unused

Figure 3.30: RS-232 Connection Scheme used in this study (The connection scheme for the DB09S and the communication circuit given in Figure 3.24).

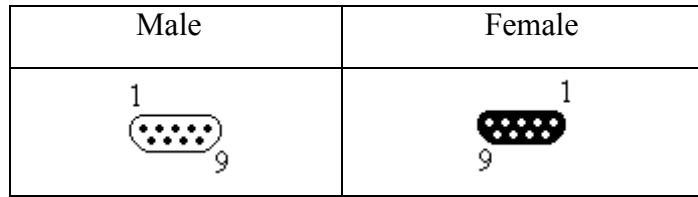


Figure 3.31: Standard 9-Pin RS-232 sockets [75].

3.8 Choice of the Excitation Frequency

Although high frequency is desirable (since the secondary voltage increases with the square of the frequency,) operating frequency should be lower than 100 kHz to decrease the capacitive coupling between the coils. Keeping the operation frequency below 50 kHz is generally applied in most of the EIT studies to avoid the effects of the stray capacitances [2]. At higher frequencies the wavelength becomes smaller and received signals from the various part of the body do not arrive in phase [78].

The frequency response of the system is found by using computer controlled LIAI in which the residue voltage is recorded with changing oscillator frequency applied to the power amplifier from 9 kHz to 100 kHz (Figure 3.32). It is observed that the residue signal gets its maximum value at 50 kHz with 1.1V. The operating frequency from Figure 3.32 is chosen as 14.1 kHz where the residual signal is 0.026V and transmitter coil current is 0.5 mA_{PEAK}. The transmitter coil is tuned to 14.1 kHz with a 349 nF capacitor so that it is possible to pass more current through the transmitter coil. With this tuning the current in the transmitter coil and the residue voltage increases to 400 mA_{P-P} and 7V_{PEAK}, respectively.

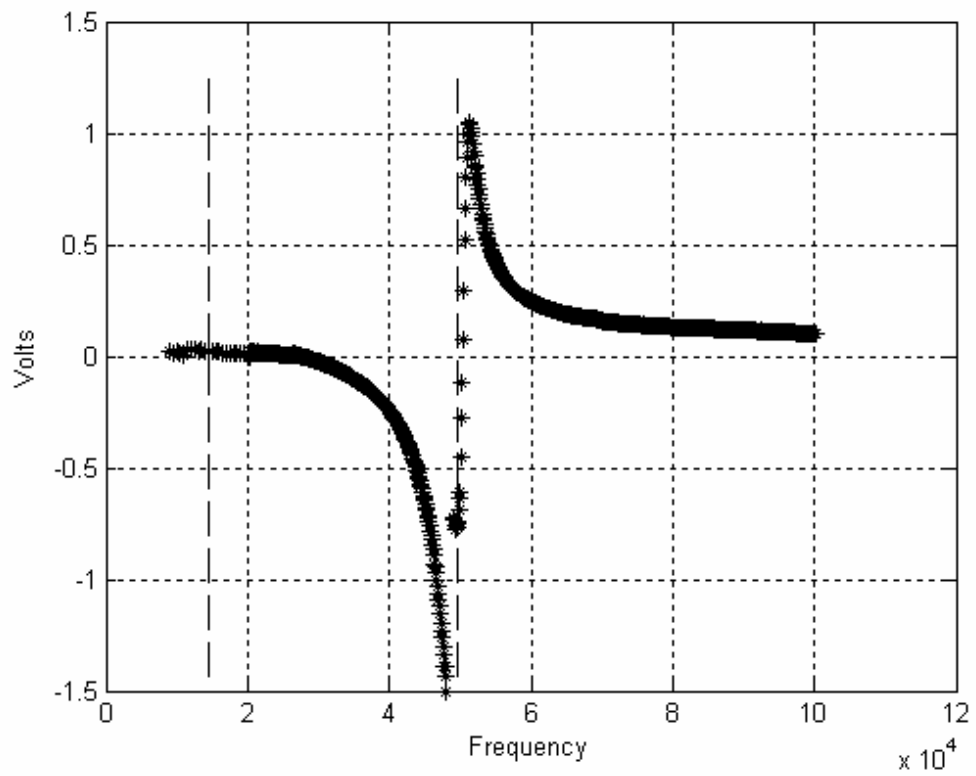


Figure 3.32: The response of the differentially connected receiver coils as a function of the frequency of the applied signal at the transmitter coil. The resonance and the operating frequencies are indicated with dashed lines.

CHAPTER 4

DATA ACQUISITION AND ANALYSIS SOFTWARE

4.1 MATLAB Scanner 1.0

A program to perform scanning experiments with the LIAI is prepared using the user interface facility of MATLAB. This user interface has the same appearance as the LIAI's front panel and all manual settings on the LIAI can be done using this MATLAB program. Program communicates with the LIAI via RS232 port using the set of commands for serial communication given in [74] (Figure 4.1). Data related to the measurements are also collected to the PC via serial port.

On some occasions, due to external effects (sudden change in ambient temperature due to breeze in the room, vibration in the scanner hardware etc.) standard deviation (SDT) of the samples may be higher than the predefined value. With the use of the 'NoiseCheck' radiobutton, program checks the SDT of the received samples. If SDT is higher than acceptable value, measurement at that location is repeated.

Scanning parameters (dimensions of the area to be scanned, number of samples etc.) are provided by the user to the program (upper left corner of the interface). According to this information, program communicates with the LIAI and makes the D/A converters of the LIAI generate the necessary signals for the step motors of the XY Scanner. Thus program handles the tasks necessary for a scanning experiment.

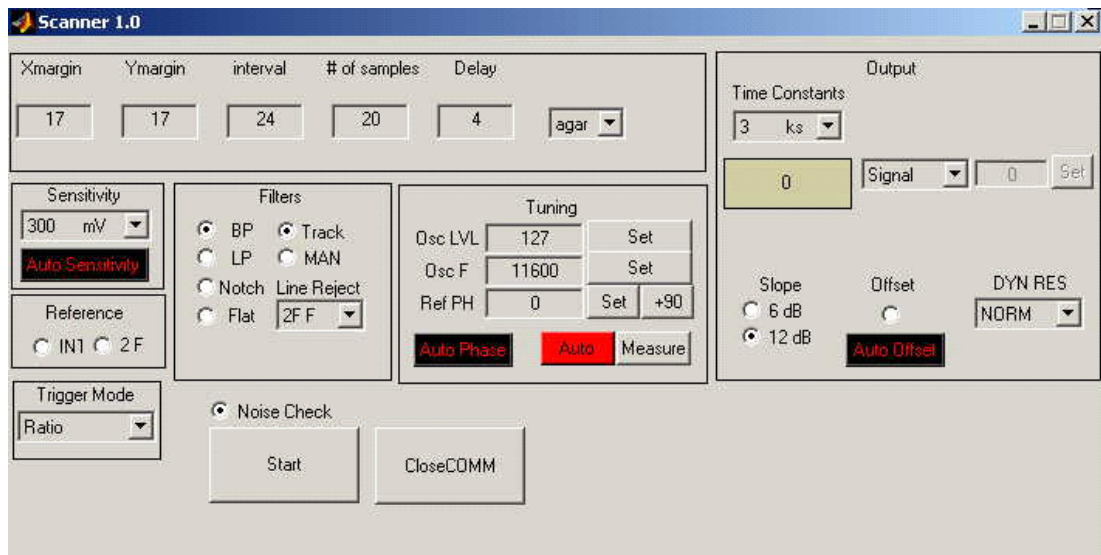


Figure 4.1: MATLAB based user interface program Scanner 1.0.

4.2 HP VEE Scanner 1.0

As an alternative to MATLAB Scanner 1.0, an HP VEE Scanner 1.0 program is prepared to control the LIAI and the XY scanner. Setting information of a scan (i.e., the dimension of the area to be scanned, number of samples to be taken, and delay length) is provided by the user to the program before the scanning starts (Figure 4.2).

The program communicates with the LIAI via the GPIB port. D/A converter outputs at the rear panel of the LIAI, which are controllable with use of the instruction set of the LIAI, generate the signals to control the XY scanner. In the later phases of the study, for the speed considerations XY scanner is controlled by a PIC μ controller which communicates with the HP VEE Scanner 1.0 program via RS232 port while measurement device (the LIAI) is still communicating through the GPIB port, via which the measurement values available at the output of the LIAI are sent to the PC.

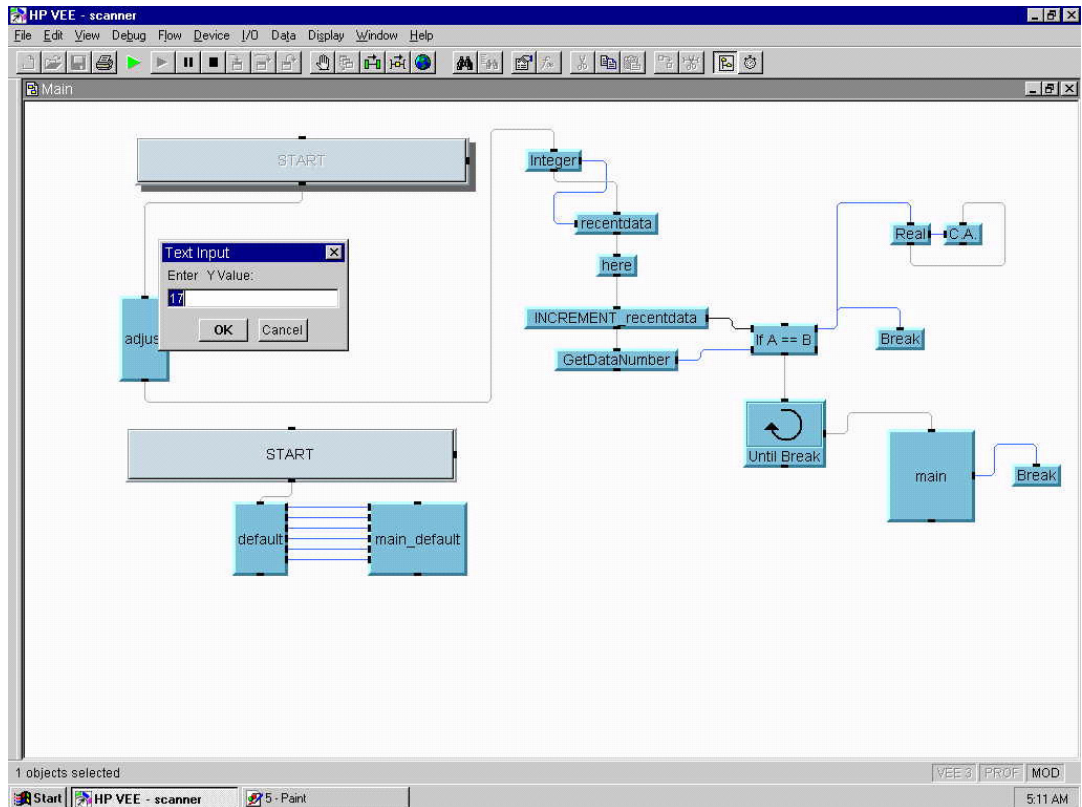


Figure 4.2: HP VEE 4.0 based user interface program HP VEE Scanner 1.0.

With the use of the DAxC, the scanner program is modified to perform scanning experiments using the HP34401A digital multimeter and PIC16F877 μ controller which handles the XY scanner. In this configuration, program communicates with the μ controller via the RS232 port. According the serial data (byte) received from the program, μ controller generates the digital signal which makes the step motors of the XY scanner move the sensor probe to the next measurement point. 7 bits of the received byte is used to express an ASCII character. The most significant bit (bit number 6) is reserved for the selection of one of the motors (i.e, '0' in the most significant bit means that the first motor is going to move and '1' indicates the second motor). Bit number 5 is used to indicate the forward or backward rotation (i.e., if bit number 5 (sixth bit from the right) is '0' selected motor (which is indicated by bit number 6) moves backward, otherwise if bit number 5 is '1', selected motor moves forward. Remaining 5 bits are used to indicate number of

the steps to move the probe from one measurement point to another. Thus, maximum number of steps between two measurement points is 32 steps (which is expressed as xx11111) while minimum number of steps is 1 (which is indicated as xx00001). As an example 1011000 (ASCII equivalent of 'X') means that the first motor (bit number 6 is '1'), is going to move backward (bit number 5 is '0') 24 steps (bit number 4 to 0 are '11000'). When the transportation of the probe is finished, μ controller sends a 'done' signal to the program via the RS232 port and the program waits for a certain time of delay until the mechanical oscillation of the probe is damped. After this delay, program tells the multimeter to start measuring the output voltage of the DA_C by taking defined number of samples which are sent to PC via GPIB port. When all samples at a measurement point are received by the computer, software communicates with the microcontroller to make the XY scanner move the probe and this cycle is repeated until the area defined by the user at the beginning of the experiment is scanned completely.

4.3 Data Observer 1.0

A user interface program is prepared using MATLAB to analyze the field profiles (voltage measurements) obtained by scanning experiments. Field profiles for agar objects can be obtained in three steps:

Field profile for background is obtained by scanning the probe over a defined area when there is neither the saline solution nor the agar object in the vicinity of the probe. Scanning is repeated when an agar object is placed in the saline solution. Taking the difference of these two field profiles in the software, thus eliminating the signals coming from the background, the field profile of the agar object in the saline solution is obtained.

Using this program one can observe the image of the background (i.e., no agar & saline solution is existing), the image of the background with agar phantom (i.e., agar phantom + saline solution + background forming a conductivity image profile) and the image of the former data being subtracted from latter to give the image profile due to agar phantom + water solution (Figure 4.3). Each of three

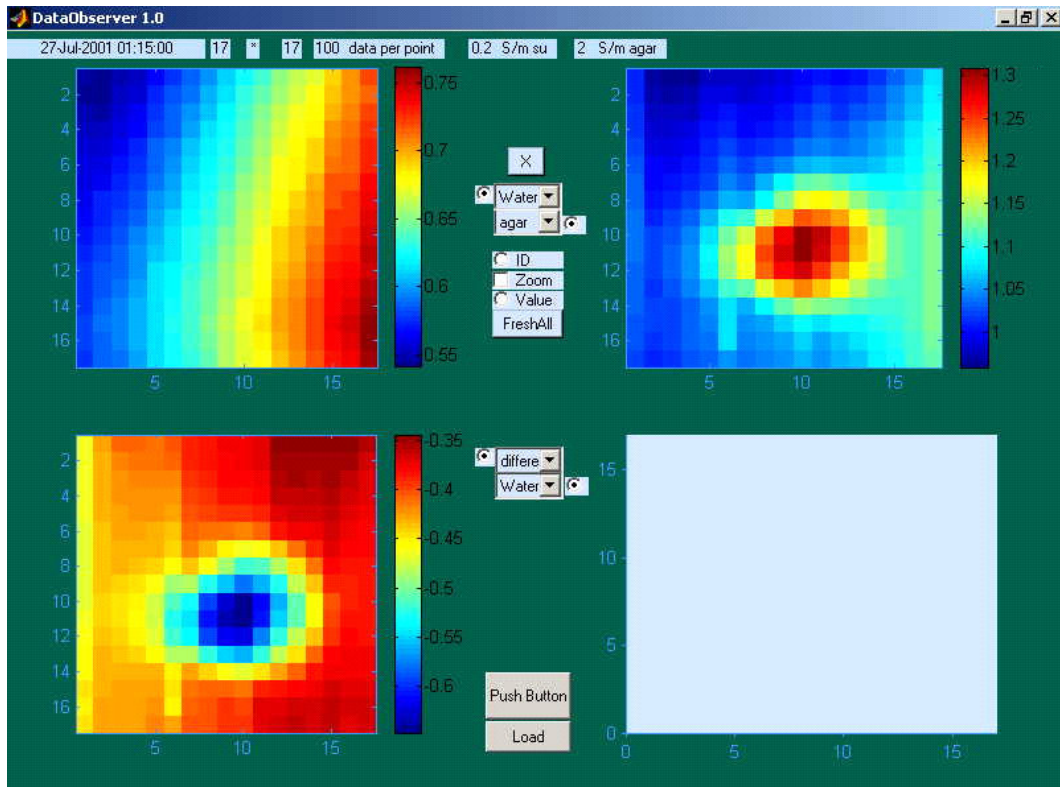


Figure 4.3: MATLAB based user interface program DataObserver 1.0. In the upper left window is the background field profile of a scan, upper right is the background + agar phantom field profile, lower left is the former image subtracted from the latter.

images can be observed at the same time in one of the four available windows in the interface program. Besides, the 1-D plots showing all samples taken at each measurement locations and averaged samples are available to the user. User may also see the variance image, formed from the variances calculated for each measurement point. Variance value of a specific pixel becomes visible when user hits the corresponding pixel with mouse on the image while all samples corresponding to that pixel is observed in another window (Figure 4.4). Some other facilities available in the interface are as follows:

- Pixel value in a 2-D image becomes visible moving the cursor above that pixel.
- 1-D plots can be zoomed using the ‘zoom’ facility.

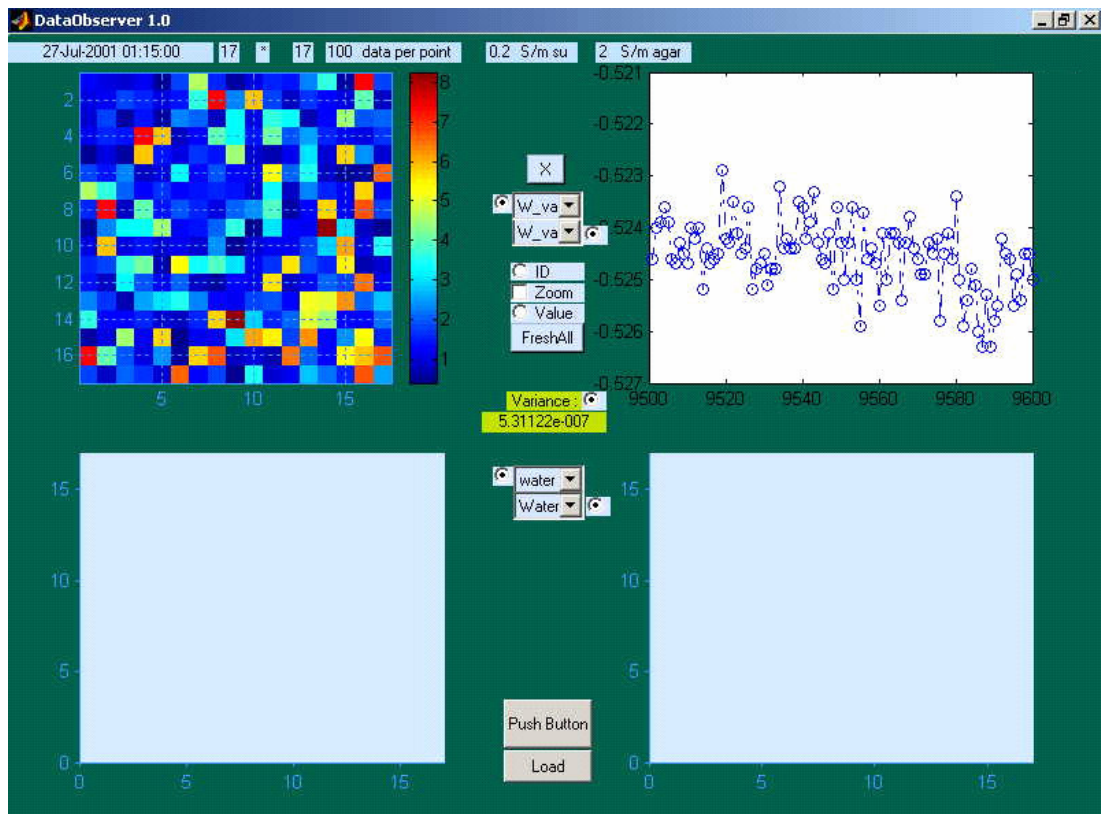


Figure 4.4: MATLAB based user interface program DataObserver 1.0. Upper left is the variance image of the 2-D field profile, upper right is 100 many samples obtained at a single measurement point chosen by hitting (with mouse) the related measurement point's pixel in the 2-D variance image. Variance value is written below the 'Variance' radiobutton which is showed by the light green colour in the middle of the interface window.

- Information kept in a notepad file like the experiment date and the conductivity values of the agar and the saline solution can be viewed at the top.
- Image or the plot to be shown in one of the four windows can be chosen independently from the popup lists.

Codes of these programs together with the Assemble codes prepared for the winding machine and XY Scanner are available in a CD which includes all the data related to the thesis.

CHAPTER 5

RESULTS

5.1 Introduction

The performance tests are carried out with the measurement systems that employ the LIAI and the DAcC. Phase sensitive detection system employing the LIAI and nulling circuit is tested with signals having different amplitude and varying phase. Phase sensitive measurement capability and noise characteristics of the DAcC are investigated next. Magnetic field detection tests reveal the response of the DAcC to the external magnetic fields. Field profiles of the scanning experiments pursued with both systems are also provided.

5.2 The Lock In Amplifier Instrument and the Nulling Circuit

Nulling circuit together with the LIAI is tested with the test setup whose schematic is given in Figure 5.1. In this experiment oscillator output of the LIAI generates a signal whose frequency is 14.1 kHz. This signal is amplified by the power amplifier which is driving the transmitter coil. Transmitter coil current flowing through monitor resistor (R_M) generates the reference voltage for the rest of the circuit and the LIAI. In the nulling circuit, reference voltage is amplified and 90° phase angle is introduced by the phase shifter block to get rid of the quadrature component of the signal coming to '+' input of the differential amplifier. Reference channel of the LIAI is fed with an in-phase signal or equivalently with a 0° -phase signal. In the amplifier (A_V) and the unity gain phase shifter blocks (θ_V) which are

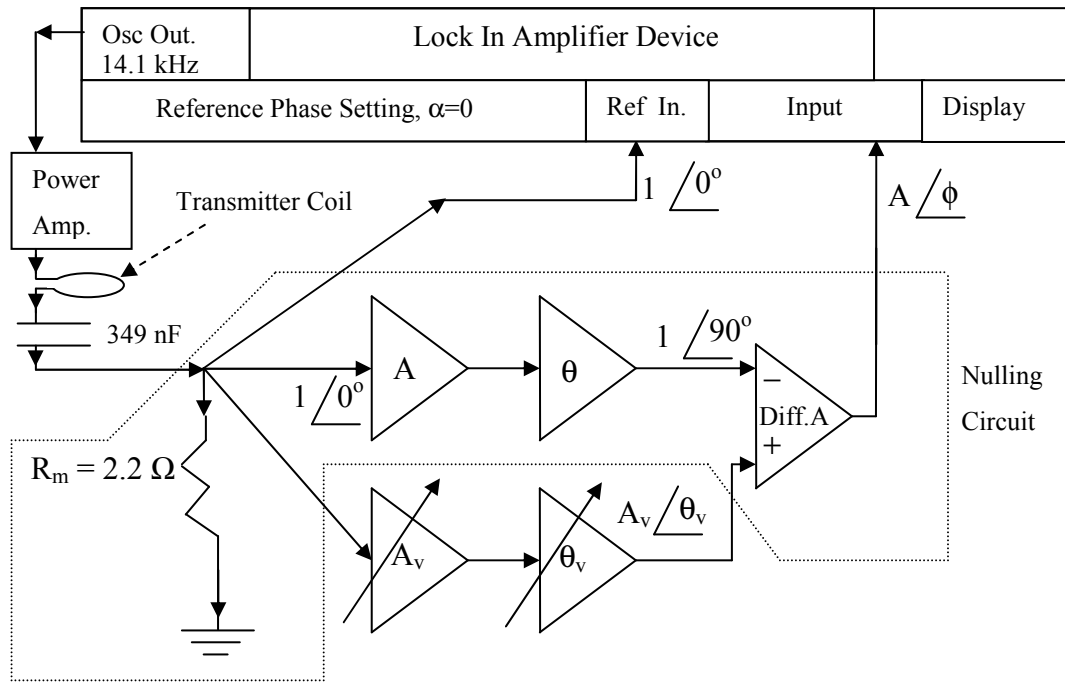


Figure 5.1: Test setup for phase sensitive measurement system using the LIAI and the nulling circuit.

similar to those used in the nulling circuit, amplitude and phase of the input signal, A and ϕ respectively, are changed.

5.2.1 Phase and amplitude measurement test

In the test setup shown in Figure 5.1, the input voltage (A) is changed from 500 mV to 4000 mV with steps of 500 mV while the phase angle (ϕ) varies from -33° to -529° which is more than enough to cover the whole period of 360° . Obtained output voltages (A') are drawn in Figure 5.2 and Figure 5.3.

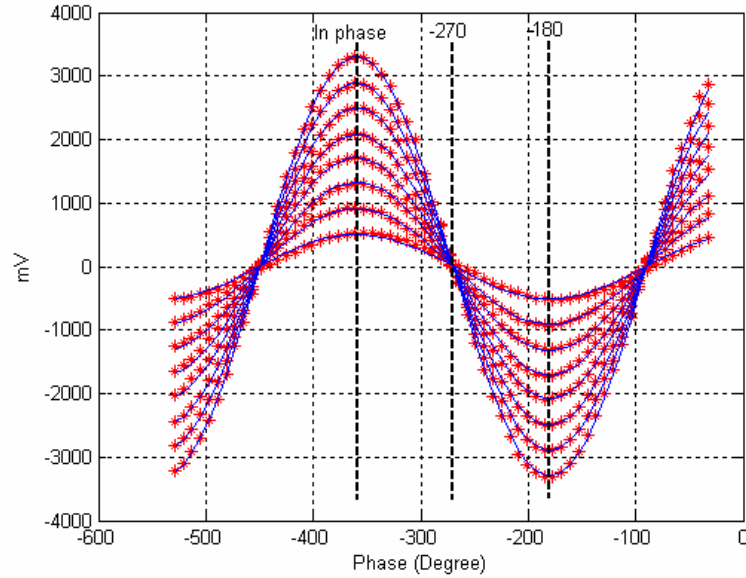


Figure 5.2: Output voltage of the LIAI (A') as a function of the input phase angle (ϕ) for different values of input amplitude A . *: measured values, lines: fitted plots whose expressions are in the form of $A_{PEAK} \cdot \cos(\phi \cdot \pi/180)$. Graph of A_{PEAK} values is drawn in Figure 5.3.

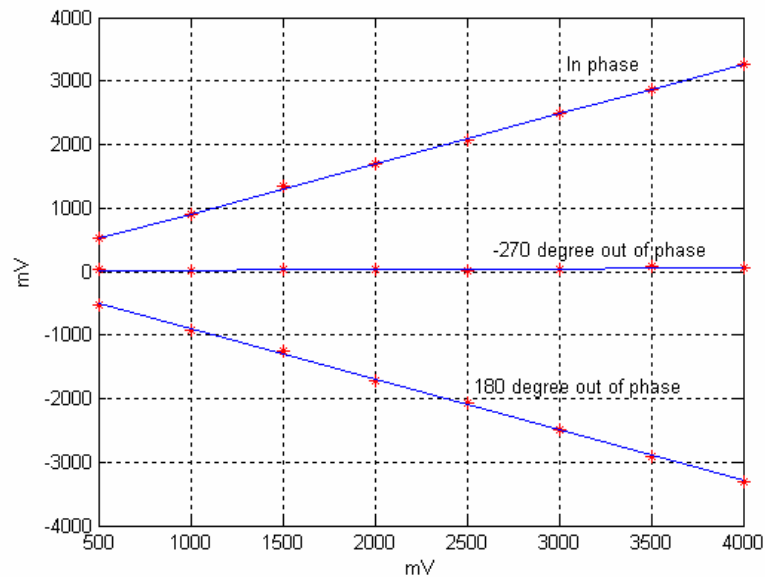


Figure 5.3: Peak value of the output amplitude (A'_{PEAK}) as a function of input amplitude (A_{PEAK}), for phase angle $\phi = -360$ (in phase), $\phi = -270$ and $\phi = -180$. *: measured values, lines: fitted plots whose slopes are 0.7848, 0.0149, -0.7974 for $\phi = -360$, $\phi = -270$, $\phi = -180$ respectively. The lines are obtained using the points that the cosine waveforms and the dashed lines (in Figure 5.2) intersect.

5.3 The Data Acquisition Card (DAcC) Performance Tests

The test related to the scaling performance, noise levels of the individual blocks and phase and amplitude characteristics are carried out with the DAcC. Conductive ring tests with the amplifier and the integrator circuits are performed.

5.3.1 Scaling

Performance test of the scaling block, which consists of the Rms to DC converter circuit and the divider circuit (indicated as RMS and D1 respectively in Figure 3.3) is made. Transmitter coil current is increased from 25 mA to 200 mA by changing the input amplitude of the power amplifier and the receiver coil buffer output is divided by the rms value of the output of the transmitter coil buffer. Obtained graph for the output of the divider D1 is drawn in Figure 5.4. As transmitter coil current increases, receiver coil voltage and rms value of the transmitter coil also increase. Dividing receiver coil voltage by the rms value of the transmitter coil current, a constant voltage at the output of the divider circuit is obtained which eliminates the effect of the transmitter coil current amplitude fluctuations on the receiver coil voltage. This is the case for moderate values of the current as shown in Figure 5.4. For current values higher than 100 mA scaling can be said to be achieved. As a remainder, in this study unless otherwise stated, transmitter coil current is set to be 200 mA, which puts the scaling circuit in the well defined operating current value.

5.3.2 Noise levels of the DAcC blocks

Noise level of the components of the DAcC is investigated. Test signals are generated by Agilent 33120A function generator. Measurements are done by Agilent 34401A digital multimeter. Both devices are GPIB controllable. Test signal frequency is set to 14.1 kHz. After isolating the input and output pins of the multiplier IC in Figure 3.16 from the rest of the circuit by just disconnecting the pin connectors, MULT_IN_1 and MULT_IN_3 are given the same signal which is 1

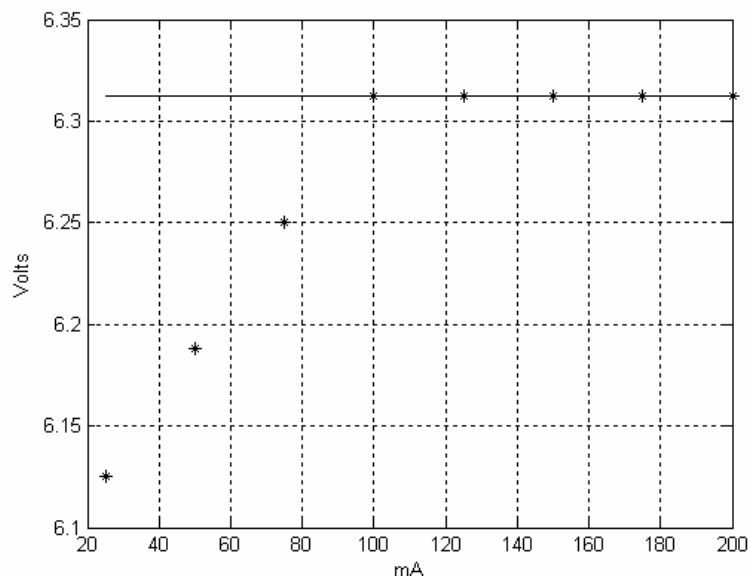


Figure 5.4: Divider circuit (D1) output voltage as a function of transmitter coil current. *: measured values, line: fitted data for the well defined operating current values between 100 and 200 mA.

V_{RMS} at 14.1 kHz. 237 samples are taken from the output of the multiplier by the multimeter in 120 seconds. Normalized rms value of the output of the function generator is found to be $1 \pm 3.68 \cdot 10^{-6}$. After this signal is squared in the multiplier normalized rms value of the output of the multiplier becomes $1 \pm 7.55 \cdot 10^{-5}$.

To test the individual noise level in the low pass filter, isolating the filter from the rest of the circuit by disconnecting its input and output pins, a signal of 2 mV_{DC} added to 343.5 mV_{RMS} at 14.1 kHz is applied to F_1 in Figure 3.17. Measured value of the filter output is 1.5 mV_{RMS}.

In the next step performance of the DC amplifier stage in Figure 3.22 is examined. Function generator is adjusted to produce 10 mV DC whose normalized standard deviation is 0.004 after 237 sample measurements. This signal is amplified by 10 and after that by 100, by the amplifier stages cascaded to produce an amplification factor of 1000. Normalized standard deviation at the output is 0.0018.

Considering the obtained figures, it is concluded that individually components do not generate much extra noise other than the noise level present at their input stages.

As a last step overall performance is observed using the scaling circuit (Rms to DC converter + divider circuits), multiplier, low pass filter and amplifier together. The test signal at 14.1 kHz with 1 V_{RMS} is given to the Rms to DC converter block which is shown as RMS in Figure 3.3, output of which feeds the ‘-’ input of divider blocks D1 and D2 (Figure 3.3) with the rms value of the test signal. ‘+’ inputs of D1 and D2 are given the test signal itself. At the outputs of D1 and D2, test signal scaled with its own rms value is obtained. These scaled signals at the outputs of D1 and D2 are multiplied in the multiplier block (M) and output of the multiplier is low pass filtered in LP (Figure 3.3), which produces a dc signal to be amplified in the amplifier block DC. For different amplitudes of the test signal, standard deviation of the output of DC is drawn in Figure 5.5. Overall normalized standard deviation is observed to be in the order of 10^{-4} for input values higher than 500 mV. Input values higher than 500 mV corresponds to the transmitter current values higher than 100 mA. Increase in the standard deviation for input values less than 500 mV arises from the characteristics of the scaling block that is observed in Figure 5.4. Mean value of the output of the amplifier is plotted in Figure 5.6.

5.3.3 Phase and Amplitude Tests for the DAcC

To investigate the response of the DAcC to inputs whose phase differs from the reference phase, test setup in Figure 5.7 is used. Total gain of the amplifier blocks A2 and A3 at the output of the DAcC is adjusted to produce 1 V as maximum output. Function generator feeds the power amplifier which drives the transmitter coil.

Transmitter coil current flows through the 349 nF capacitor and the monitor resistor R_M . Voltage on the monitor resistor is taken as reference and is given to the reference input of the DAcC. Input channel of the DAcC is fed with the output of the phase shifter block. Phase of the input is varied from $+300^\circ$ to -150° . A cosine shaped output waveform is obtained as expected. This waveform implies that the DAcC can measure the component of the signal coming to the input channel in phase with the signal at the reference channel (Figure 5.8). The mean error between the fitted plot

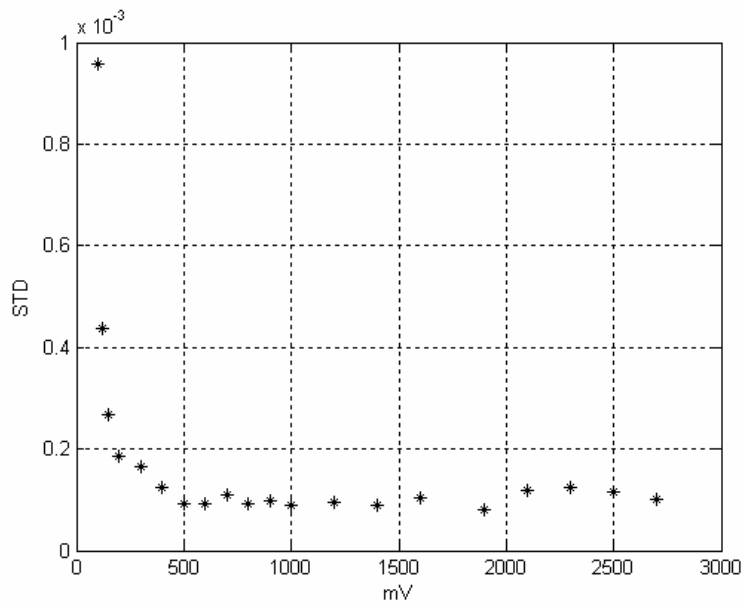


Figure 5.5: Standard deviation at the output of amplifier block, (indicated as DC Figure 3.3) as a function of the test signal amplitude.

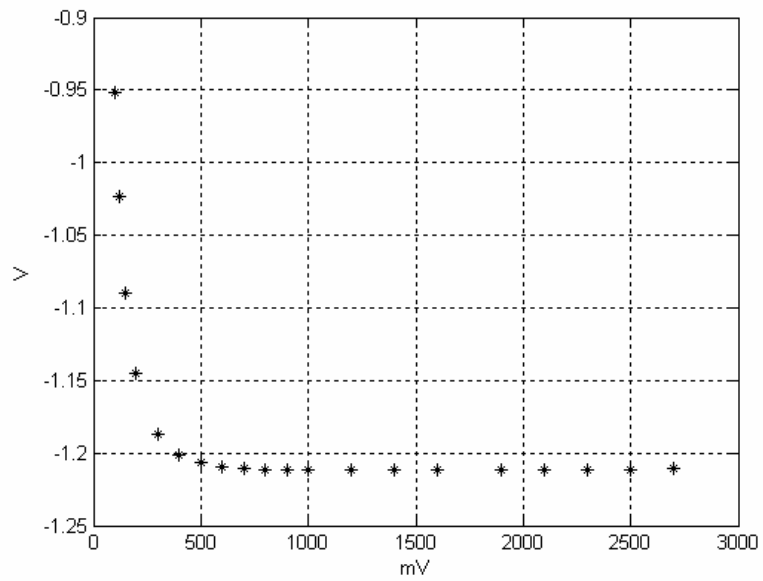


Figure 5.6: Mean value of the amplitude of the output of the amplifier as a function of the test signal amplitude.

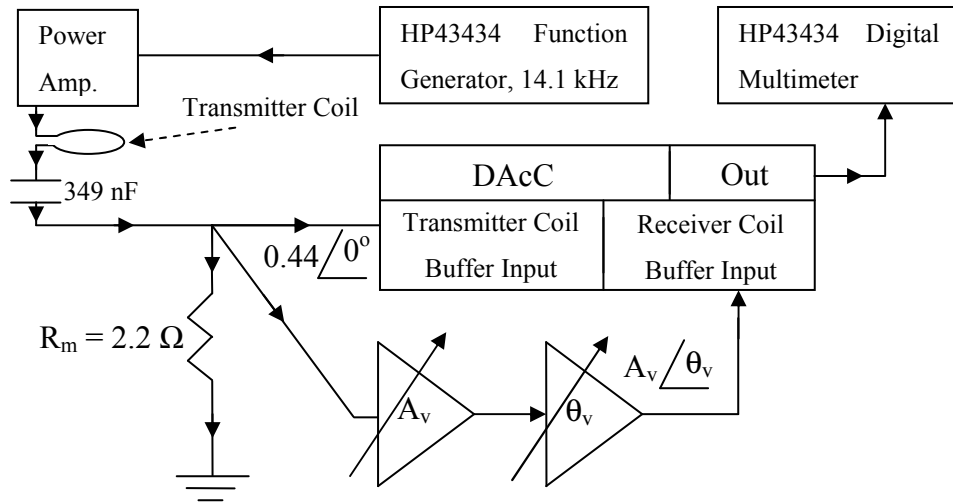


Figure 5.7: The DAcC test setup.

and the measurements are found to be 0.6% of the full scale.

To find out the response of the DAcC to input signals with different amplitudes the experiment setup whose details are drawn in Figure 5.9 is suggested. An external magnetic field is created by a secondary transmitter coil with 200 turns, which is called as transmitter coil 2, TrCoil₂. Function generator output is given to a variable gain circuit. Gain of this circuit is adjusted by a microcontroller and a D/A converter, DAC0832 (Figures 5.10 and 5.11). According to the 8 bit digital value at the D port of the microcontroller, internal resistors of D/A Converter is enabled to produce an amplification factor of $\langle 8 \text{ Bit} \rangle_{10} / 256$ at the output of the variable gain circuit. $\langle 8 \text{ Bit} \rangle_{10}$ means the decimal value of the digital data expressed by 8 bits. Output of this circuit feeds a second power amplifier which drives TrCoil₂. Thus current flowing through TrCoil₂ can take 256 discrete values between 0 mA and 10 mA.

L , the distance between TrCoil₂ and sensor (Figure 5.9), is adjusted to be 4, 6, 8 and 10 cm and the in phase component of the signal induced in the receiver coil is measured. For these distances the magnetic field intensity created by TrCoil₂ at distance L is analytically calculated to be -131, -35, -14 and -7 μT , for different values of L which are 4, 6, 8, and 10 cm, respectively. Plots of the measured in phase

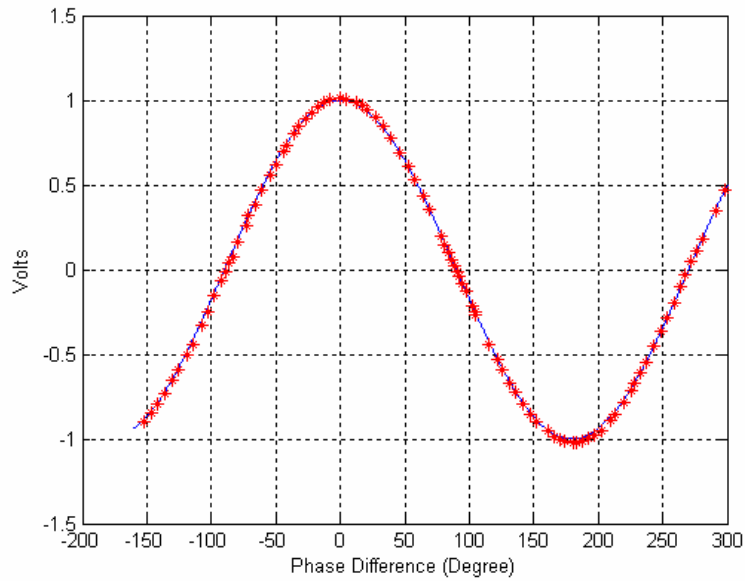


Figure 5.8: Output voltage for the DAC as a function of phase difference. *: obtained values, curve: fitted plot which can be expressed as $1 \cdot \cos(\text{PhaseDifference})$.

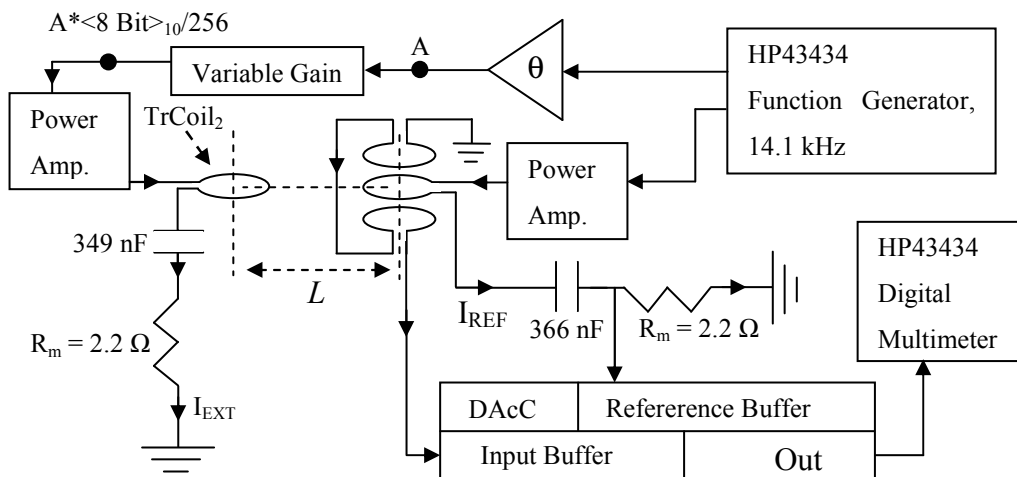


Figure 5.9: Test setup which is used to investigate the response of the measurement system to external magnetic field.

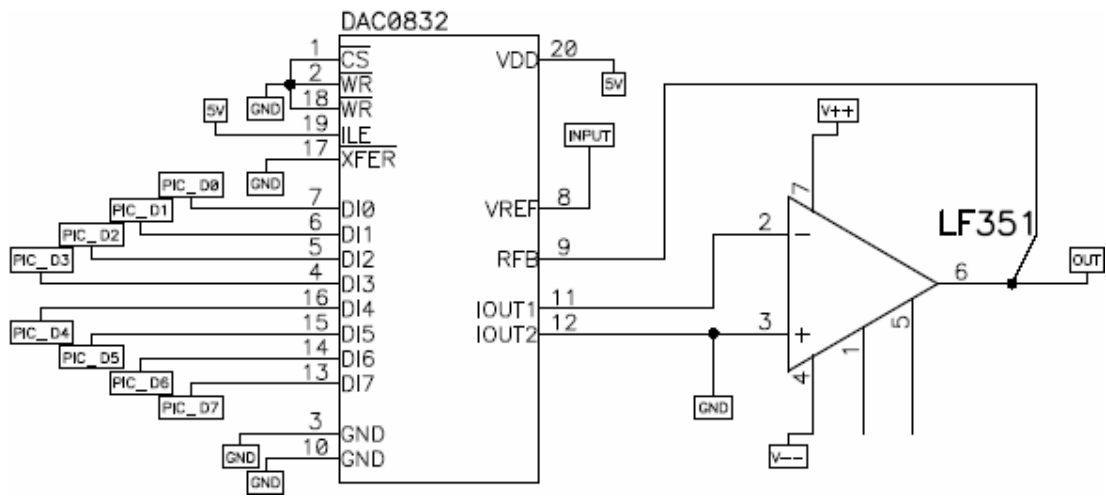


Figure 5.10: Digitally controlled variable gain circuit. Digital data comes from the microcontroller circuit drawn in Figure 3.24. Output signal is $V_{REF} \cdot \langle 8 \text{ Bit} \rangle_{10} / 256$.

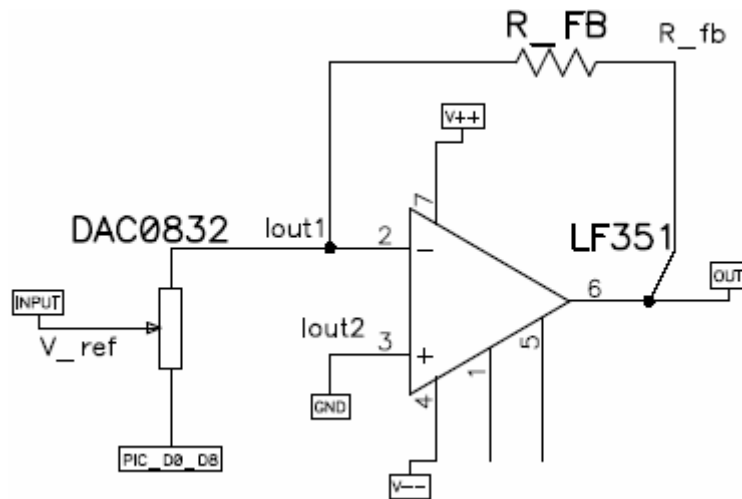


Figure 5.11: Digitally controlled variable gain circuit modeled as an inverting amplifier. Value of the potentiometer at the input stage is adjusted by microcontroller.

component for varying external magnetic field and varying distance are drawn in Figure 5.12.

As a last experiment in this subsection, phase of the current flowing through TrCoil_2 which is called as I_{EXT} is adjusted to be 90° leading the current in the transmitter coil of the sensor, I_{REF} . A phase shifter block placed between the function generator output and the input of the variable gain circuit can be used for this purpose. In this case voltage induced due to external magnetic field will be in phase with I_{REF} , since voltage induced in the receiver coils due to external magnetic field created by I_{EXT} lags I_{EXT} by 90° . Changing the gain of the amplifier circuit a linear graph which is shown as 'A' in Figure 5.13.

If I_{EXT} is adjusted to be 180° leading I_{REF} , induced voltage in the receiver coils due to I_{EXT} will be 90° leading I_{REF} . In this case as the external magnetic field increases, 0 V is measured as the in-phase component. This situation is indicated as 'B' in Figure 5.13.

Lastly, If I_{EXT} is adjusted to be 270° leading I_{REF} , induced voltage in the receiver coils due to I_{EXT} will be 180° leading I_{REF} . In this case as the external magnetic field increases a linearly decreasing voltage is measured as the in-phase component. This situation is indicated as 'C' in Figure 5.13.

5.3.4 Magnetic Field Measurement Tests Using Conductive Ring and Resistors

In the magnetic field detection experiments, explained in section 5.3.3, the magnetic field to be detected is generated by a second transmitter coil (TrCoil_2 in Figure 5.9) which is fed by a second power amplifier. Another experiment is conducted using a 3-turn coil (conductive ring) with 30 mm diameter prepared with 0.5 mm copper wire. This coil is placed right below the magnetic field sensor and output port of the coil is shunted with resistor R as shown in Figure 5.14. Value of R is varied in the range of 1Ω to $10\text{k}\Omega$.

In the experiment setup which is drawn in Figure 5.14, the power amplifier which drives the transmitter coil in the magnetic sensor is fed with a 14.1 kHz signal generated by the Agilent 33120A function generator. The current flowing through

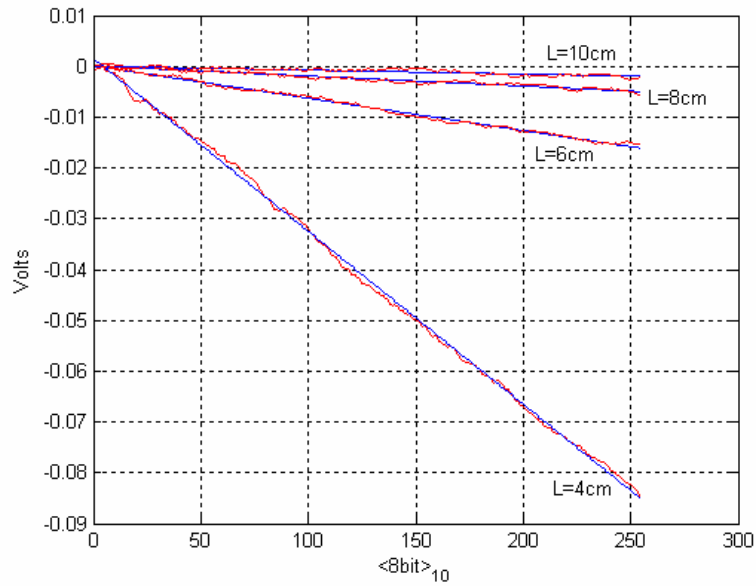


Figure 5.12: Measured in-phase component voltage for different values of L as a function of decimal value of the 8 bits at Port D of microcontroller. As decimal value is increasing output of the variable gain amplifier and flowing in the TrCoil_2 increases. As L increases maximum magnetic field created by the second transmitter coil (when $\langle 8\text{bit} \rangle_{10} = 255$) decreases (magnitude of the slope of the fitted lines decreases) which decreases the induced in phase component in the receiver coils.

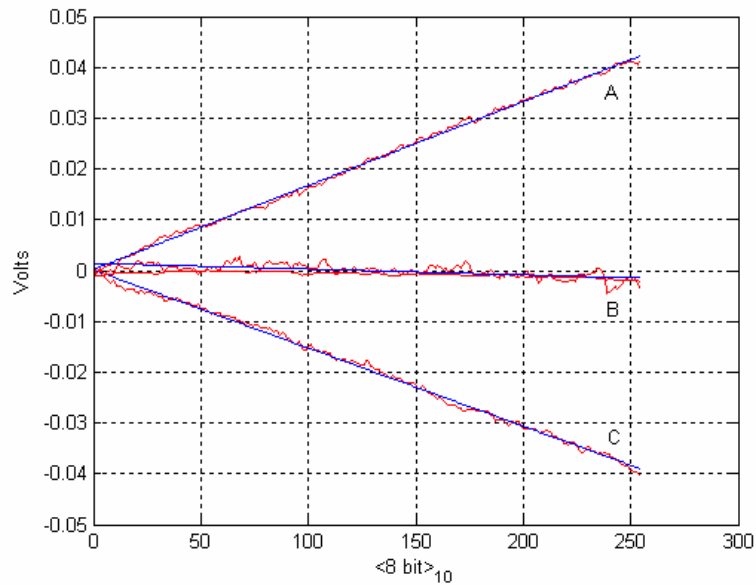


Figure 5.13: Measured signal due to I_{EXT} as a function of decimal value of the Port D of microcontroller. r: measured values, b: fitted line for the measured data.

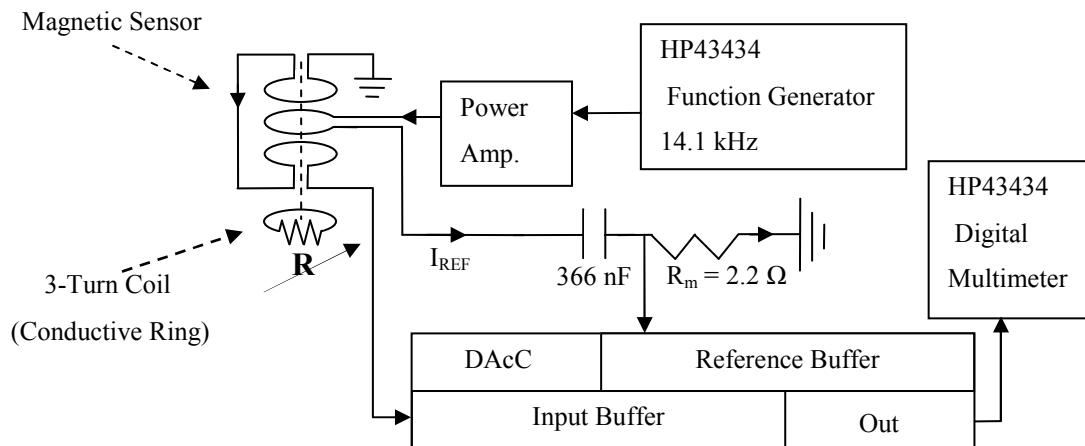


Figure 5.14: Magnetic field generation by the conductive ring with variable resistance R .

the transmitter coil is monitored on the monitor resistor R_M whose voltage provides the reference signal to the DAC. Differentially connected receiver coils' output signal is buffered in the receiver coil buffer of the DAC. The primary flux generated by the transmitter coil of the magnetic sensor results in eddy currents flowing in the 3-turn coil. The amplitude of the current flowing in the conductive ring thus the magnetic field generated by the ring (secondary field) is controlled by the resistor R . The secondary magnetic field which is inversely proportional to the resistor R is detected by the receiver coils, alias the magnetic sensor. Inverse proportion is deduced from the following reasoning: Primary flux generated by the magnetic sensor and the portion of this flux coupled to the conductive ring does not change when the transmitter coil current's amplitude and frequency is kept constant. This coupled flux in the conductive ring induces a constant amplitude sinusoidal voltage across output port of the ring. Though, no current flows through the ring until the port is shorted or shunted to a resistor. If a resistor is connected to the port, the only parameter that will determine the current flowing through the resistor will be the resistor itself. If the resistor value is decreased, the current flowing in the ring will be increased and if the resistor value is increased the current will be decreased while the induced voltage in the ring is still constant. Since the flux induced by the current

flowing in the ring (secondary flux) is directly proportional with the conductive ring current, it is inversely proportional to the resistance of the conductive path, which is represented by R .

Using the setup in Figure 5.14, secondary voltage induced in the receiver coils due to secondary flux generated by the conductive ring is measured. The DAaC is adjusted to measure the signal in phase with the current flowing through the transmitter coil in the magnetic sensor. At the last stage of the DAaC in Figure 3.3, the two available blocks are the amplifier block and the integrator circuit block. Conductive ring experiments are conducted with use of these blocks.

5.3.4.1 Conductive Ring and Resistor Experiment using the DC Amplifier

DC signal at the output of the lowpass filter in the DAaC carry the phase and amplitude information about the in-phase component of the signal coming from the receiver coils (section 3.3). Lowpass Filter's DC output is amplified by the inverting amplifier, the block indicated as DC in Figure 3.3. Output bandwidth of the amplifier is limited using a 680 nF capacitor connected to the output of the opamp. Thus high frequency terms at the output is eliminated.

Measurements are carried out with 42 resistors covering the resistance range from 1 Ω to 10 k Ω . For each resistor 20 samples are taken. Another 20 samples are taken after disconnecting the resistor from the conductive ring, making the ring open circuit (no secondary field is generated by the ring). Aim of the second measurement is to observe and cancel out the effect of voltage drift occurring in the receiver coils. A slight drift of 0.5 mV/minute can be observed in Figure 5.15. When no resistor is connected to the ring, all the measurements taken should yield 0 mV at the output of the system. But in Figure 5.15, for the measurements when the resistor is not connected, it is seen that there is approximately 10 mV drift between the measurements taken at the beginning (sample number 0 in Figure 5.15) and at the end (sample number 1680 in Figure 5.15) of the experiment. Drift is assumed to be originated thermally in the 10000-turn receiver coils.

A data set for a single resistor consists of 40 samples, 20 of which is taken

when the resistor is connected and remaining 20 of which is taken right after the first measurement when the resistor is not connected. These two data sets are taken such that the time delay between them is as little as possible. Taking the difference of the former measurements from the latter the Difference Data is obtained. In the Difference Data, effect of drift is eliminated and response of the system to external secondary magnetic field is observed. For 42 different resistors values $42 \times 20 \times 2 = 1680$ many samples are taken throughout all experiment (range of x- axis in Figure 5.15).

If the effect of drift is minimized and the coil signal is stable, since amplified DC signal is sampled at the output of amplifier (block named DC in Figure 3.3), at each measurement data taken should give a line with zero slope. This is actually the case in Figure 5.16 in which the Difference Data for 42 resistors are plotted. It is seen that the Difference Data at 20 points in Figure 5.16 conform to the zero-slope lines.

Mean value of the Difference Data is plotted in Figure 5.17 and 5.18. Since the induced (secondary) voltage is directly proportional to the secondary flux which is inversely proportional to the resistor value shunted to the conductive ring, $y=k/x$ curve fits to the data, where k is a constant. Plotting the same plot for $1/\text{Resistor Value}$ vs. Mean of the Difference Data, a linear plot is obtained as given in Figure 5.19. Maximum measurable resistor value employing the amplifier is limited by the Signal to Noise Ratio (SNR) of the system, as observed in Figure 5.20. Arrows in Figure 5.20 (a) and (b) indicate the points left side of which is zoomed in the following figure. In Figure 5.20 (c), the arrow indicates the minimum distinguishable value (which corresponds to maximum distinguishable resistor value) whose x value is $2.52 \times 10^{-3} \text{ 1}/\Omega$. Inverting this, corresponding resistor value can be found to be $1/(2.52 \times 10^{-3} \text{ 1}/\Omega) = 397 \Omega$. For this resistor mean of the measured value is $1.09 \times 10^{-3} \text{ V}$ and corresponding value using the fitted line in Figure 5.20 (c) is $7.12 \times 10^{-4} \text{ V}$. For the points remaining in the left to this value which corresponds to large values of resistors, SNR of the system is not enough to distinguish the larger resistor values.

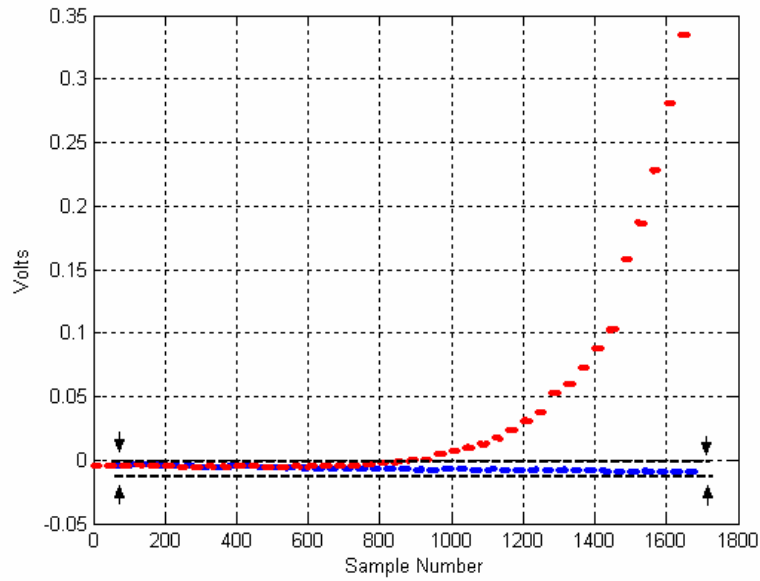


Figure 5.15: The output voltage of the amplifier as a function of the samples taken during whole experiment. Packages of red points refer to the 20 samples taken with different values of resistors. Packages of blue points around 0V refer to the corresponding offset measurements. An approximate drift about 10 mV is observed between the dashed lines indicated by arrows.

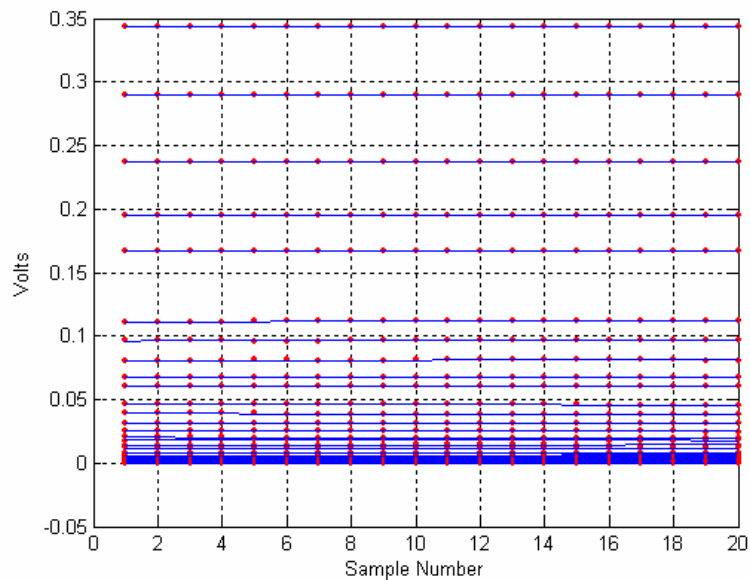


Figure 5.16: Output of the amplifier as a function of the Difference Data for all measurements. Lines with zero slope whose values are varying between 0 V and 0.35V refer to the measurements with different resistor values.

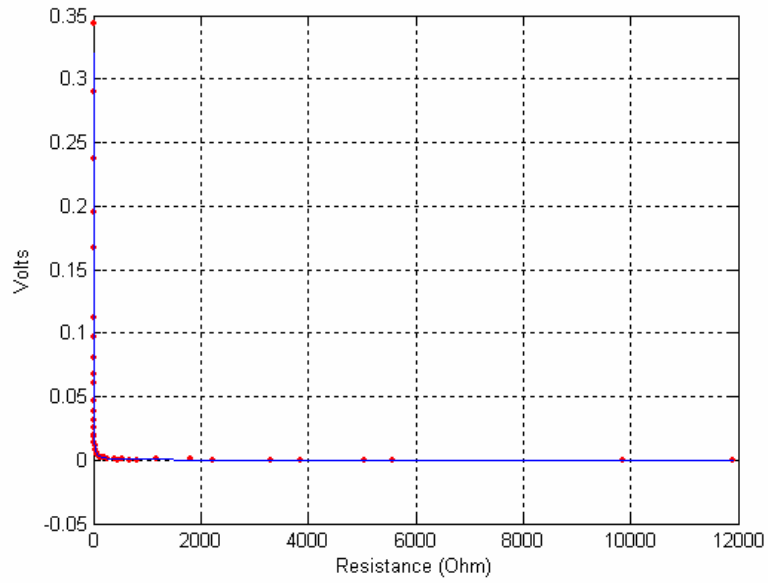


Figure 5.17: Output voltage of the DAC employing the amplifier as the last stage as shown in Figure 3.3 as a function of Resistor values. Red points are the mean of the Difference Data. Blue colored plot is the fitted curve.

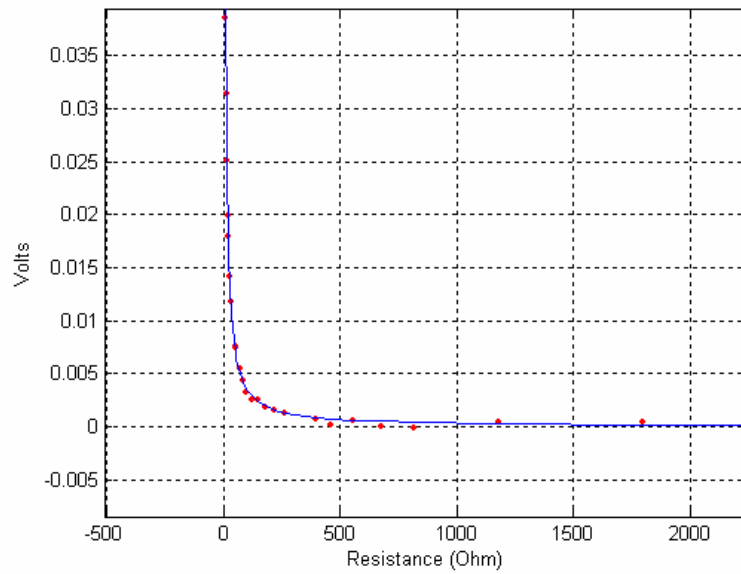


Figure 5.18: Zoomed version of the output voltage in figure 5.17 as a function of resistor values.

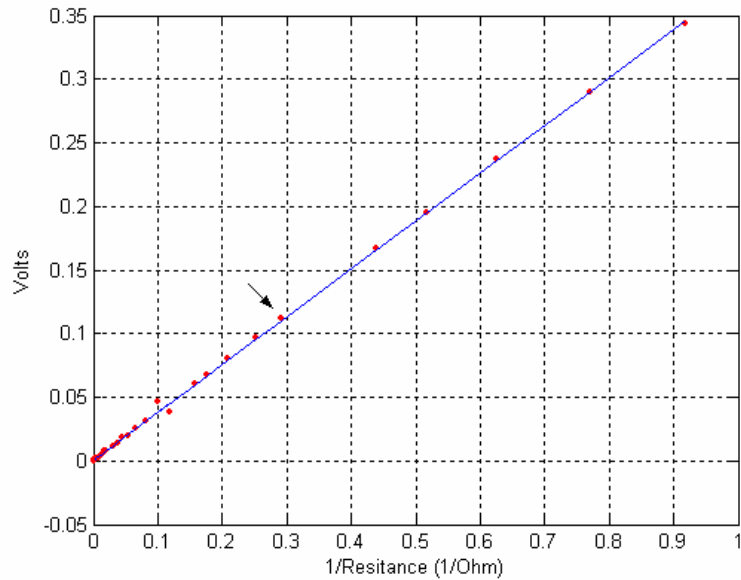
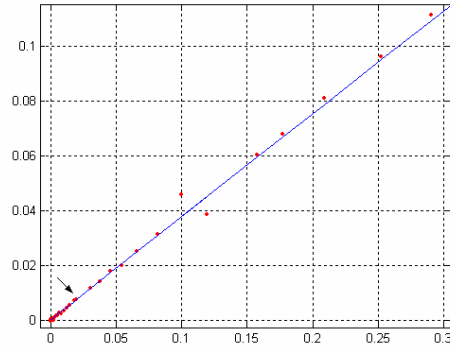
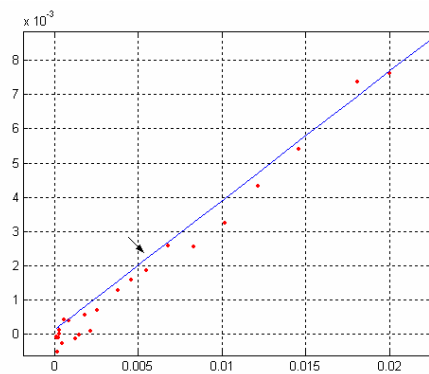


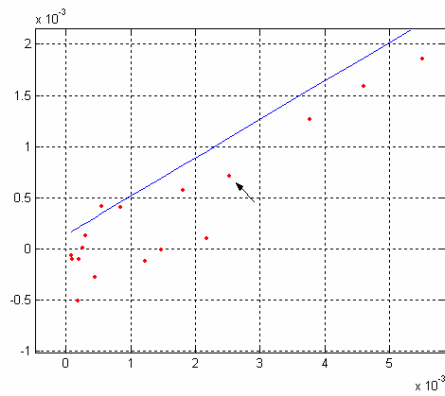
Figure 5.19: Difference Data obtained from the output voltage of the DAC employing the amplifier as the last stage as shown in Figure 3.3 as a function of $1/(\text{Resistor Value})$. Red points are the mean values of the Difference Data. Fitted curve plotted in blue has the expression of $y = 0,38x$. Left hand side of the point indicated by the arrow around $x=0.3$ is zoomed in the next figure which is Figure 5.20 (a).



(a)



(b)



(c)

Figure 5.20: Output voltage of the amplifier as a function of (Zoomed) 1/Resistor Values of the same plot in Figure 5.19.

5.3.4.2 Conductive Ring and Resistor Experiment using Integrator

Conductive ring and resistor experiment explained in section 5.3.4.1 is repeated with an integrator circuit (INT) used as the last stage of the DAAC (Fig.3.3). Explanation related to the working principle of the integrator circuit is given in the last two paragraphs related to Figure 3.23 and Figure 3.24 in section 3.3. To remind shortly, DC output of the low pass filter is connected to the integrator circuit (INT in Figure 3.3). The 680 nF capacitor of the integrator is short circuit via a multiplexer IC. Thus integrator gives 0 mV when the capacitor is short circuit (multiplexer is enabled). When resistor R (in Figure 5.14) is shunted to the conductive ring (multiplexer is disabled), a DC jump inversely proportional to R is observed in the input of the integrator. This DC value determines the slope of the rising voltage at the output of the integrator. Rising of the integrator voltage is limited with 17 V beyond which opamp saturates.

In Figure 5.21, data drawn in blue color are taken when no secondary field exists (resistor R in Figure 5.14 is not connected). When no secondary field exists lines with zero slope starting from 0 mV are expected to fit to the taken data but due to input offset of the opamp used in the integrator, lines with similar slope values are obtained. Other lines in the same graph which exhibit a large absolute rising characteristics (from 0V to |-17 V|) fit to the data with red colour which was obtained when different values of resistor R are connected to the conductive ring of Figure 5.14.

In Figure 5.22, difference data obtained by subtracting the data obtained when no external field exists from the data when a resistor is connected are plotted. For 42 different values of resistor, $42 \times 2 \times 18 = 1512$ samples are taken. 42 difference data having 18 samples each are fitted by corresponding lines (Figure 5.22).

Slopes of the lines that fit to the difference data are drawn for the corresponding resistor values in Figure 5.23 and 5.24. Fitted curve can be expressed as $y = -m/x$, where m is a constant. This kind of relation was expected due to fact that the slope of the voltage measured at the output of the integrator during a measurement performed when resistor R is shunted to the conductive ring is proportional to the DC value at the input, whereas DC value is inversely proportional

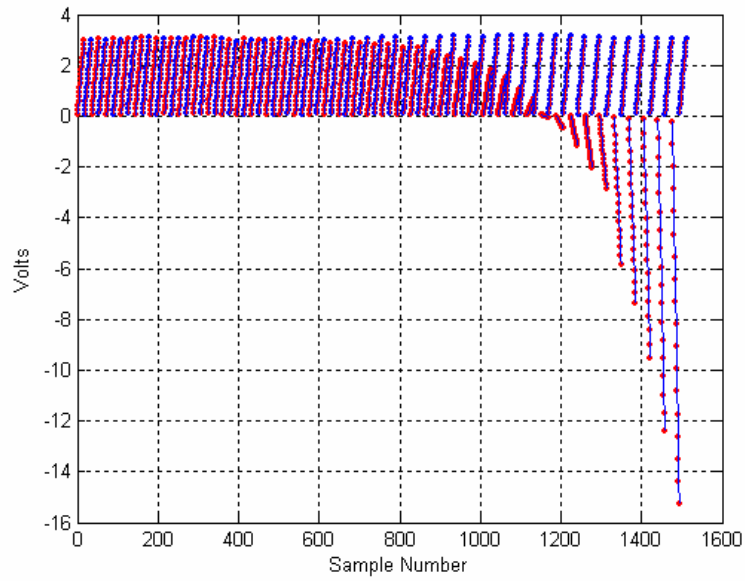


Figure 5.21: Output of the integrator in the DAC as a function of sample number. Red points: Data obtained with different resistor values connected to the conductive ring, blue points: Data obtained when no resistor is connected. Difference of these two gives the difference data.

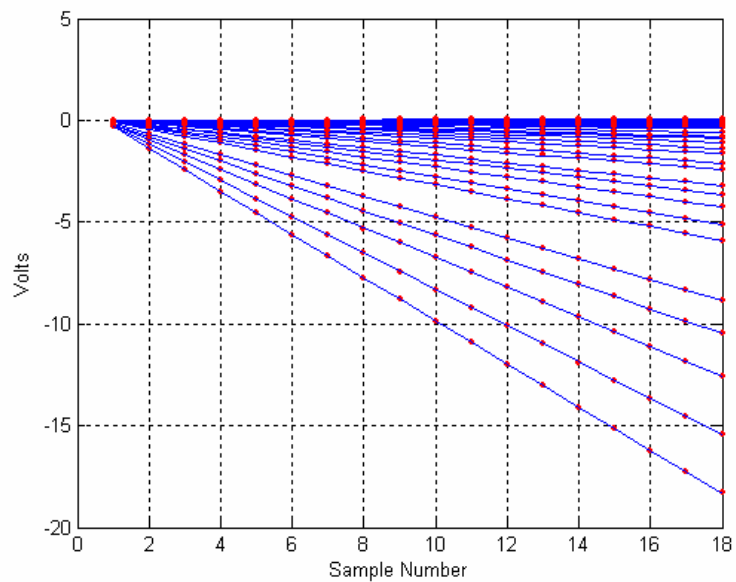


Figure 5.22: Output of the DAC using the integrator at the output stage as a function of the difference data sample number. Plots refer to different resistor values.

with resistor R, which makes the slope be inversely proportional with R.

In Figure 5.25, the Difference Data is plotted for the inversed values of resistors. Since integrator output is inversely proportional with resistor values, a linearly varying graph is obtained plotting the same data in Figure 5.23 for inversed resistor values. Data in the left hand side of the point indicated by the arrow in Figure 5.25 is zoomed and plotted in Figure 5.26 (a). The same process is applied in Figure 5.26 (b). In Figure 5.26 (c) the arrow shows the point related to the maximum distinguishable resistor value. That the points left to this one are not distinguishable comes from the limit of the SNR of the system.

Maximum measurable resistor value employing the integrator is limited by the Signal to Noise Ratio (SNR) of the system. In Figure 5.26 (c), the arrow indicates the minimum distinguishable value (which corresponds to maximum distinguishable resistor value) whose x value is $2.17 \cdot 10^{-3} \text{ 1}/\Omega$. Inverting this value, corresponding resistor value can be found to be $1 / (2.17 \cdot 10^{-3} \text{ 1}/\Omega) = 461 \text{ }\Omega$. For this resistor mean of the measured value is $2.5 \cdot 10^{-3} \text{ V}$ and corresponding value using the fitted line in Figure 5.26 (c) is $1.87 \cdot 10^{-4} \text{ V}$. For the points remaining in the left of this value which corresponds to large values of resistors, it can be deduced that SNR of the system is not sufficient to distinguish the larger resistor values. In Figure 5.26 (c), data which remain in the left of the dashed line refer to the large resistor values, for which induced voltages are below the noise level of the system.

5.4 Scanning Experiments

Scanning experiments are performed using both data acquisition systems: The LIAI and the DAAC. Human left palm is scanned with the system employing the LIAI. The DAAC was used to perform agar experiments.

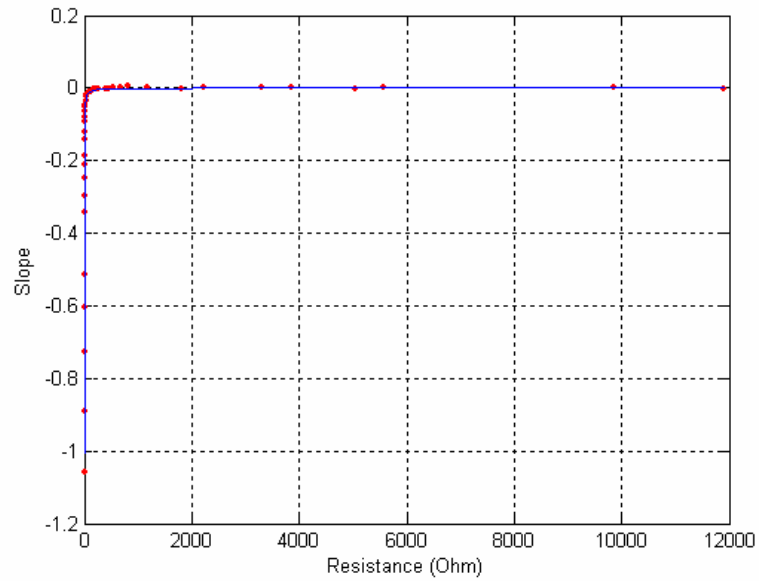


Figure 5.23: Slope of the lines fitting to the Difference Data as a function of resistor values. Red: Slope of the line fitted to the Difference Data, blue: curve fitted to the calculated slopes

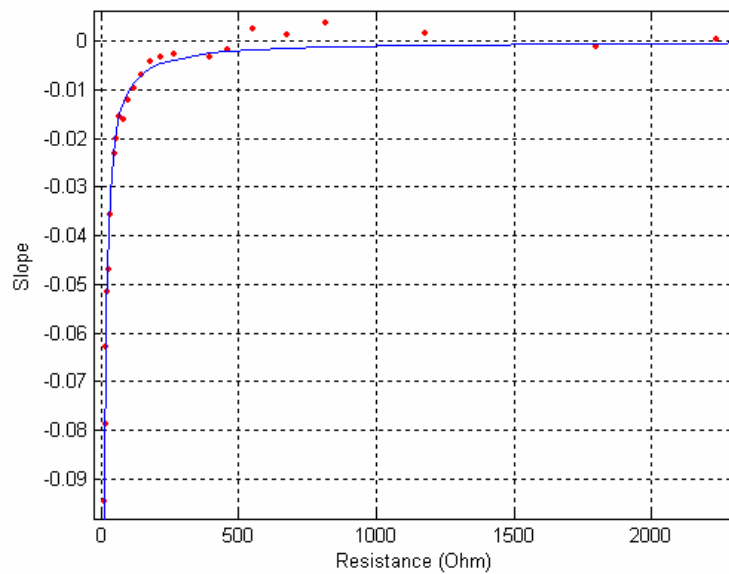


Figure 5.24: Zoomed version of the slope of the lines fitting to the Difference Data in Figure 5.23 as a function of resistor values. Red: Slope of the line fitted to the difference data, blue: fitted curve to the calculated slopes.

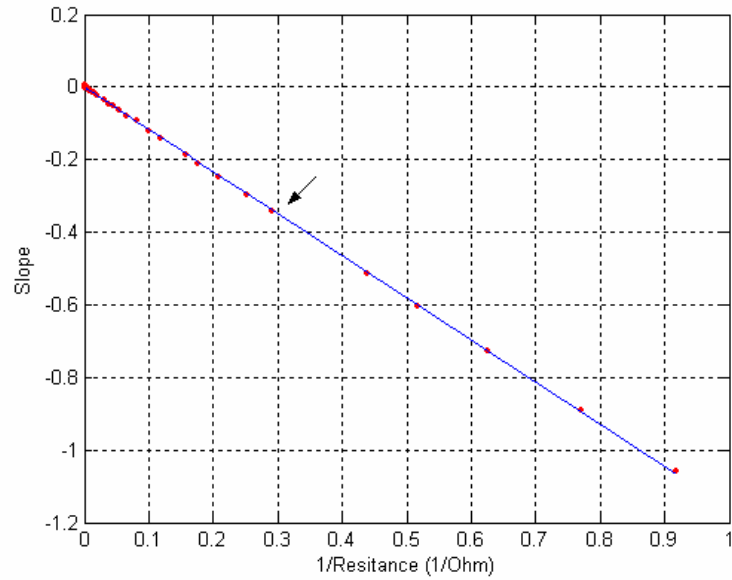
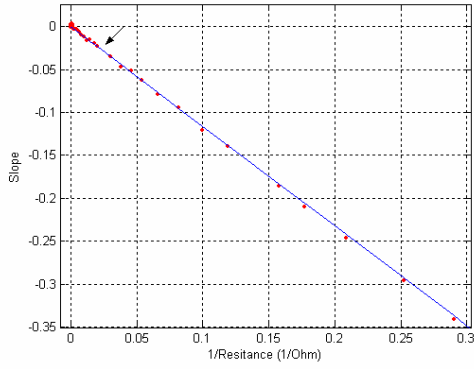
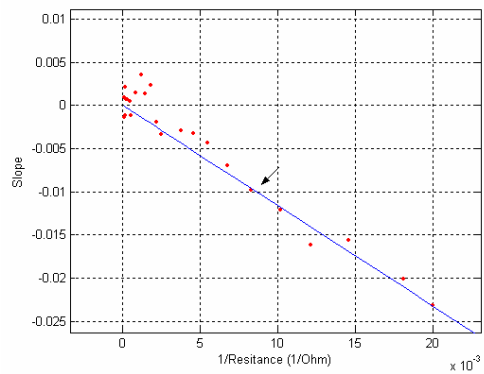


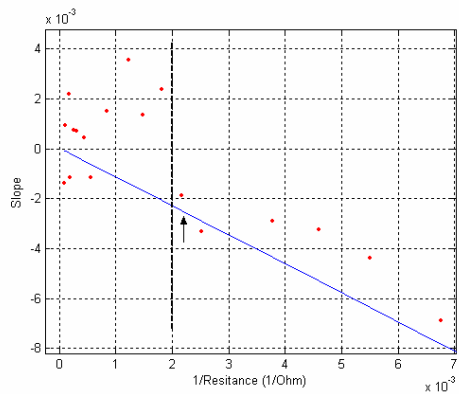
Figure 5.25: Slopes of the Difference Data lines as a function of inversed resistor values. Red points: Slope of the lines fitted to the Difference Data. Fitted line's (blue) expression is $y = -1.16x$.



(a)



(b)



(c)

Figure 5.26: Slopes of the Difference Data lines as a function of $1/\text{Resistor}$ values. Left hand side of the points indicated by arrows are zoomed in the following figures coming after (a) and (b). In (c) arrow indicates the point that the largest resistor value that can be distinguished.

5.4.1 Experiment using the LIAI

First experiment employs the LIAI together with the nulling circuit. The image profile for the palm of left hand of a human is obtained (Figure 5.27) after speeding up the scanning system using a microcontroller instead of D/A converters of the LIAI (Section 3.6). The scanning area is defined by 48*48 pixels. The pixel width is 3.6 mm which is equal to the distance traversed by the probe after each twelve steps of the step motor in the XY scanner. With the increased scanning speed, 17.2*17.2 cm² is scanned in 75 minutes. At each measurement point 10 samples are taken via RS232 port of the LIAI. The delay time between the arrival of the probe to the measurement point and the instant that the system starts to record measurements is set as 1 second. From this information, the average data acquisition time (scanning and recording the data) is calculated to be 0.15 sec/mm².

To provide an equal distance between the surface of the hand and the probe, the hand is pressed against a plastic plate placed between the palm of the hand and the probe. The thickness of the plate is 3mm. The hand is taped to the plate to stabilize the position and the volunteer kept his palm upward and pressed to the plate, which is located horizontally, through out the scanning.

The regions between the forefinger and the middle finger and also between the middle and ring finger are showed by the light blue color, which is also used to show the detected cavity in the middle of the palm. Since the wrist is bended to make 90° with the plate, it can not be observed in the profile.

Since some kind of soft plastic is used in the experiment, the region of the plate that the bone of the thumb is leaned against was curved. This causes the thumb to be located closer to the sensor and as a result the thumb is observed in red color. The increase in the received signal around thumb arises from the diminished distance to the probe. The same situation is observed about the region in the left side of the palm cavity. Lastly, the distortion at the little finger may be interpreted until some certain extent such that during the experiment little finger was scanned later than the rest of the hand. Thus due to the exhaustion and tiredness of the finger, its position may have changed.

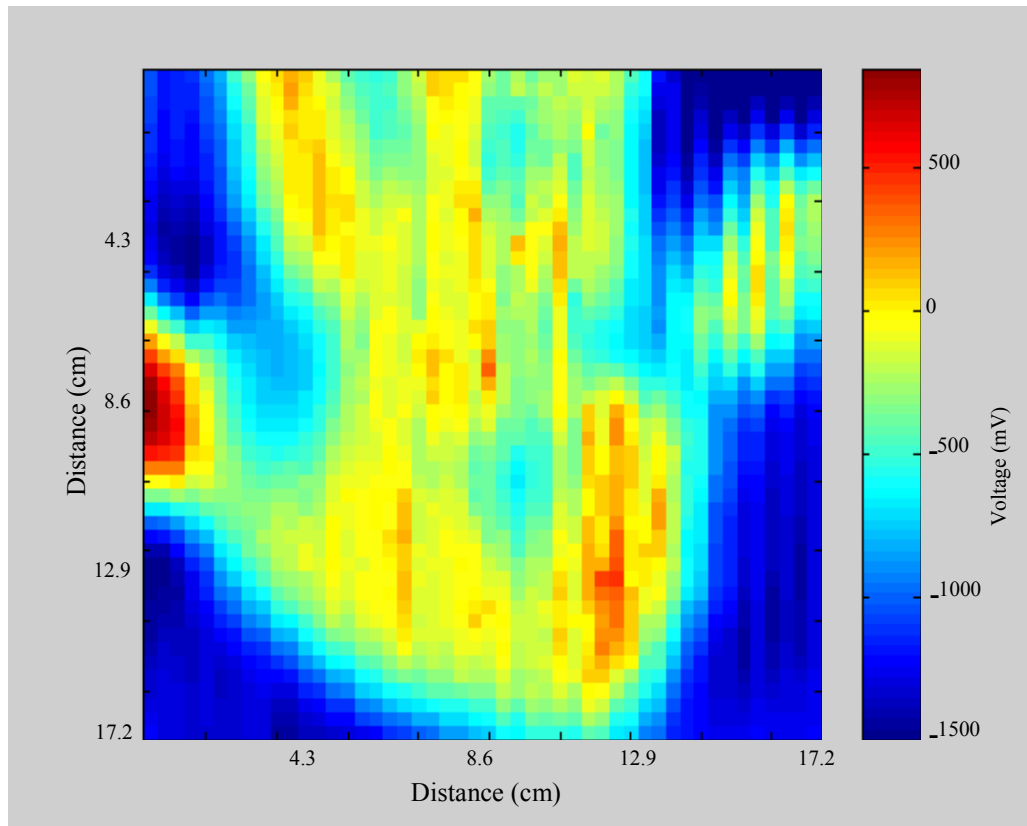


Figure 5.27: The field profile of the palm of the human left hand.

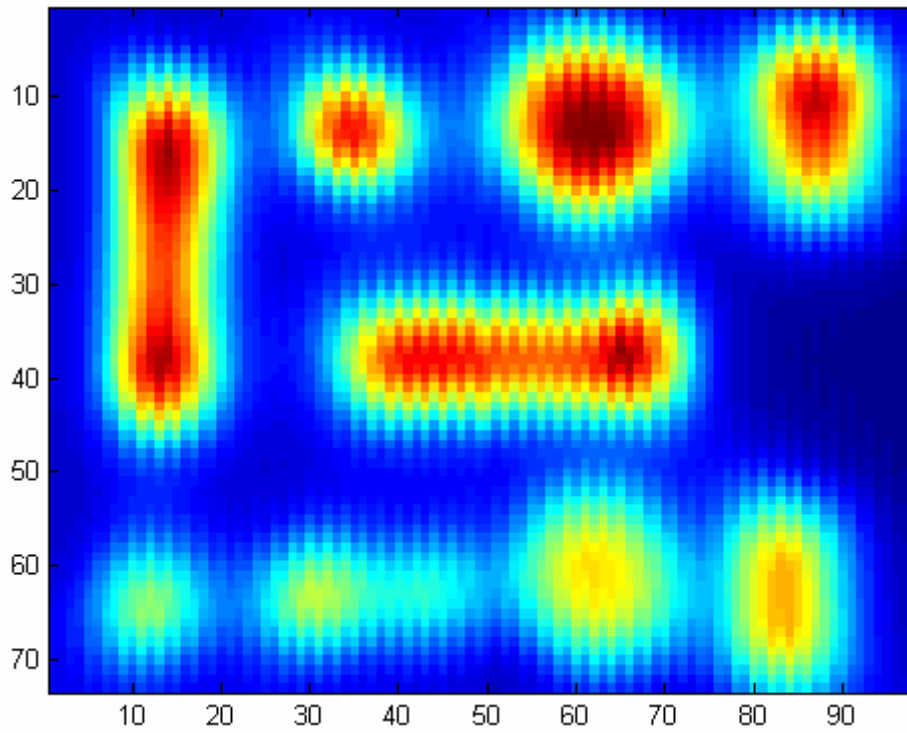
5.4.2 Experiment using the DAcC

The second experiment is performed using the DAcC. The agar objects with different geometries are placed in the saline solution and the image profile for this configuration is shown in Figure 5.28 (a). Actual locations, geometries, and relative dimensions of the agar objects can be observed in the photograph given in Figure 5.28 (b).

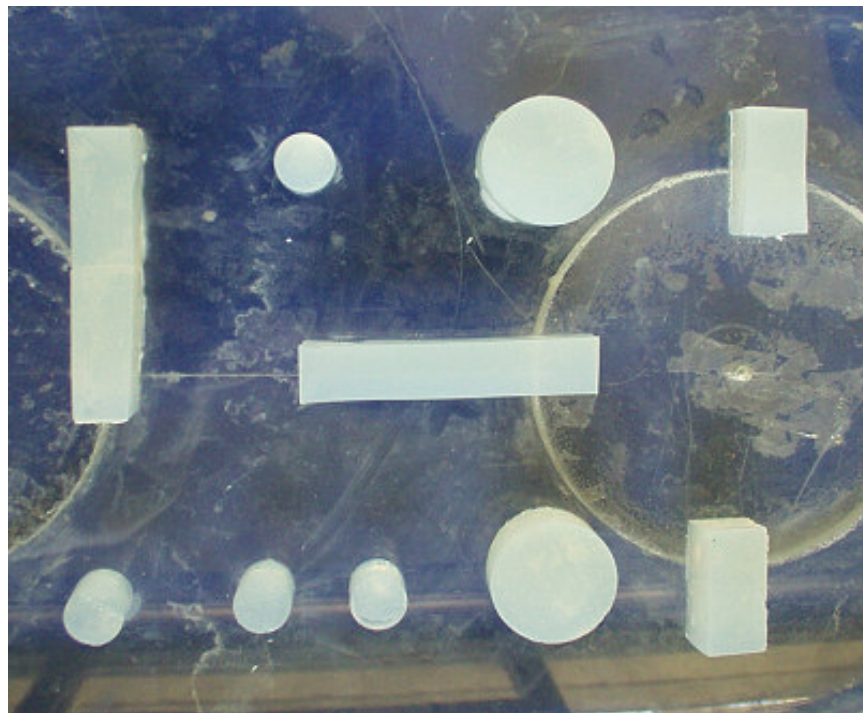
The scanning area is defined by 99*73 pixels. The pixel width is 2.4 mm which is equal to the distance traversed by the probe after each eight steps of the step motors in the XY scanner. 23.8*17.5 cm² is scanned in 149 minutes, taking 21 samples at each measurement point. Delay time is 200 ms. The step motors are driven at 200 Hz (single step takes 5 ms). Thus traversing 2.4 mm which is equal to

the eight steps of the step motor takes $8 \times 5 \text{ms} = 40 \text{ms}$.

The agar objects all have the conductivity value of 1 S/m whereas saline solution's conductivity is 0.2 S/m. All the agar objects have the height of 1 cm. Agar objects' upper surfaces are adjusted to be to be at the same level with the saline solution as much as possible. Even though, due to the slope of the surface that the scanner is based on, saline solution is not aligned exactly parallel with the agar objects' surfaces. There is a saline solution level difference around the agar objects imaged with red color and those that are imaged mostly with light green and yellow color. Although this difference is less than 1 mm, agar objects at the bottom of Figure 5.28 (a) are more distinguishable than those located above them. In the experiment, the DAAC is adjusted to produce maximum response in the existence of the agar objects.



(a)



(b)

Figure 5.28: (a): Image profile of the agar objects placed in saline solution of 0.2 S/m, (b): Agar objects of 1 S/m.

CHAPTER 6

CONCLUSION AND DISCUSSION

In a previous study, a prototype data acquisition system was developed for electrical impedance imaging via contactless measurements. That system uses magnetic excitation to induce currents inside the body and measures the magnetic fields of the induced currents using an axial gradiometer and a LIAI. In this study, first the scanning speed of that system was improved. Using a microcontroller to control the XY Scanner, the scan time is decreased from 4.67 sec/mm² to 0.15 sec/mm². User interface programs MATLAB Scanner 1.0 and Data Observer 1.0 were prepared to control the LIAI via PC and to analyze the acquired data, respectively. The image profile of a biological tissue (the human left hand) was obtained with use of the LIAI. A new data acquisition card, the DAcC was designed and constructed on PCB which eliminates the use of the LIAI in the phase sensitive measurements. Results of the system performance tests revealed that the DAcC operates as it was suggested: Individual tests for the blocks in the DAcC, as well as the overall system performance tests are made. Error in the phase sensitive measurements was measured to be 0.6% of the test signals. The minimum magnetic field density that could be detected was measured as 7 μ T. Induced magnetic density by tissue conductivity compatible objects was also calculated to be on the order of μ Tesla. An HP VEE program (HP VEE Scanner 1.0) was used to perform fast scanning experiments with the use of a microcontroller and the DAcC. Using the DAcC, field profiles of agar objects with different geometries were also obtained. A coil winding machine was prepared which enables the operator to design and wind up coils under self-controlled environment and conditions. With this device, it is possible wind coils with 20 rotations per second. Coil diameters can have

any value between 7 mm and 10 cm.

Main contributions of this study are as follows:

- 1) An inexpensive data acquisition system (the DAcC) was designed and realized. The system properties can be summarized as follows:
 - i) Maximum linearity error was measured as 2.37×10^{-3} % of the full scale for the amplifier and 6.60×10^{-4} % of the full scale for the integrator circuit. Thus output stage performance of the DAcC was improved by using an integrator instead of an amplifier in the output stage,
 - ii) Thermally generated voltage drift at the sensor output was measured to be 0.5 mV/minute in the ambient temperature,
 - iii) Overall normalized standard deviation at the output of the data acquisition system was observed as to be in the order of 10^{-4} ,
- 2) Novel experimental applications are developed:
 - i) Unique plastic phantoms were designed and were constructed to be used in conductivity tests pursued by using saline solutions. Phantoms have cylindrical chambers of 34 mm in diameter and 8 mm in height. These phantoms have openings that can be blocked by plastic screws. Thus evaporation and any concentration change in the saline solution were avoided. Upper surface of the phantoms have a thickness of 1.2 mm. Thus distance between the saline solution placed in the chamber of the phantom and the magnetic sensor was minimized,
 - ii) A test setup was configured using of an auxiliary coil to find out the reponse of the system to external magnetic fields. By calculating the resistance of a conductive disc, resistive ring experiments were related to the saline solution experiments pursued by cylindrical phantoms. In the resistive ring experiments (i.e., a conductive ring loaded with a variable resistor) maximum measurable resistor value was found as 397 Ω , using an amplifier at the output stage of the DAcC and

461 Ω using an integrator instead of the amplifier. Maximum measurable resistor value found in the resistive ring experiment was proportional to the minimum distinguishable conductance value of the cylindrical phantom experiment. Consequently, using 461 Ω shunted to the conductive ring corresponds to a saline solution of 2.7 S/m in the cylindrical phantom experiment, which was calculated setting $h = 0.01$ m in Equation 2.20,

- 3) Agar objects and biological tissues are scanned. The image profile of the biological tissue (the human left hand) was obtained, for the first time in the literature, as a result of the fast scanning experiments. Agar objects with conductivity value of 1 S/m in a saline solution of 0.2 S/m were scanned. Image profile of the scan fitted well with the actual locations, geometries, and relative dimensions of the agar objects.

As a future work, the system needs to be improved to distinguish the little changes around average body conductivity, (0.2 S/m) which corresponds to the disc resistance of ~ 6.3 k Ω . To obtain a better performance, sensitivity of the system should be increased, which can be achieved by increasing the SNR of the system. After that multi-frequency systems employing sensor arrays may be studied.

REFERENCES

- [1] Barber, D. C., Brown, B. H., “*Applied potential tomography*”, J. Phys. E: Sci. Instrum., vol. 17, pp. 723-733, 1984.
- [2] Seagar, A. D., Barber, D. C., and Brown, B. H., “*Electrical impedance imaging*”, IEE Proc. A, vol. 134, pp. 201–10, 1987
- [3] Morucci, J., Rigaud, B., “*Bioelectrical impedance techniques in medicine*”, Crit. Rev. Biomed. Eng., vol. 24, pp. 467-597, 1996.
- [4] Isaacson, D., “*Distinguishability of conductivities by electric current computed tomography*”, IEEE Trans. Med. Imag., vol. 5, pp. 91-95, June 1986.
- [5] Bronzino, J., *The Biomedical Engineering Handbook*, IEEE press, CRC Press, 1995.
- [6] Purvis, W. R., Toker, R. C., Anderson, D. K., and Freeston, I, “*Induced current impedance imaging*”, IEEE Proceedings - A, vol. 140, pp. 135-141, March 1993.
- [7] Gencer, N. G., M. Kuzuoglu, and Ider, Y. Z., “*Electrical impedance tomography using induced currents*”, IEEE Trans. Med. Imag., vol. 13, pp. 338-350, June 1994.
- [8] Gencer, N. G., Ider, Y. Z., and Williamson, S. J. , “*Electrical impedance tomography: Induced current imaging achieved with a multiple coil system*”, IEEE Trans. on Med. Imag., vol. 43, pp. 139-149, February 1996.
- [9] Gencer, N. G., “*Electrical Impedance Tomography Using Induced Currents*”, Ph.D. Thesis, Middle East Technical University, Ankara, Turkey, July 1993.
- [10] Freeston, I., Tozer, R. “*Impedance imaging using induced currents*”, Physiol. Meas., vol. 16, no. supp 3.A, pp. 257-266, 1995.
- [11] Sharon Zlochiver, Michal Radai, M., Shimon Abboud, Moshe Rosenfeld, Xiu-Zhen Dong, Rui-Gang Liu, Fu-Sheng You, Hai-Yan Xiang and Xue-Tao Shi, “*Induced current electrical impedance tomography system: experimental results and numerical simulations*”, Physiol. Meas., vol. 25, pp. 239–255, 2004.
- [12] McArdle, F., “*Investigation of cardiosynchronous images of the hearth and head using applied potential tomography*”, Ph.D. Thesis, Sheffield, University of Sheffield, 1992.

- [13] McArdle, F, Brown, B., Pearse, R., and Barber, D., “*The effect of skull of low birthweight neonates on applied potential tomography imaging of centralised resistivity changes*”, Clin. Phys. Physiol. Meas., vol. 9, no. suppl. A, pp. 55-60, 1988.
- [14] Eyuboglu, B. M., Oner, F. A. A., Baysal, U., Bibert, C., Keyf, A.İ., Yilmaz Ü., and Erdoğan, Y., “*Application of electrical impedance tomography in diagnosis of emphysema - a clinical study*”, Physiol. Meas., vol. 16, pp. A191-A211, 1995.
- [15] Eyuboglu, B. M., Brown, B. H., Barber, D. C., and Seager, A., “*Localization of cardiac related impedance changes in the thorax*”, Clin. Phys. Physiol. Meas., vol. 8, pp. A167-A173, 1987.
- [16] Eyuboglu, B. M., Brown, B. H., and Barber, D. C., “*Problems of cardiac output determination from electrical impedance tomography scans*”, Clin. Phys. Physiol. Meas., vol. 9, pp. 71-77, 1988.
- [17] Eyuboglu, B. M., Brown, B. H., “*Methods of cardiac gating applied potential tomography*”, Clin. Phys. Physiol. Meas., vol. 9, pp. 43-48, 1988.
- [18] Harris, N., Suggett, A., Barber, D., and Brown, B., “*Applications of applied potential tomography (APT) in respiratory machine*”, Clin. Phys. Physiol. Meas., vol. 8A, pp. 155-165, 1987.
- [10] Freeston, I., Tozer, R. “*Impedance imaging using induced currents*”, Physiol. Meas., vol. 16, no. supp 3.A, pp. 257-266, 1995.
- [11] Sharon Zlochiver, Michal Radai, M., Shimon Abboud, Moshe Rosenfeld, Xiu-Zhen Dong, Rui-Gang Liu, Fu-Sheng You, Hai-Yan Xiang and Xue-Tao Shi, “*Induced current electrical impedance tomography system: experimental results and numerical simulations*”, Physiol. Meas., vol. 25, pp. 239–255, 2004.
- [12] McArdle, F., “*Investigation of cardiosynchronous images of the hearth and head using applied potential tomography*”, Ph.D. Thesis, Sheffield, University of Sheffield, 1992.
- [13] McArdle, F, Brown, B., Pearse, R., and Barber, D., “*The effect of skull of low birthweight neonates on applied potential tomography imaging of centralised resistivity changes*”, Clin. Phys. Physiol. Meas., vol. 9, no. suppl. A, pp. 55-60, 1988.
- [14] Eyuboglu, B. M., Oner, F. A. A., Baysal, U., Bibert, C., Keyf, A.İ., Yilmaz Ü., and Erdoğan, Y., “*Application of electrical impedance tomography in diagnosis of emphysema - a clinical study*”, Physiol. Meas., vol. 16, pp. A191-A211, 1995.

- [15] Eyuboglu, B. M., Brown, B. H., Barber, D. C., and Seager, A., “*Localization of cardiac related impedance changes in the thorax*”, Clin. Phys. Physiol. Meas., vol. 8, pp. A167-A173, 1987.
- [16] Eyuboglu, B. M., Brown, B. H., and Barber, D. C., “*Problems of cardiac output determination from electrical impedance tomography scans*”, Clin. Phys. Physiol. Meas., vol. 9, pp. 71-77, 1988.
- [17] Eyuboglu, B. M., Brown, B. H., “*Methods of cardiac gating applied potential tomography*”, Clin. Phys. Physiol. Meas., vol. 9, pp. 43-48, 1988.
- [18] Harris, N., Suggett, A., Barber, D., and Brown, B., “*Applications of applied potential tomography (APT) in respiratory machine*”, Clin. Phys. Physiol. Meas., vol. 8A, pp. 155-165, 1987.
- [19] Harris, N., Suggett, A., Barber, D., and Brown, B., “*Applied potential tomography: A new technique for monitoring pulmonary function*”, Clin. Phys. Physiol. Meas., vol. 9A, pp. 79-85, 1988.
- [20] Mcleod, C., Shi, Y., Denyer, C., Lidgey, F., Lionheart, W., Mcleod, C., Paulson, K., and Pidcock, M., “*Chest impedance imaging using trig. current patterns*”, in Proc. IX Int. Conf. on Electrical Bio-impedance, Heidelberg, Germany, (Heidelberg: University of Heidelberg), pp. 408-409, 1995.
- [21] Avill, R., Mangnall, Y. F., Bird, N. C., Brown, B. H., Barber, D. C., Seager, A., Johnson, A. G., and Read, N. W., “*Applied potential tomography: A new non-invasive technique for measuring gastric emptying*”, Gastroenterology, vol. 92, pp. 1019-1026, 1987.
- [22] Mangnall, Y. F., Baxter, A. J., Avill, R., Bird, N. C., Brown, B. H., Barber, D. C., Seager, A., Johnson, A. G., and Read, N. W., “*Applied potential tomography: A new non-invasive technique for assesing gastric function*”, Clin. Phys. Physiol. Meas., vol. 8, pp. 119-129, 1987.
- [23] Piperno, G., Frei, E., and Moshitzky, M., “*Breast cancer screening by impedance measurements*”, Frontiers Med. Biol. Eng., vol. 2, no. 2, pp. 111-117, 1990.
- [24] Cherepenin, V., Karpov, A., Korjenevsky, A., Kornienko, V., Mazaletskaya, A., Mazurov, D., and Meister, D. “*A 3D electrical impedance tomography (EIT) system for breast cancer detection*”, Phys. Meas., vol. 22, pp. 9-18, 2001.
- [25] Kerner, T. E., Paulsen, K. D., Hartov, A., Soho, S. K., and Poplack, S. P., “*Electrical impedance spectroscopy of the breast: clinical results in 26 subjects*”, IEEE Trans. Med. Imaging, vol. 21, pp. 638-45, 2002.

- [26] Nirmal K. Soni, Alex Hartov, Christine Kogel, Steven P. Poplack and Keith D. Paulsen, “*Multi-frequency electrical impedance tomography of the breast: new clinical results*”, *Physiol. Meas.*, vol. 25, pp. 301–314, 2004.
- [27] Mueller, J. L., Isaacson, D., Newell, J. C., “*Reconstruction of conductivity changes due to ventilation and perfusion from eit data collected on a rectangular electrode array*”, *Phys. Meas.*, vol. 22, pp. 97-106, 2001.
- [28] Robert Merwa, Karl Hollaus, Oszkar Biro and Hermann Scharfetter, “*Detection of brain oedema using magnetic induction tomography: a feasibility study of the likely sensitivity and detectability*”, *Physiol., Meas.*, vol. 25, pp. 347–354, 2004.
- [29] Liston, A. D., Bayford, R. H., Tidswell A. T., and Holder, D. S., “*A multi-shell algorithm to reconstruct EIT images of brain function*”, *Physiol. Meas.*, vol. 23, pp. 105–119, 2002.
- [30] Bagshaw, A. P., Liston, A. D., Bayford, R. H., Tizzard, A., Gibson, A. P., Tidswell, A. T., Sparkes, M. K., Dehghani, H., Binnie, C. D., and Holder, D. S., “*Electrical impedance tomography of human brain function using reconstruction algorithms based on the finite element method*”, *Neuroimage*, vol. 20, pp. 752–63, 2003.
- [31] Ireland, R. H., Tozer, J. C., Barker, A. T., Barber, D. C., “*Towards magnetic detection electrical impedance tomography: data acquisition and image reconstruction of current density in phantoms and in vivo*”, *Physiol. Meas.*, vol. 25, pp. 775–796, 2004.
- [32] Cherepenin, V., Karpov, A., Korjenevsky, A., Kornienko, V., Kultiasov Y., Mazaletskaya A., and Mazourov D., “*Preliminary static EIT images of the thorax in health and disease*”, *Physiol. Meas.*, vol. 23, pp. 33–41, 2002.
- [33] David Holder, “*Editorial, Biomedical Applications of Electrical Impedance Tomography*”, *Physiol. Meas.*, vol. 23, issue 2, 2002.
- [34] Alexander Hartov, Nirmal K. Soni and Keith D. Paulsen, “*Variation in breast EIT measurements due to menstrual cycle*”, *Physiol. Meas.*, vol. 25, pp. 295–299, 2004.
- [35] Liston, A. D., Bayford R. H., and Holder D. S., “*The effect of layers in imaging brain function using electrical impedance tomography*”, *Physiol. Meas.*, vol. 25, pp. 143–158, 2004.
- [36] Netz, J., Forner, E., and Haagemann S., “*Contactless impedance measurement by magnetic induction- a possible method for investigation of brain impedance*”, *Physiol. Meas.*, vol. 14, pp. 463-471, 1993.

- [37] Purvis, W. R. , Tozer, R. C., and Freeston, I. L., “*Impedance imaging using induced currents*”, in Proc. 12th Ann. Int. Conf. IEEE Eng. Med. Biol. Soc., vol. 12, pp. 114-115, 1990.
- [38] Scaife, J. M., Tozer, R. C., and Freeston, I. L., “*Real and imaginary impedance images using induced currents*”, in Proc. 12th Ann. Int. Conf. IEEE Eng. Med. Biol. Soc., vol. 12, pp. 116-117, 1990.
- [39] Mengxing Tang, Wei Wang, James Wheeler, Malcolm McCormick and Xiuzhen Dong, “*The number of electrodes and basis functions in EIT image reconstruction*”, *Physiol. Meas.* vol. 23, pp.129–140, 2002.
- [40] Ider, Y. Z., Nakiboglu, B., Kuzuoglu, M., and Gençer, N. G., “*Electrical impedance tomography. determination of the boundary of an object inserted into a water-filled cylinder*”, *Clin. Phys. Physiol. Meas.*, vol. 13, Supp. A, pp. 151-154, 1992.
- [41] Andy Adler, “*Accounting for erroneous electrode data in electrical impedance tomography*”, *Physiol. Meas.*, vol. 25, pp. 227–238, 2004.
- [42] Williams, R. A., Beck M. S., “*Process Tomography: Principles, Techniques and Applications*”, Oxford: Butterworth Heinemann, 1995.
- [43] Daily, W., Ramirez A., “*Environmental process tomography in the United States*”, *Chem. Eng. J. Biochem. Eng.*, vol. 56 (3), pp. 159–65, 1995.
- [44] Noel, M., Xu B., “*Archaeological investigation by electrical resistance tomography: a preliminary study*”, *Geophys. J. Int.*, vol. 107, pp. 95–102, 1991.
- [45] Tarjan, P., McFee, R., “*Electrodeless measurements of the active resistivity of the human torso and head by magnetic induction*”, *IEEE Transactions on Biomedical Engineering*, vol. 15, pp. 266-278, October 1968.
- [46] Al-Zeibak, S., Sunders, N. H., “*A feasibility study of in vivo electromagnetic imaging*”, *Phys. Med. Biol.*, vol. 38, pp. E1-160, 1993.
- [47] Gençer, N. G., Tek, M. N., “*Imaging tissue conductivity via contactless measurements: a feasibility study*”, *TUBITAK Elektrik J.*, vol. 6, no. 3, pp. 183-200, 1998.
- [48] Gençer, N. G. , Tek, M. N., “*Forward problem solution for electrical conductivity imaging via contactless imaging*”, *Phys. Med. Biol.*, vol. 44, pp. 927-940, April 1999.
- [49] Tek, M. N., “*Electrical conductivity imaging via contactless measurements: Forward and Inverse Problem Simulations*”, MSc. Thesis. Middle East Technical University, July 1998.

- [50] Gençer, N. G., Tek, M. N., “*Electrical conductivity imaging via contactless measurements*”, IEEE Trans. on Med. Imag., vol. 18, pp. 617-627, July 1999.
- [51] Başak Ülker Karbeyaz, Nevzat G. Gençer, “*Electrical Conductivity Imaging via Contactless Measurements: An Experimental study*”, IEEE Transactions on Medical Imaging, vol. 22, no. 5, pp. 627-635, May 2003.
- [52] Başak Ülker, Nevzat G. Gençer, “*Implementation of a Data Acquisition System for Contactless Conductivity Imaging*”, IEEE Eng. Med. Biol., pp.152-155, September/October 2002.
- [53] Başak Ülker, “*Implementation of a Data Acquisition System for Contactless Conductivity Imaging*”, MSc. Thesis, Middle East Technical University, December 2001.
- [54] Ahmad, T., Gençer, N. G., “*Development of Data Acquisition System for Conductivity Images of Biological Tissues via Contactless Measurements*”, Proceedings of 23rd Annual EMBS International Conference, October 25-28, Istanbul, Turkey, 2001.
- [55] Ahmad, T., “*Experimental Studies on Development of a New Imaging System for Contactless subsurface Conductivity Imaging of Biological Tissues*”, MSc. Thesis, Middle East Technical University, August 2001.
- [56] Riedel, C. H., Keppelen, M., Nani, S., Merges, R. D. and Dossel, O., “*Planar system for magnetic induction conductivity measurement using a sensor matrix*”, Physiol. Meas. vol. 25, pp. 403–411, 2004.
- [57] Korzhenevskii, A. V., Cherepenin, V. A., “*Magnetic induction tomography*”, J. Commun. Tech. Electron., vol. 42, pp. 469–74, 1997.
- [58] Korjenevsky, A., Cherepenin, V., and Sapetsky, S., “*Magnetic induction tomography: experimental realization*”, Physiol. Meas., vol. 21, pp. 89–94, 2000.
- [59] Korjenevsky, A., Sapetsky, S., “*Methods of measurements and image reconstruction in magnetic induction tomography*”, Proc. 2nd EPSRC Engineering Network Meeting on Biomedical Applications of EIT, 5–7 April, London, 2000.
- [60] Griffiths H., “*Magnetic induction tomography*”, Meas. Sci. Technol., vol. 12, pp. 1126–1131, 2001.
- [61] Watson, S., Williams, R. J., Griffiths, H., Gough, W., and Morris, A., “*Frequency down-conversion and phase noise in MIT*”, Physiol. Meas. 23, 189–194, 2002.
- [62] Gough, W., “*Circuit for the measurement of small phase delays in MIT*”, Physiol. Meas., vol. 24, pp. 501–507, 2003.

- [63] Watson, S, Williams, R. J., Griffiths, H., Gough W. and Morris, A., “*Magnetic induction tomography: phase versus vector-voltmeter measurement techniques*”, *Physiol. Meas.*, vol 24, pp. 555–564, 2003.
- [64] Watson, S., Morris, A., Williams, R. J., Griffiths H., and Gough, W., “*A primary field compensation scheme for planar array magnetic induction tomography*”, *Physiol. Meas.*, vol. 25, pp. 271–279, 2004.
- [65] Igney, C. H., Watson, S., Williams, R. J., Griffiths H., and Dossel, O., “*Design and performance of a planar-array MIT system with normal sensor alignment*”, *Physiol. Meas.*, vol 26, pp. S263–S278, 2005.
- [66] Watson, S., Igney, C. H., Dossel, O., Williams R. J., and Griffiths, H., “*A comparison of sensors for minimizing the primary signal in planar-array magnetic induction tomography*”, *Physiol. Meas.*, vol 26, pp. 319–331, 2005.
- [67] Hermann Scharfetter, Stephan Rauchenzauner, Robert Merwa, O Biro, and Karl Hollaus, “*Planar gradiometer for magnetic induction tomography (MIT): theoretical and experimental sensitivity maps for a low-contrast phantom*”, *Physiol. Meas.*, vol 25, pp. 325–333, 2004.
- [68] Hermann Scharfetter, Robert Merwa, and Karl Pilz, “*A new type of gradiometer for the receiving circuit of magnetic induction tomography (MIT)*”, *Physiol. Meas.*, vol. 26, pp. 307–318, 2005.
- [69] Lennart Bavall, “*Determination of the thickness of copper coatings on steel by measuring the impedance of a thin elliptic coil*”, *Meas. Sci. Technol.*, vol. 13, pp. 510–519, 2002.
- [70] Jackson, J., *Classical Electrodynamics*, John Wiley and Sons Inc., ISBN: 0-471-30932-X, 1998.
- [71] Williamson, S., Romani, G., Kaufman, L., and Modena, I. eds., “*Physical concepts and mathematical models in Biomagnetism: an Interdisciplinary Approach*”, pp. 101-139, New York: Plenum Press, 1983.
- [72] Cheng, D. K., *Field and Wave Electrodynamics*, Addison-Wesley Publishing Company, ISBN: 0-201-01239-1, 1983.
- [73] UAF42, Universal Active Filter Datasheet, Burr-Brown.
- [74] Model 5209 Lock-In Amplifier Instruction Manual. EG&G Instruments Corporation, 1992.

[75] Axelson, J., “*Her yönüyle Seri Port*”, Çeviren: C.Gerçek, Editör: G.Dinçer, Katkıda Bulunanlar: Z.Aytemur, A.Bodur, Mart 2000, ISBN: 975-6897-07-4, www.Tekno-market.com yayınları.

[76] PIC16F877 Microcontroller Datasheet, Microchip.

[77] LM12 80W operational amplifier datasheet, National semiconductors, 1999.

[78] Tarjan, P., “*Electrodeless measurements of Resistivity Fluctuations in the human torso and head*”, Ph. D. Thesis., vol. 15, pp. 266-278, October 1968.